Moritz Johannes Püschel

Electromagnetic Effects in Gyrokinetic Simulations of Plasma Turbulence

2009

Theoretische Plasmaphysik

Electromagnetic Effects in Gyrokinetic Simulations of Plasma Turbulence

Inaugural-Dissertation

zur Erlangung des Doktorgrades
der Naturwissenschaften im Fachbereich Physik
der Mathematisch-Naturwissenschaftlichen Fakultät
der Westfälischen Wilhelms-Universität Münster

vorgelegt von

Moritz Johannes Püschel

aus Starnberg

2009

Dekan:	Prof. Dr. Johannes Wessels
Erster Gutachter:	Prof. Dr. Frank Jenko
Zweiter Gutachter:	Prof. Dr. Rudolf Friedrich
Tag der mündlichen Prüfung:	12. 3. 2009
Tag der Promotion:	12. 3. 2009

Abstract

This thesis details findings related to the effects of magnetic field fluctuations on the properties of microturbulent transport in fusion plasmas. To this end, direct numerical analyses and supporting analytical investigations are performed.
Primarily, the gyrokinetic turbulence code GENE is employed to obtain the results presented here – the derivation of its basic equations is outlined, along with its most important numerical features. Examples for contributions to its development are given in a detailed study of the effects of multiple (hyper-)diffusion terms on GENE simulations, as well as in an overview of data visualization tools. The rest of the thesis is focussed on physical scenarios.
Advances are presented in electromagnetic simulations with so-called Cyclone Base Case parameters: Linearly, the subdominant and stable behavior of Kinetic Ballooning Modes (KBMs) is studied, along with mode interactions and transformations. The nonlinearly accessible range of the plasma pressure is extended significantly, showing for the first time examples of KBM turbulence. Multiple analyses concerning the transport levels at high pressure are performed, including quasilinear models and zonal flow studies. To augment these results, a second operation point is chosen in the Trapped Electron Mode regime which displays different physical behavior in multiple aspects.
The aforementioned simulations are analyzed to solidify a test particle based model for the magnetic transport, to study the nature of changes to the magnetic geometry due to fluctuations of the magnetic field, and to investigate the behavior of fast ions as they are subjected to electromagnetic fields. Additionally, effects of realistic geometry on simulations at finite plasma pressure are discussed.
Finally, two astrophysical scenarios are analyzed in the context of microturbulent heat transport levels. In the case of evaporating cold gas clouds immersed in much hotter material, such transport may have a significant impact on the standard model for these objects.

Zusammenfassung

In der vorliegenden Arbeit werden Untersuchungen zu den Auswirkungen von Magnetfeldfluktuationen auf die Eigenschaften turbulenten Transports in Fusionsplasmen dargelegt. Hierzu werden direkte numerische Analysen wie auch analytische Modellrechnungen eingesetzt.
Primär wird der gyrokinetische Turbulenzcode GENE für die Berechnung der hier dargestellten Ergebnisse verwendet – die Herleitung seiner Grundgleichungen wie auch die wichtigsten seiner numerischen Fähigkeiten werden beschrieben. Beispiele von Beiträgen zu seiner Entwicklung beinhalten eine ausführliche Studie der Effekte verschiedener (Hyper-)Diffusionsterme auf GENE-Simulationen, aber auch einen Überblick über Programme zur Datenvisualisierung. Der übrige Teil dieser Arbeit behandelt physikalische Szenarien.
Fortschritte bei elektromagnetischen Simulationen mit sogenannten Cyclone-Base-Case-Parametern sind aufgeführt: Im Falle linearer Rechnungen werden das subdominante und stabile Verhalten von Kinetischen Ballooning-Moden (KBM) untersucht; auch Wechselwirkung und Transformation von Moden wird behandelt. Nichtlinear wird der zugängliche Wertebereich des Plasmadrucks stark erweitert, und erstmalig werden Fälle von KBM-Turbulenz präsentiert. Verschiedene Transportanalysen werden eingesetzt, unter anderem quasilineare Modelle und Untersuchungen von sogenannten Zonal Flows. Zur Erweiterung dieser Studie wird ein zweiter Parametersatz hinzugezogen, bei welchem Turbulenz von Gefangenen-Elektronen-Moden zu einem qualitativ abweichenden physikalischen Verhalten führt.
Die oben erwähnten Simulationen werden zusätzlichen Analysen unterworfen zu Untersuchungen eines Modells für den magnetischen Transport, des Einflusses von Magnetfeldfluktuationen auf die Magnetfeldstruktur sowie des Verhaltens schneller Ionen in elektromagnetischen Feldern. Zusätzlich werden Effekte realistischer Geometrien auf Simulationen mit endlichem Plasmadruck besprochen.
Zuletzt werden zwei astrophysikalische Szenarien untersucht; hierbei steht der Einfluß mikroturbulenten Transports im Vordergrund. Im Fall verdampfender kalter Gaswolken in einem deutlich heißeren Medium besteht die Möglichkeit, daß anomaler Transport einen signifikanten Einfluß auf das Standardmodell für solche Objekte hat.

Contents

Chapter 1

Introduction – Nuclear Fusion

> *By the time our young children reach middle age, fusion may begin to deliver energy independence and energy abundance to all nations rich and poor. Fusion is a promise for the future we must not ignore.*
>
> Spencer Abraham

> *Even if it succeeds, [ITER] will be just a proof of concept, with commercial fusion power still decades away. But if we don't reach for such lofty goals, we may eventually find ourselves moving past denial into the next stage: depression.*
>
> Corey S. Powell

Imitating nature has provided mankind with some great advancements even in the most complex technological fields – looking to the gecko for surface adhesion, constructing a robotic water strider, or analyzing lotus leaves in order to understand their self-cleaning property. One of the most critical resources, energy, is provided to this planet by the Sun via nuclear fusion. However, humanity is still dependent on energy sources that are becoming increasingly scarce. At the same time, the corresponding production processes are highly problematic, be it due to the carbon emissions caused by burning fossil fuels or the fact that permanent nuclear waste storage is still an unsolved problem. Creating a small star on Earth would be but another step in following nature's teachings.

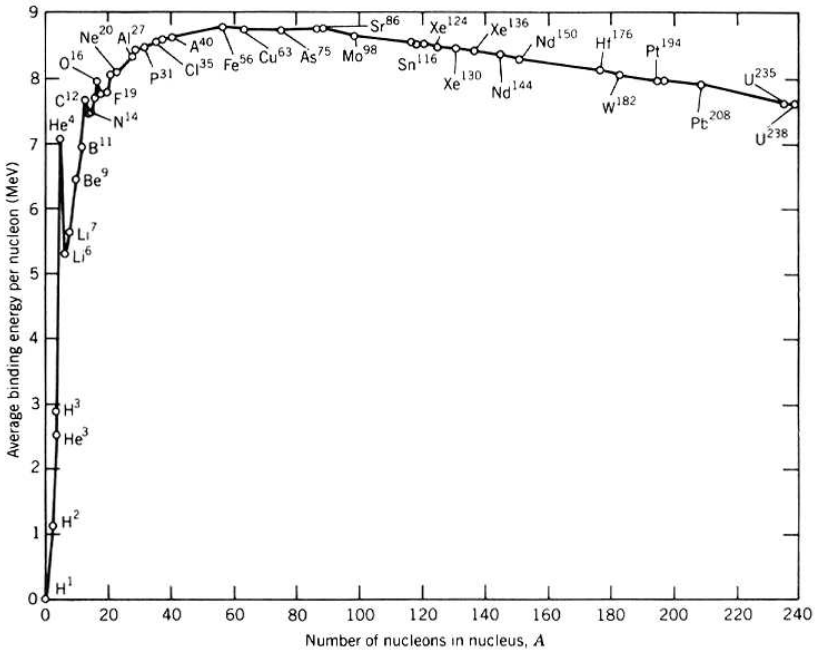

Figure 1.1: Chart of the binding energies of selected atomic nuclei. The elements to the left of iron – the stablest nucleus – can be combined in fusion processes, while the elements to the right may be split; in both cases energy is released. The maximal energy gain is achieved by fusing the lightest of elements, utilizing the large slope of this graph at the lowest mass numbers. Source: [1]

In fusion processes, light nuclei are combined into heavier ones, releasing energy corresponding to the mass difference of the output and input nuclei; much in analogy to nuclear fission, where very heavy elements are split into lighter ones. A significant difference, however, lies in the potential energy gain per elementary process which for fusion exceeds the fission gain by an order of magnitude (see Fig. 1.1).

During the fusion process, two (positively charged) nuclei approach one another closely enough for the strong nuclear force to overcome the electrostatic repulsion and thus combine them into a single nucleus. For typical reactions, the energy yield is ~ 10 MeV – roughly six orders of magnitude larger than the ionization energy of hydrogen which can be used as an upper boundary estimate for chemical reaction energies. Therefore, relying on fusion reactions for power generation would require substantially less fueling material compared to chemical reactions, e.g.: burning of coal.

Overcoming the Coulomb barrier requires large particle energies. If one was to consider only classical particles, the resulting necessary temperature would be enormous – the Sun could not be powered by fusion processes. However, as a consequence of the uncertainty principle for position and momentum, the wave functions of the nuclei may overlap before they have penetrated their respective Coulomb barriers, making a fusion reaction possible via tunneling at much lower energy than the classical prediction.

1.1 Fusion Reactions

The universe owes the existence of heavier elements to supernova explosions where for a very short time, thermodynamic conditions allow for the creation of a wide range of nuclei. However, in most other cases – be it the nucleosynthesis in the early universe, a main branch star, or a fusion reactor – very light elements are fusing to form only slightly heavier ones.

1.1.1 Astrophysical Fusion Processes

Within the first half hour after the Big Bang, roughly one quarter of the baryonic mass was converted to helium by fusing protons and neutrons (free neutrons were highly abundant at that point); however, due to the rapid expansion of the universe, temperature and pressure soon dropped below the required levels and thus halted nuclear fusion reactions. Only later, after the formation of the first stars, did fusion-relevant conditions occur again.

Proton-Proton Chain

Most stars, the Sun with a central temperature of abount 10^7K being one of them, mainly rely on the proton-proton chain to produce energy. In this sequence of reactions, four protons are converted to an alpha particle,

$$4\,{}^1_1\mathrm{H} + 2\mathrm{e}^- \longrightarrow {}^4_2\mathrm{He} + 2\nu_\mathrm{e} + 26.7\,\mathrm{MeV} \quad .$$

There are multiple different ways in which the last step – the creation of the helium nucleus – may be realized. This has an impact on the reaction rate and the energies of the neutrinos produced in the reactions, but not on the reaction equation.

CNO Cycle

Heavier stars can use carbon as a catalyst to burn hydrogen with higher efficiency. In the standard version of the so-called CNO (carbon-nitrogen-oxygen) cycle, a carbon nucleus fuses with a proton to produce nitrogen, β^+-decays back into carbon, picks up two more protons to form oxygen, followed by another β^+ decay. During the last step, the oxygen fuses with another proton into a metastable nucleus that decays into carbon and helium, again creating the previously used catalyst. Together, these steps yield the same result as the proton-proton cycle, only at somewhat different reaction rates. More specifically, for the CNO cycle to be more efficient than the proton-proton chain, slightly higher temperatures than those in the Sun are required.

Triple-Alpha Process

Another very important fusion process that occurs in older stars is the triple-alpha process. Here, three helium nuclei are combined into a carbon nucleus,

$$3\,{}^4_2\mathrm{He} \longrightarrow {}^{12}_6\mathrm{C} + 7.4\,\mathrm{MeV} \quad .$$

The triple-alpha process is the link between the production of helium and that of heavier elements. The first generation of stars after the Big Bang had no initial helium abundance; thus, heavier elements could be bred only after those stars had undergone their triple-alpha phase.

1.1.2 Power Plants: Deuterium and Tritium

On Earth, it is significantly more difficult to create an environment in which controlled fusion reactions happen at a reasonably high rate. Stars are held together by their own gravity and mostly do not fuse their nuclear material very efficiently; this fact is illustrated by their long lifetime. Terrestrial fusion, however, needs to be implemented on much smaller spatial scales and at the highest possible efficiency. The latter can be achieved by selecting the reaction with the largest cross-section while optimizing temperature and pressure.
Fig. 1.2 shows how the cross-sections of different fusion reactions depend on the temperature. Clearly, D-T fusion is the most efficient reaction unless one plans on venturing into temperature ranges which are extremely difficult to access. From the reaction equation,

$${}^2_1\mathrm{D} + {}^3_1\mathrm{T} \longrightarrow {}^4_2\mathrm{He} + {}^1_0\mathrm{n} + 17.6\,\mathrm{MeV} \quad ,$$

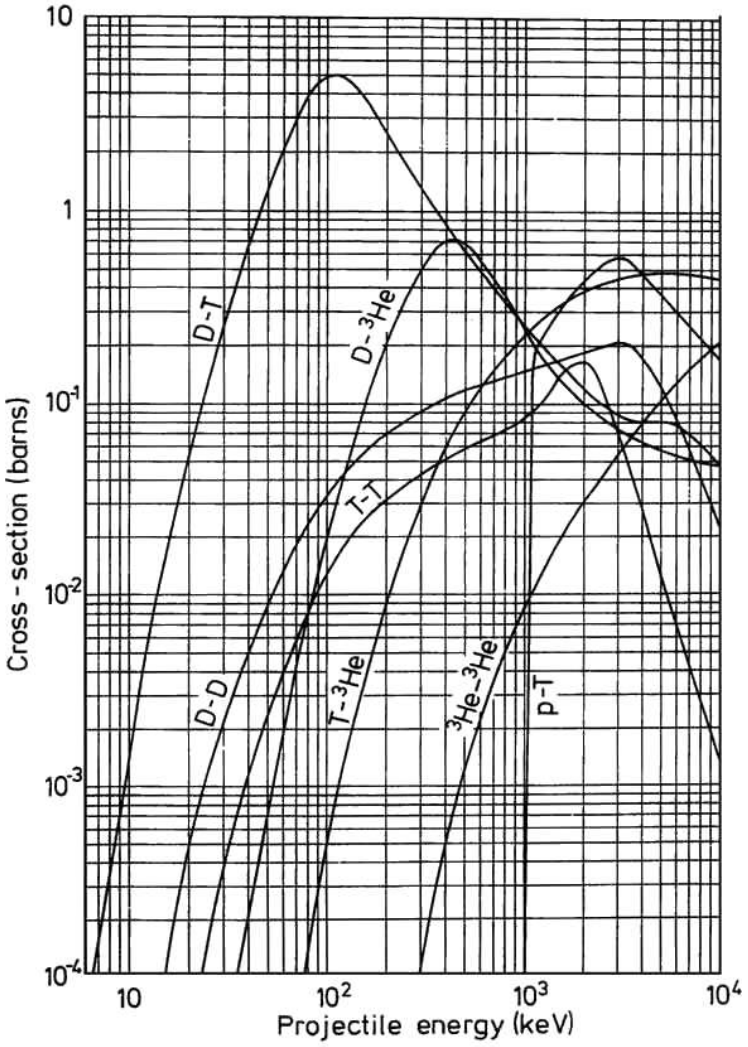

Figure 1.2: Cross sections of fusion reactions involving light elements as a function of the energy of one participant in the rest frame of the second participant. D-T fusion is the most efficient reaction in this energy range. Source: [2]

one can infer that no weak interaction processes occur which would strongly reduce the reaction rate. Another useful feature of D-T fusion is that the reaction produces a fast neutron, carrying 14.1 MeV, or four fifths, of the total kinetic energy. This provides the means to extract energy from the reactor by making use of the heat created by those same neutrons when they collide with the reactor walls.

One can use the Lawson criterion to estimate the required conditions for a burning plasma; in this state, the energy losses to the environment are (over-)compensated by the energy released in the fusion reactions. For a D-T plasma, the criterion reads

$$n_{\mathrm{e}} T \tau_E \geq 10^{21}\,\mathrm{keV\,s/m^3} \quad . \tag{1.1}$$

Thus, for given temperature T and density n_{e}, one has to maximize the energy confinement time τ_E (which is the duration over which the plasma energy, measured at one point of time, remains in the system) to maximize the efficiency of a fusion reactor.

Going from stellar to terrestial scales is more difficult, for gravity can no longer hold the plasma together; confinement of the fusion material is still the subject of ongoing research. The most promising approach is to confine a hot plasma by the use of magnetic fields to insulate it from the reactor walls. An alternative concept is to create fusion conditions only for a very short time – maximizing efficiency instead by increasing the other quantities in the Lawson criterion, density and temperature – in a non-equilibrium fashion. This is achieved by heating a D-T pellet with strong lasers, with the material fusing until the density is becoming too low due to the resulting expansion. The focus of this thesis, however, lies on magnetic confinement.

1.2 Magnetic Confinement Research

Generally, there are two concepts of confining a plasma in a magnetic field: one can either construct a magnetic mirror, or one needs to create a toroidal field structure. The Earth's atmosphere is an example of the former, shielding the planet from energetic particles. However, using that principle to build a fusion reactor has failed mostly due to the problem that it is not possible to maintain an anisotropic velocity distribution sufficiently long which is required for the mirror effect to confine the plasma.

1.2.1 Tokamak and Stellarator

Turning to toroidal configurations, one finds that simply bending a homogeneous cylindrical magnetic field to a torus leads to drift effects due to the ∇B and curvature drifts; the resulting drift velocities for a particle of mass m and charge q, moving in a magnetic field $\mathbf{B}$ with velocity components $v_{\parallel}$ parallel and $v_{\perp}$ perpendicular to the field, read

$$\mathbf{v}_{\nabla B} = \frac{mcv_{\perp}^2}{2qB}\frac{\mathbf{B}\times\nabla B}{B^2} \quad , \tag{1.2}$$

$$\mathbf{v}_c = \frac{mcv_{\parallel}^2}{qB}\frac{\mathbf{B}\times\nabla B}{B^2} \quad , \tag{1.3}$$

where c denotes the speed of light. Due to the charge dependency, these drifts separate particles of opposite electrical charge, resulting in electric fields perpendicular to the magnetic field. This induces an $\mathbf{E}\times\mathbf{B}$ drift,

$$\mathbf{v}_E = c\,\frac{\mathbf{E}\times\mathbf{B}}{B^2} \quad . \tag{1.4}$$

These drifts usually destroy the confinement within a fraction of a second. To cancel this effect, two concepts have been developed, the tokamak and the stellarator.

In a tokamak, an induced toroidal electric current – i.e., a current along the magnetic axis – creates an additional magnetic field in the poloidal direction (see Fig. 1.3), with the resulting combined field canceling the drift. The advantage to this concept is that only planar magnetic coils are required. For power plants, superconducting magnets are a necessity to provide reasonable efficiency, and non-planar coils are very challenging to manufacture. However, since the current required to produce the poloidal field is being induced via a transformer coil, the current in said coil has to be constantly increased, putting a severe constraint on the operation time. Methods to circumvent this constraint are being developed, generating internal transport barriers in the plasma which in turn cause a so-called bootstrap current. This toroidal current reduces the required externally induced current, prolonging the maximal operation time.

Alternatively, one can avoid the necessity for inducing a current by constructing a complex external magnetic field; this concept is called stellarator (see Fig. 1.4). The advantage of continuous operation is achieved at the expense of using magnetic field coils of non-trivial shape.

At present, the tokamak concept is developed much further than the stellarator; however, knowledge gained from stellarator experiments will likely be an important factor in operating tokamaks continuously, i.e., without externally induced current.

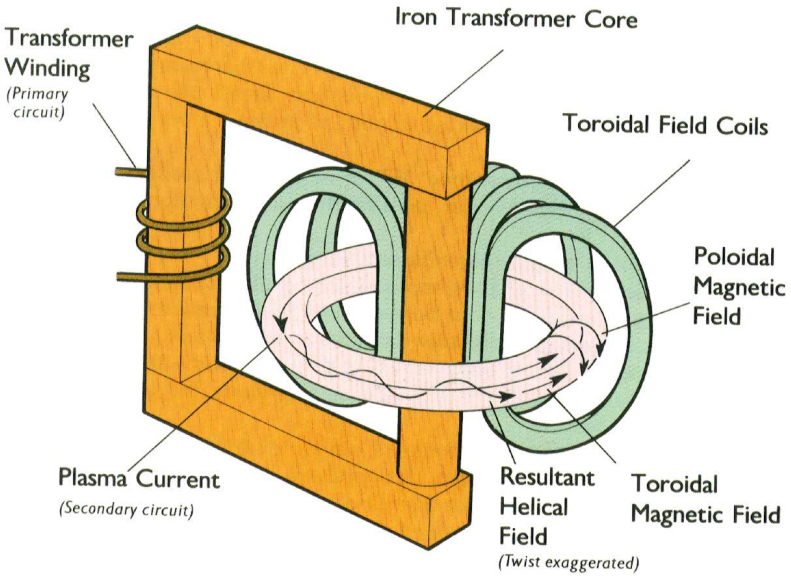

Figure 1.3: Basic concept of a tokamak fusion device. A toroidal magnetic field created by external field coils is combined with a poloidal field. The latter is due to a current which is induced in the plasma via a central transformer coil. The net ∇B drift for a particle in such a configuration is zero. Source: [3]

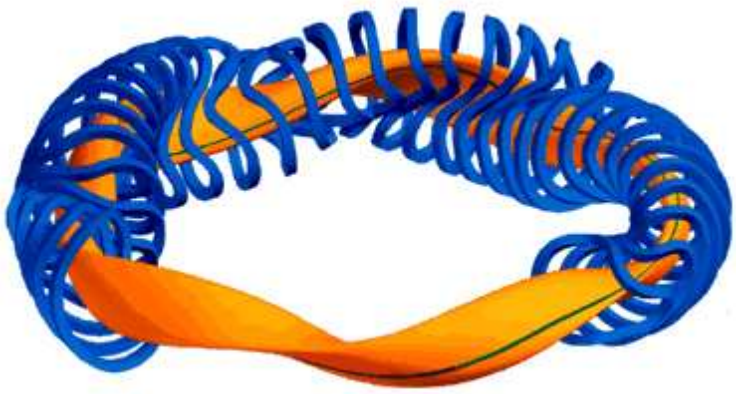

Figure 1.4: Shapes of the magnetic field coils and a magnetic flux surface for the Wendelstein 7-X stellarator. While here, no induced toroidal current is required, the complex shape of the coils makes the stellarator a challenging concept from an engineering point of view. Source: [4]

1.2.2 Fusion Experiments

The first fusion experiments were built in the late forties and early fifties of the twentieth century, with research mostly being classified. Initially, mainly pinch devices were investigated, but they were abandoned later when it became apparent that they were intrinsically unstable. A decade after it was decided that fusion research was safe to be declassified, the Russian T-3 machine – one of the first tokamaks – was put into operation in 1958, starting a concept line that now is the most progressed in the field. Current examples include the European cooperation JET, based in the United Kingdom, ASDEX Upgrade in Germany, DIII-D in the U.S., and JT-60 in Japan. The international project ITER [5] is presently under construction; it will be the largest fusion experiment on Earth and is expected to produce more energy in fusion reactions than is required to power its heating systems, achieving a fusion energy gain factor of

$$Q = \frac{P_{\text{fusion}}}{P_{\text{heating}}} \sim 10 \quad . \tag{1.5}$$

With ITER, the community hopes to advance knowledge in the areas of reactor engineering, steady state operation, and Edge Localized Mode control (for reviews on ELMs, see Refs. [6] and [7]), as well as showcase safety and environmental properties. In a next step, a demonstration reactor, DEMO, is planned in order to prove that fusion reactors are economically viable.
The stellarator line goes back to a concept by Lyman Spitzer, with the first device built in 1951. However, the complex shape required for the magnetic coils slowed down progress in this area. The Wendelstein 7-X machine is currently under construction in Germany; its size is similar to tokamaks that were built more than a decade ago, and the stellarator line is not expected to catch up with tokamak experiments in the near or intermediate future. However, if Wendelstein 7-X is successful, it will significantly increase the chances of future stellarator-based commercial reactors, as well as give strong support to the tokamak line via the cross-concept application of experimental results.

1.3 The Need for an Emission-Free Energy Source

1.3.1 The Global Energy Situation

One of the primary reasons why fusion research is being conducted is the pressing problem to satisfy the growing energy needs of humanity while reducing carbon emissions drastically to avoid severe effects due to climate change. Currently,

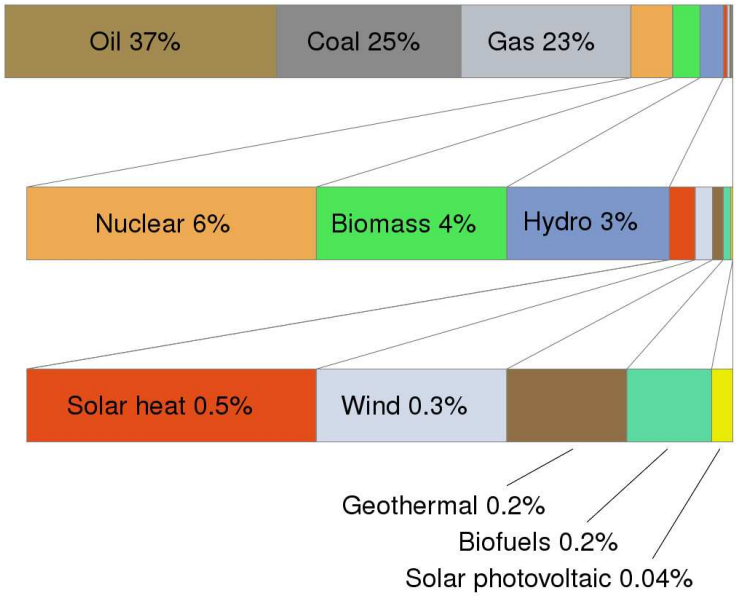

Figure 1.5: Global energy source composition. The vast majority is provided by burning fossil fuels (oil, coal, gas), a process that produces significant carbon emissions. Biomass, despite its technical carbon-neutrality, also adds to the emitted carbon. Of the remaining sources, only nuclear and hydro energy play a significant role. Source: [8]

more than four fifths of the world-wide energy consumption are fueled by resources that are both limited and carbon-emitting. While the amount of total consumed energy is strongly increasing, it has been estimated that emissions have to be cut by at least fifty percent in the next four decades (see, e.g., the findings of the Intergovernmental Panel on Climate Change [9]) to stabilize the planet's climate.

Possible routes to achieving this goal are connected to a strong reliance on non-fossil energy sources. Wind, solar heat, or photovoltaic power, however, can not be used to supply the world's base load without significant power storage capacities, and even then they are limited in scope. Fusion power, while not expected to be able to contribute significantly until the second half of the century, would provide humanity with a sustainable and risk-free energy source.

1.3.2 Environmental and Safety Aspects of Fusion

Environmental Impact

Fusion is inherently emission-free – only very small quantities of the inert helium are produced in the reactions, and the materials to fuel the reactor are obtainable without significant environmental impact: deuterium can be extracted from seawater via electrolysis, and tritium is bred from lithium inside the reactor building using the neutrons from the fusion reactions. Lithium is found both in the Earth's crust and in seawater. Taking all available Deuterium and Lithium sources, and considering 5000 power plants providing a global energy solution (each producing 1 GW while using 110 kg of Deuterium and 380 kg of Lithium per year at perfect efficiency), D-T fusion could be employed for 50 million years (for more details, see Ref. [10]).
The only concern stems from the reactor walls which – due to the high neutron fluxes – experience alterations in their nuclear structure over time, resulting in radiological activity. However, this effect is in no way comparable with the corresponding activity in fission plants. Fig. 1.6 shows the decay of radioactivity for fusion and fission plants, compared with the natural activity of coal ash. While fission plant components must be stored for millennia before the material can be reused, the storage period for fusion plant components can be estimated to be around fifty to a hundred years. After only five hundred years, their levels have dropped to those of coal ash, making the radiotoxicity of fusion-related waste a very benign problem, though not completely negligible.

Safety and Worst-Case Scenario

The 1986 accident at the Chernobyl nuclear power plant has since become a symbol of the dangers related to fission power. Due to failing control mechanisms, a runaway reaction occurred, resulting in immediate vaporization of the pressurized coolant, thus compromising the integrity of the reactor building. In this context, it becomes clear that prior to building fusion reactors, the possible consequences of mishandling such a device need to be investigated.
Such research has been undertaken, with rather clear results. Bartels et al. [11] studied 25 reference accidents with respect to their potential release of radioactive material. Those scenarios can roughly be divided up into the following categories: plasma events (which have no environmental release risk), loss of power (with no external effects even if backup generators fail), leaks in the coolant cycle (where in the worst conceivable case, release of tritiated water (HTO) is limited to an acceptable level of $\sim$ 5 grams), loss of vacuum (with even lower release),

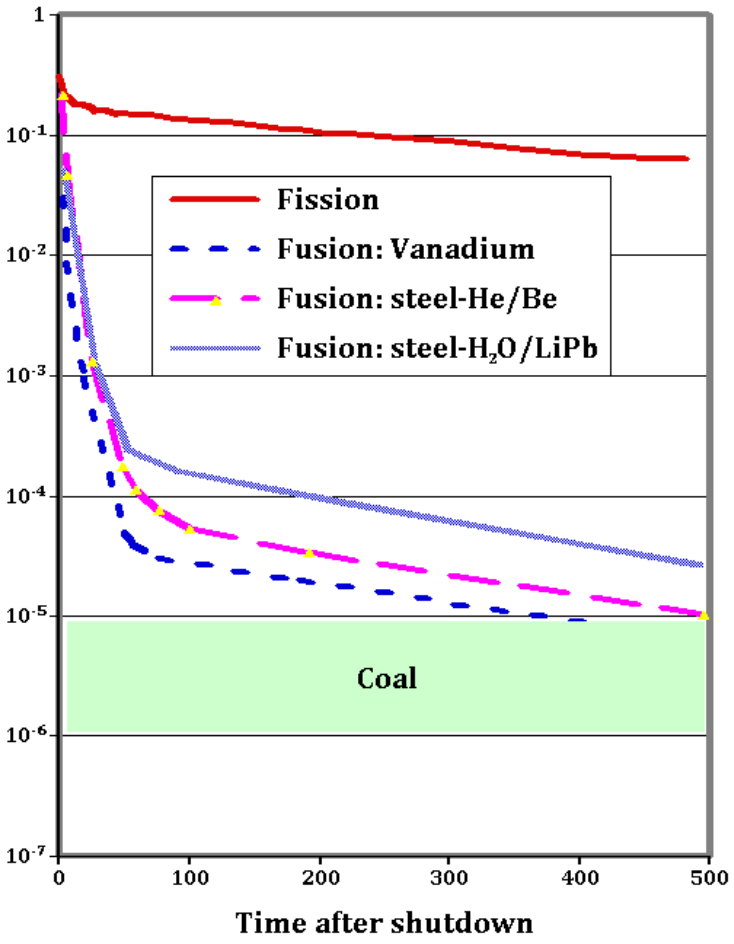

Figure 1.6: Decrease of the radiotoxicity (in arbitrary units) of reactor material over time for different reactor types. Shown are a fission reactor (based on the concept of water pressurization which is the most common nuclear power plant type) in addition to three different fusion reactor types, distinguishable by the steel used for the reactor vessel; also, the natural level of coal ash is included for comparison. Source: IPP

maintenance accidents (which, in terms of potential release, constitute a risk similar to that connected with the loss of vacuum), and magnet malfunction (no release risk). Similarly, advanced tokamak scenarios (see Ref. [12]) are designed to operate at risk levels where evacuation plans are obsolete. For more information on reactor safety, see Ref. [10] and references therein.
Clearly, magnetic confinement fusion technology will not be able to cause any damage that could in the least be compared with the Chernobyl catastrophe.

1.4 Simulation of Fusion Plasmas

In the field of fusion research, an increasing interaction between experiment and theory can be observed. Numerical and analytical investigations are required to improve the understanding of observed phenomena, as well as to help optimize concepts for future devices. Following Tang and Chan [13], a brief overview of aspects of research in the two most prominent theoretical frameworks, magneto-hydrodynamic (MHD) and kinetic theory, is given.
Macroscopic physics of fusion reactors are described well in the context of MHD, using hydrodynamic quantities – density, pressure, and velocity field – in conjunction with Maxwell's equations. This excludes effects connected to non-Maxwellian distribution functions. Large-scale disruptions (e.g., ELMs) can be understood that way, enabling theorists to look for ways to avoid such instabilities. The non-linear evolution of magnetic islands (see Ch. 7 for more information on islands and references), which enhance radial transport, is usually studied using MHD models. And magnetic reconnection may also be explored in this fashion.
Often, neoclassical theory (see, e.g., Wang et al. [14]) is used to augment MHD by describing collisional heat transport. Specifically, particles on so-called banana orbits contribute to such transport; these particles are reflected by the higher magnetic field on the inside of the torus, and are thus caught on orbits which resemble those of cosmic particles in the Earth's atmosphere.
However, even when a magnetic confinement configuration is stable according to the predictions made by MHD, transport levels are observed which exceed neoclassical expectations significantly. This effect is a result of microturbulent phenomena in the plasma, causing anomalous transport. In order to study the underlying physics, kinetic models must be employed which take into account non-Maxwellian velocity space properties. Generally, kinetic simulations fall into two categories: Particle-in-Cell and Vlasov. The latter does not compute single particle orbits but instead operates on the particle distribution functions directly by solving the Vlasov equation. Both types may be simplified by averaging over

the fast gyromotion of particles about magnetic field lines, an approximation which retains all physically relevant scales but reduces the computational effort that is required. Since most of the work presented in this thesis relies on such gyrokinetic Vlasov simulations, a brief derivation of the corresponding equations may be found in Ch. 2.
Additionally, fusion theory covers the investigation of phenomena in the plasma edge, where the magnetic field structure becomes more problematic and the plasma may interact with the reactor wall (see, e.g., Neu et al. [15] for details on plasma-wall interaction). In this case, the inclusion of additional physical models ranging from surface to molecular physics can become necessary.
More details on the diverse aspects of fusion plasma simulations are available in publications by Dinklage et al. [16] and by Batchelor et al. [17].

1.5 Thesis Outline

The remainder of this thesis is structured as follows. First, a brief derivation of gyrokinetic theory is given, starting from the equations of motion for charged particles in electromagnetic fields, and – via gyroaveraging – arriving at the gyrokinetic Vlasov equation, along with the corresponding field equations. A description of the GENE (Gyrokinetic Electromagnetic Numerical Experiment) code follows, a numerical solver of the gyrokinetic equations; most of the work presented in this thesis is based on results obtained with the GENE code. The visualization of simulation data is detailed in a separate chapter, with a description of the GENE Diagnostics Tool and available diagnostics, as well as another visualization program, the RZG VisualKit. Next, numerical diffusion is discussed, with an emphasis on parallel (hyper-)diffusion terms used to suppress the unphysical effect of high-$k_\parallel$ structures. Similarly, parallel velocity space diffusion is investigated with the intent of avoiding numerical recurrence. Then, simulation results are presented from electromagnetic GENE runs, covering two distinct parameter sets, with an in-depth analysis of physical and numerical effects; linearly, special focus is put on the onset of kinetic ballooning modes, while nonlinearly, investigations into turbulent transport levels are performed. This is followed by additional studies of the properties of electromagnetic plasma turbulence. Before concluding, two applications to astrophysics are discussed briefly, where the GENE code can be used to describe cross-field transport in galactic cooling flows and evaporating clouds.

Chapter 2

Gyrokinetics and the GENE Code

Before giving a description of the GENE code – which was used to obtain most of the results reported in this thesis – a brief derivation of the gyrokinetic framework is presented: after a coordinate transform using the Lie formalism, the fast gyromotion of particles in magnetic fields is integrated out, reducing the dimensionality of the system by one. The Vlasov equation is given in its general form, as well as normalized and in flux tube geometry to allow for numerical treatment.

2.1 Gyrokinetic Theory

The basic idea of gyrokinetics is to assume that the gyromotion of a particle about a magnetic field line sets the fastest time scale in the system, and turbulent frequencies are much lower. In this case, one may describe the particle by substituting a charged ring with the same radius as the gyromotion, moving along the field line (see Fig. 2.1) and being subjected to drift effects. For some applications, it is sufficient to turn to a drift-kinetic approach, where only the motion of the gyrocenter is considered, corresponding to the long-wavelength limit of gyrokinetics.

Gyrokinetic theory was originally derived in the 1980s. Lie transformations (as detailed in Refs. [18–21]) are used to isolate and remove any dependence on the gyroangle θ and thus reduce the number of dimensions by one. The original work can be found in Refs. [22–24], with a more recent review available by Brizard and Hahm [25]. Following Dannert [26] and Pueschel [27], a summary of the derivation is given below.

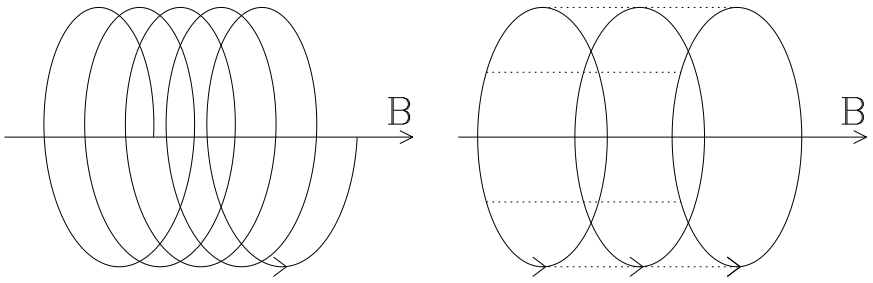

Figure 2.1: Basic idea of the gyrokinetic approximation: instead of following particles on their spiral-shaped trajectory about magnetic field lines, the fast orbital motion is averaged over, retaining all frequencies that are small compared to the gyrofrequency. In other words, instead of orbiting particles, one follows charged circles which move along the magnetic field lines.

2.1.1 Lagrangian and One-Form

In order to separate physical scales that are connected to different aspects of a particle's motion, one must choose a coordinate system that reflects the scale separation. For a particle moving in a magnetic field, the most obvious choice is to go to field aligned coordinates. Here, a local Cartesian coordinate system $(\mathbf{e}_1, \mathbf{e}_2, \mathbf{b})$ is used with $\mathbf{b} = \mathbf{B}/B$ pointing in the direction of the magnetic field $\mathbf{B}$. Thus, the position vector of a gyrating particle points in the direction of $\mathbf{a}(\theta) = \mathbf{e_1}\cos\theta - \mathbf{e_2}\sin\theta$, and its gyration velocity is parallel to $\mathbf{c}(\theta) = -\mathbf{e_1}\sin\theta - \mathbf{e_2}\cos\theta$, with θ denoting the gyroangle.
The Langrangian of a particle – with mass m, charge q, spatial position $\mathbf{x}$, and velocity $\mathbf{v}$ – in an electromagnetic field can be written as

$$\mathcal{L}(\mathbf{x}, \mathbf{v}) = \left(m\mathbf{v} + \frac{q}{c}\mathbf{A}(\mathbf{x}) \right) \cdot \dot{\mathbf{x}} - \mathcal{H}(\mathbf{x}, \mathbf{v}) \quad , \tag{2.1}$$

with the Hamiltonian

$$\mathcal{H}(\mathbf{x}, \mathbf{v}) = \frac{mv^2}{2} + q\Phi(\mathbf{x}) \quad . \tag{2.2}$$

Here, $\mathbf{A}(\mathbf{x})$ and $\Phi(\mathbf{x})$ correspond to the magnetic and electrostatic potential, respectively. It proves advantageous to switch to a one-form formulation,

$$\int \mathcal{L}(\mathbf{x}, \mathbf{v}) \mathrm{d}t = \int \gamma \quad . \tag{2.3}$$

The one-form $\gamma = \gamma(\mathbf{x}, \mathbf{v})$ can be transformed to the so-called gyrocenter coordinates $(\mathbf{X}, v_\parallel, \mu, \theta)$, where $\mathbf{X}$ denotes the gyrocenter position, $v_\parallel$ its velocity

component along $\mathbf{b}(\mathbf{x})$, and $\mu = mv_\perp^2/(2B)$ the magnetic moment. $v_\perp$ is the perpendicular velocity component. It is assumed that the electromagnetic fields vary on a scale much larger than the gyroradius $\rho = v_t\Omega^{-1}$, where $v_t = (T/m)^{1/2}$ is the thermal velocity at temperature T and $\Omega = qB/(mc)$ is the gyrofrequency. Consequently, $\Phi(\mathbf{x}) \approx \Phi(\mathbf{X})$, with the same being valid for $\mathbf{A}$.
In terms of these new coordinates, the old coordinates can be written as

$$\mathbf{x} = \mathbf{X} + \rho(\mathbf{X})\mathbf{a}(\theta) \quad , \tag{2.4}$$

$$\mathbf{v} = v_\parallel \mathbf{b}(\mathbf{X}) + v_\perp(\mathbf{X}, \mu)\mathbf{c}(\theta) \quad . \tag{2.5}$$

With the indices i and j going over the three spatial and three velocity coordinates, as well as the time coordinate t, the transformation becomes

$$\Gamma = \sum_j \Gamma_j = \sum_j \sum_i \gamma_i \frac{\mathrm{d}x_j}{\mathrm{d}X_i} \quad . \tag{2.6}$$

These derivatives can be calculated in a straightforward fashion using the above relations. After averaging over the gyromotion – i.e., performing integrals of the form

$$\Gamma_i \to \frac{1}{2\pi} \int_0^{2\pi} \Gamma_i \mathrm{d}\theta \quad , \tag{2.7}$$

which cancels all terms proportional to either $\mathbf{a}(\theta)$ or $\mathbf{c}(\theta)$ due to the θ-periodic function contained therein – the following expression remains:

$$\begin{aligned} \Gamma = &- \left(\frac{mv_\parallel^2}{2} + \mu B(\mathbf{X}) + q\Phi(\mathbf{X}) \right) \mathrm{d}t + \\ &+ \left(mv_\parallel \mathbf{b}(\mathbf{X}) + \frac{q}{c}\mathbf{A}(\mathbf{X}) \right) \mathrm{d}\mathbf{X} + \frac{\mu B(\mathbf{X})}{\Omega(\mathbf{X})} \mathrm{d}\theta \quad . \end{aligned} \tag{2.8}$$

This calculation can be performed analogously using a perturbed initial one-form, with perturbed fields

$$\Phi(\mathbf{x}) \to \Phi_0(\mathbf{x}) + \Phi_1(\mathbf{x}) \quad , \quad \mathbf{A}(\mathbf{x}) \to \mathbf{A}_0(\mathbf{x}) + \mathbf{A}_1(\mathbf{x}) \quad . \tag{2.9}$$

Equilibrium electric fields – which do not occur in the physical scenarios under consideration – are removed by setting $\Phi_0(\mathbf{x}) = 0$. According to the gyrokinetic ordering, the above perturbations are assumed to be small compared with the equilibrium fields,

$$\frac{q\Phi_1}{T_0} \sim \frac{\|\mathbf{A}_1\|}{\rho B_0} \sim \epsilon \ll 1 \quad . \tag{2.10}$$

However, this assumption does not apply to the perpendicular gradients of the equilibrium and the perturbed parts, which is why the perturbed fields have to

be taken at the precise particle position (i.e., $\Phi_1(\mathbf{x}) \neq \Phi_1(\mathbf{X})$ in general, with the same applying to the perturbation of the magnetic potential).
Naturally, applying the assumption in Eq. (2.9) to the one-form and performing the same transformation as before, the resulting equilibrium one-form Γ_0 is identical to the original result as given in Eq. (2.8). Defining $\mathbf{r} = \rho\mathbf{a}(\theta)$ to be the particle position relative to the gyrocenter, the perturbed part reads

$$\Gamma_1 = \frac{q}{c}\mathbf{A}_1(\mathbf{X}+\mathbf{r})\mathrm{d}\mathbf{X} + \frac{\mathbf{a}(\theta)\cdot\mathbf{A}_1(\mathbf{X}+\mathbf{r})}{v_\perp(\mathbf{X},\mu)}\mathrm{d}\mu + \\ + \frac{mv_\perp(\mathbf{X},\mu)}{B_0(\mathbf{X})}\mathbf{A}_1(\mathbf{X}+\mathbf{r})\cdot\mathbf{c}(\theta)\mathrm{d}\theta - q\Phi_1(\mathbf{X}+\mathbf{r})\mathrm{d}t \quad . \tag{2.11}$$

Unlike Γ_0, the above Γ_1 still contains θ-dependent terms which cannot be integrated out by performing the simple average as above. In order to dispose of these terms, one can employ a Lie transform with a suitable gauge function, as is demonstrated below. Note that in this work, only perturbations of order ϵ are considered, while higher orders are neglected.

2.1.2 Lie Transform

A Lie transform constitutes a near-identity coordinate transform and is defined as follows, along with its effect on one-forms:

$$T = \mathrm{e}^{\epsilon G} \quad , \quad \bar{\Gamma} = T^{*-1}\Gamma + \mathrm{d}S \quad , \tag{2.12}$$

with $\epsilon \ll 1$, a generator G, and a scalar gauge function $\mathrm{d}S$. From this, a tangent map and its pullback operator are obtained, respectively:

$$T_* = \mathrm{e}^{-\epsilon L_G} \quad , \quad T^* = \mathrm{e}^{\epsilon L_G} \quad , \tag{2.13}$$

with the Lie derivative L_G acting on the one-form (in a system with coordinates X_i) according to

$$(L_G\Gamma)_i = \sum_j G^j\left(\frac{\partial\Gamma_i}{\partial X^j} - \frac{\partial\Gamma_j}{\partial X^i}\right) \quad . \tag{2.14}$$

Expanding both one-forms and $\mathrm{d}S$ into an equilibrium and a perturbation part, and ordering the resulting terms (keeping only those up to $\mathcal{O}(\epsilon)$), one gets

$$\bar{\Gamma}_0 = \Gamma_0 + \mathrm{d}S_0 \quad , \tag{2.15}$$

$$\bar{\Gamma}_1 = \Gamma_1 - L_1\Gamma_0 + \mathrm{d}S_1 \quad . \tag{2.16}$$

This formalism is now applied to the original Γ_0 and Γ_1 (as given in Eq. (2.11)); it follows immediately that $\mathrm{d}S_0 = 0$, while for the first order,

$$\bar{\Gamma}_{1i} = \Gamma_{1i} - \sum_j G^j\left(\frac{\partial\Gamma_i}{\partial X^j} - \frac{\partial\Gamma_j}{\partial X^i}\right) \quad , \quad X_i, X_j \in \{\mathbf{X}, v_\parallel, \mu, \theta\} \quad . \tag{2.17}$$

Since the time t remains unchanged, it is not included in the X_i. Performing all the derivatives, and introducing

$$\mathbf{A}_0^* = \mathbf{A}_0 + \frac{mc}{q} v_\parallel \mathbf{b}_0 \quad , \quad \mathbf{B}_0^* = \nabla \times \mathbf{A}_0^* \quad , \tag{2.18}$$

one arrives at

$$\bar{\Gamma}_{1t} = -q\Phi_1(\mathbf{X}+\mathbf{r}) + \nabla(\mu B_0)\cdot G^{\mathbf{X}} + m v_\parallel G^{v\parallel} + B_0(\mathbf{X}) G^\mu + \frac{\partial S_1}{\partial t} \tag{2.19}$$

$$\bar{\Gamma}_{1\mathbf{X}} = \frac{q}{c}\Big(\mathbf{A}_1(\mathbf{X}+\mathbf{r}) - \mathbf{B}_0^* \times G^{\mathbf{X}}(\mathbf{X}+\mathbf{r})\Big) - m\mathbf{b}_0(\mathbf{X}) G^{v\parallel} + \nabla S_1 \tag{2.20}$$

$$\bar{\Gamma}_{1v\parallel} = m\mathbf{b}_0(\mathbf{X})\cdot G^{\mathbf{X}} + \frac{\partial S_1}{\partial v_\parallel} \tag{2.21}$$

$$\bar{\Gamma}_{1\mu} = \frac{\mathbf{a}(\theta)\cdot\mathbf{A}_1(\mathbf{X}+\mathbf{r})}{v_\perp(\mathbf{X},\mu)} + \frac{mc}{q} G^\theta + \frac{\partial S_1}{\partial \mu} \tag{2.22}$$

$$\bar{\Gamma}_{1\theta} = \frac{m v_\perp(\mathbf{X},\mu)}{B_0(\mathbf{X})}\mathbf{c}(\theta)\cdot\mathbf{A}_1(\mathbf{X}+\mathbf{r}) - \frac{mc}{q} G^\mu + \frac{\partial S_1}{\partial \theta} \tag{2.23}$$

This resulting one-form $\bar{\Gamma}_1$ now needs to be made independent of the gyroangle θ through corresponding choice of the generator and the gauge function. Additional freedom is used to obtain a comparatively simple one-form is by requiring $\bar{\Gamma}_{1v\parallel} = \bar{\Gamma}_{1\mu} = \bar{\Gamma}_{1\theta} = 0$. These conditions lead to equations for $G^{\mathbf{X}}$, G^θ, and G^μ which – together – contain all velocity space derivatives of S_1 and are subsequently inserted into the equations for the remaining components of $\bar{\Gamma}_1$. Keeping in mind the purpose of employing the Lie transform, another requirement is added,

$$\bar{\Gamma}_{1\mathbf{X}} = \frac{q}{2\pi c}\int_0^{2\pi} \mathbf{A}_1(\mathbf{X}+\mathbf{r})\mathrm{d}\theta \quad , \tag{2.24}$$

which imposes conditions on $G^{v\parallel}$ and $G^{\mathbf{X}}$. Lastly, the time component is considered. Looking at the order of the different terms containing derivatives of the gauge function, one can see that the θ derivative is larger than the other terms by a factor of ϵ; thus, the other terms are dropped, resulting in

$$\begin{aligned}
\bar{\Gamma}_{1t} = {} & -q\Phi_1(\mathbf{X}+\mathbf{r}) - \\
& - \frac{1}{B_{0\parallel}^*}\nabla(\mu B_0)\cdot\left[\mathbf{b}_0(\mathbf{X})\times\left(\mathbf{A}_1(\mathbf{X}+\mathbf{r}) - \frac{1}{2\pi}\int_0^{2\pi}\mathbf{A}_1(\mathbf{X}+\mathbf{r})\mathrm{d}\theta\right)\right] + \\
& + \frac{q v_\parallel}{c}\frac{\mathbf{B}_{0\parallel}^*}{B_{0\parallel}^*}\cdot\left(\mathbf{A}_1(\mathbf{X}+\mathbf{r}) - \frac{1}{2\pi}\int_0^{2\pi}\mathbf{A}_1(\mathbf{X}+\mathbf{r})\mathrm{d}\theta\right) + \\
& + \frac{q v_\perp}{c}\mathbf{c}(\theta)\cdot\mathbf{A}_1(\mathbf{X}+\mathbf{r}) + \Omega\frac{\partial S_1}{\partial\theta} \quad .
\end{aligned} \tag{2.25}$$

Requiring that all terms containing a difference between a field and its gyroaverage must vanish, a final condition for $\partial S_1/\partial\theta$ is obtained. The gyroaverages are performed for the field terms,

$$\frac{1}{2\pi}\int_0^{2\pi}\Phi_1(\mathbf{X}+\mathbf{r})\mathrm{d}\theta = J_0(\lambda)\Phi_1(\mathbf{X}) \tag{2.26}$$

$$\frac{1}{2\pi}\int_0^{2\pi}\mathbf{A}_1(\mathbf{X}+\mathbf{r})\mathrm{d}\theta = J_0(\lambda)\mathbf{A}_1(\mathbf{X}) \tag{2.27}$$

$$\frac{qv_\perp}{2\pi c}\int_0^{2\pi}(\mathbf{A}_1(\mathbf{X}+\mathbf{r})\cdot\mathbf{c}(\theta))\,\mathrm{d}\theta = -\mu\mathcal{I}_1(\lambda)B_{1\parallel}(\mathbf{X}) = \mu\frac{2iI_1(i\lambda)}{\lambda}B_{1\parallel}(\mathbf{X}) \tag{2.28}$$

with the Bessel functions $J_0(\lambda)$ and $I_1(i\lambda)$, as well as $\lambda = i\rho\nabla_\perp$. Here, the function $\mathcal{I}_1(\lambda)$ is defined implicitly in relation to $I_1(i\lambda)$. One thus arrives at the final, gyrokinetic one-form:

$$\Gamma = \left(mv_\parallel\mathbf{b}_0(\mathbf{X}) + \frac{q}{c}\mathbf{A}_0(\mathbf{X}) + \frac{q}{c}J_0(\lambda)A_{1\parallel}(\mathbf{X})\mathbf{b}_0(\mathbf{X})\right)\cdot\mathrm{d}\mathbf{X} + \frac{mc}{q}\mu\mathrm{d}\theta - \\ -\left(\frac{mv_\parallel^2}{2} + \mu B_0(\mathbf{X}) + qJ_0(\lambda)\Phi_1(\mathbf{X}) + \mu\mathcal{I}_1(\lambda)B_{1\parallel}(\mathbf{X})\right)\mathrm{d}t \quad . \tag{2.29}$$

This result gives a modified Lagrangian,

$$\mathcal{L} = \frac{q}{c}(\mathbf{A}_0^* + J_0(\lambda)A_{1\parallel}\mathbf{b}_0)\cdot\dot{\mathbf{X}} + \frac{mc}{q}\mu\dot{\theta} - \tag{2.30}$$

$$-\left(\frac{mv_\parallel^2}{2} + qJ_0(\lambda)\Phi_1 + \mu B_0 + \mu\mathcal{I}_1(\lambda)B_{1\parallel}\right) \quad , \tag{2.31}$$

where the variable dependencies have been dropped, since all fields are now to be taken at the gyrocenter position $\mathbf{X}$. Note that henceforth, a bar over a perturbed field quantity denotes gyroaveraging, i.e.: multiplication by the appropriate Bessel function.

2.1.3 The Gyrokinetic Vlasov Equation

In conjunction with the Euler-Lagrange equation, the Lagrangian provides equations for the time derivatives of all phase space coordinates. These derivatives appear in the Vlasov equation, which in the absence of collisions can be written as

$$\frac{\mathrm{d}f}{\mathrm{d}t} = \frac{\partial f}{\partial t} + \dot{\mathbf{X}}\cdot\nabla f + \dot{v}_\parallel\frac{\partial f}{\partial v_\parallel} + \dot{\mu}\frac{\partial f}{\partial\mu} = 0 \quad . \tag{2.32}$$

It states that the phase space volume of a particle distribution function $f = f(\mathbf{X}, v_\parallel, \mu)$ is conserved. Using the definitions of the drift velocities,

$$\mathbf{v}_\chi = -\frac{c}{B_0^2}\nabla\chi_1 \times \mathbf{B}_0 \tag{2.33}$$

$$\mathbf{v}_{\nabla B} = \frac{\mu}{m\Omega}\mathbf{b}_0 \times \nabla B_0 \tag{2.34}$$

$$\mathbf{v}_c = \frac{v_\parallel^2}{\Omega}(\nabla \times \mathbf{b}_0)_\perp \tag{2.35}$$

along with the modified potential

$$\chi_1 = \bar{\Phi}_1 - \frac{v_\parallel}{c}\bar{A}_{1\parallel} + \frac{1}{q}\mu\bar{B}_{1\parallel} \quad , \tag{2.36}$$

and assuming that the perturbed field varies on much smaller scales than the equilibrium field,

$$\bar{A}_{1\parallel}\nabla \times \mathbf{b}_0 \ll (\nabla\bar{A}_{1\parallel}) \times \mathbf{b}_0 \quad , \tag{2.37}$$

one arrives at the three equations

$$\dot{\mathbf{X}} = v_\parallel \mathbf{b}_0 + \frac{B_0}{B_{0\parallel}^*}(\mathbf{v}_\chi + \mathbf{v}_{\nabla B} + \mathbf{v}_c) \tag{2.38}$$

$$\dot{v}_\parallel = \left(\frac{\mathbf{b}_0}{m} + \frac{B_0}{m v_\parallel B_{0\parallel}^*}(\mathbf{v}_\chi + \mathbf{v}_{\nabla B} + \mathbf{v}_c)\right) \cdot \cdot \left(-q\nabla\bar{\Phi}_1 - \frac{q}{c}\mathbf{b_0}\dot{\bar{A}}_{1\parallel} - \mu\nabla(B_0 + \bar{B}_{1\parallel})\right) \tag{2.39}$$

$$\dot{\mu} = 0 \tag{2.40}$$

Inserting these into Eq. (2.32) leads to the standard formulation of the gyrokinetic Vlasov equation, written here for a particle species j:

$$\frac{\partial f_j}{\partial t} + \left(v_\parallel \mathbf{b}_0 + \frac{B_0}{B_{0\parallel}^*}(\mathbf{v}_\chi + \mathbf{v}_{\nabla B} + \mathbf{v}_c)\right) \cdot \cdot \left(\nabla f_j + \frac{1}{m_j v_\parallel}\left(-q_j\nabla\bar{\Phi}_1 - \frac{q_j}{c}\mathbf{b_0}\dot{\bar{A}}_{1\parallel} - \mu\nabla(B_0 + \bar{B}_{1\parallel})\right)\frac{\partial f_j}{\partial v_\parallel}\right) = 0 \quad . \tag{2.41}$$

While some numerical codes solve a normalized version of this equation, it is advantageous to go one step further and split off a Vlasov equation for the perturbed part of the distribution function: $f_j \to f_{j0} + f_{j1}$, with $f_{j1}/f_{j0} \sim \epsilon$, while assuming that the unperturbed part is stationary. Introducing the modified distribution function

$$g_{j1} = f_{j1} - \frac{q_j}{m_j c}\bar{A}_{1\parallel}\frac{\partial f_{j0}}{\partial v_\parallel} \quad , \tag{2.42}$$

and the derived quantity

$$G_{j1} = g_{j1} - \frac{q_j}{m_j v_\parallel}\chi_1 \frac{\partial f_{j0}}{\partial v_\parallel} \quad , \tag{2.43}$$

the perturbed Vlasov equation reads

$$\begin{aligned}
&\frac{\partial g_{j1}}{\partial t} + \frac{B_0}{B^*_{0\parallel}}\mathbf{v}_\chi \cdot \left(\nabla f_{j0} - \frac{1}{m_j v_\parallel}\mu \nabla B_0 \frac{\partial f_{j0}}{\partial v_\parallel}\right) + \\
&\quad + \frac{B_0}{B^*_{0\parallel}}(\mathbf{v}_\chi + \mathbf{v}_{\nabla B} + \mathbf{v}_c)\cdot \nabla G_{j1} + v_\parallel \mathbf{b}_0 \cdot \nabla G_{j1} - \\
&\quad - \left(\frac{1}{m_j}\mathbf{b}_1 + \frac{B_0}{m_j v_\parallel B^*_{0\parallel}}\mathbf{v}_c\right)\cdot \\
&\quad \cdot \left(q_j \nabla \bar{\Phi}_1 + \frac{q_j}{c}\mathbf{b_0}\dot{\bar{A}}_{1\parallel} + \mu \nabla (B_0 + \bar{B}_{1\parallel})\right)\frac{\partial f_{j1}}{\partial v_\parallel} = 0 \quad .
\end{aligned} \tag{2.44}$$

In the presence of collisions, the right hand side has to be substituted with the corresponding collision operator. For convenience, the perturbed parts are subscripted only with the species index j from here on, while continuing to distinguish the equilibrium parts by adding a zero to the subscript.

2.1.4 The Gyrokinetic Field Equations

In a similar fashion as above, one can derive the gyrokinetic field equations from Maxwell's equations, using the same Lie generators as for the Vlasov equation, to form a complete and self-consistent set of equations. Since frequencies comparable and faster than the plasma frequency are removed, quasineutrality can be assumed, i.e., ion and electron charge densities must be identical, $q_\mathrm{i} n_\mathrm{i} = e n_\mathrm{e}$, in the case of a two-species plasma.
Maxwell's equation and quasineutrality contain densities and currents which are defined as moments of the distribution function. By use of the Lie transform $T^* = 1 + \epsilon L_G$, the distribution function can be shifted from the particle position to the gyrocenter. The transformation reads

$$\begin{aligned}
T^*(f_{j0} + f_j) &= (f_{j0} + f_j) + \frac{q_j}{m_j c}(A_\parallel(\mathbf{X}+\mathbf{r}) - \bar{A}_\parallel)\frac{\partial F_{j0}}{\partial v_\parallel} + \\
&+ \frac{1}{B_0}\left(q_j(\Phi(\mathbf{X}+\mathbf{r}) - \bar{\Phi}) - \frac{q_j v_\parallel}{c}(A_\parallel(\mathbf{X}+\mathbf{r}) - \bar{A}_\parallel) - \mu \bar{B}_\parallel\right)\frac{\partial F_{j0}}{\partial \mu} \quad .
\end{aligned} \tag{2.45}$$

Now the equilibrium distribution is assumed to be of Maxwellian type,

$$f_{j0}(v_\parallel, \mu) = \left(\frac{m_j}{2\pi T_j}\right)^{3/2} n_0 \mathrm{e}^{-\frac{m_j v_\parallel^2/2 + \mu B_0}{T_j}} \quad , \tag{2.46}$$

with the species temperature T_j. The velocity derivatives of f_{j0} can be calculated in a straightforward manner. Note that this choice is not a solution of the stationarity assumption about the equilibrium part of Eq. (2.41).
One is then left with the integrals of the distribution function and the fields. Carrying out these integrals while making use of the definition

$$\Gamma_i(b_j) = I_i(b_j)\mathrm{e}^{-b_j} \quad , \quad i = 0, 1 \quad , \quad b_j = -\frac{T_j}{m_j\Omega_j^2}\nabla_\perp^2 \quad , \tag{2.47}$$

with the modified Bessel functions I_0 and I_1, the field equations can be evaluated, giving

$$\sum_j q_j(1-\Gamma_0(b_j))\frac{q_j\Phi}{T_{j0}} = \\ = \sum_j q_j\left((\Gamma_0(b_j)-\Gamma_1(b_j))\frac{B_\parallel}{B_0} + \frac{2\pi B_0}{m_j n_{j0}}\int J_0(\lambda_j) f_j \mathrm{d}v_\parallel \mathrm{d}\mu\right) \tag{2.48}$$

$$\left(1 + \sum_j 4b_j\beta_j(\Gamma_0(b_j)-\Gamma_1(b_j))\right)\frac{B_\parallel}{B_0} = \\ = -\sum_j 2\beta_j\left(\frac{B_0}{n_{j0}T_{j0}}\int \mu\mathcal{I}_1(\lambda_j) f_j \mathrm{d}^3v + \frac{q_j\Phi}{T_{j0}}(\Gamma_0(b_j)-\Gamma_1(b_j))\right) \tag{2.49}$$

$$\nabla_\perp^2 A_\parallel = -\frac{8\pi^2 B_0}{c}\sum_j \frac{q_j}{m_j}\int v_\parallel J_0(\lambda_j) f_j \mathrm{d}v_\parallel \mathrm{d}\mu \tag{2.50}$$

Note that the field equations for Φ and $B_\parallel$ are coupled. For small $\beta_j \equiv 8\pi p_j/B^2 \ll 1$, the parallel magnetic fluctuations are negligible. However, for the higher β values achieved in stellarators or spherical tokamaks, they might have a significant influence, and for some astrophysical scenarios where $\beta > 1$, they are indispensable. First benchmarking exercises have been performed that include $B_\parallel$, but for the results presented in this thesis, $B_\parallel$ fluctuations are neglected.
Together with the Vlasov equation (2.44), the field equations constitute a complete set of equations that can be used to self-consistently advance the distribution functions in time and thereby provide a complete physical description of the evolution of the plasma.

2.2 Flux Tube Geometry

A magnetic equilibrium geometry has to be specified for Eqs. (2.44) and (2.48) to (2.50) before they can be solved numerically. While in principle, one can model a full tokamak geometry, this approach requires an enormous computational effort.

For the work presented here, the described plasma volume is reduced to a flux tube: a spatial domain around a magnetic field line with a parallel extent of 2π or multiples thereof poloidally. While this limits the gyrokinetic framework to local investigations, it retains most of the physical effects. More details on flux tubes can be found in Beer [28], Merz [29], and references therein. Only a few important features shall be mentioned here.

Since a flux tube is confined to the neighborhood of a field line, it is radially local in that it is confined to a small range of flux surfaces. If its radial size is small compared to the major radius R_0 at the magnetic axis, the equilibrium quantities (as well as their gradients) may be assumed to be constant, i.e., the temperature and density profiles can be expressed by scalars. Consequently, it is intuitive to use periodic boundary conditions for the radial coordinate; the same is done for the binormal coordinate, reflecting the toroidal symmetry of fusion reactors.

However, for general values of the safety factor q, the parallel ends of a flux tube do not connect. As a consequence, quasiperiodic boundary conditions are chosen. For representation of the perpendicular coordinates in Fourier space, the conditions read

$$g(k_x, k_y, \pi) = (-1)^{\mathcal{N} k_y L_y/(2\pi)} g(k_x + \mathcal{N} k_y L_y / L_x, k_y, -\pi) \tag{2.51}$$

for a quantity g in a flux tube of parallel size 2π and perpendicular size $L_x \times L_y$ (see Ref. [29] and references therein). Here, x denotes the radial, y the binormal (also: toroidal), and z the parallel coordinate. $\mathcal{N}$ corresponds to the number of identical flux tubes which may be used to cover the entire torus, a property which will be discussed in further detail in Ch. 3.

2.2.1 General Geometry

The magnetic geometry is described by the metric which follows from the well-known Grad-Shafranov equation. In the present work, use is made of both numerical solutions of that equation – modeling specific reactor geometries – and a simplified model discussed below. One efficient way to obtain the required geometry coefficients is to employ the Tracer code which follows the procedure detailed by Xanthopoulos and Jenko [30]. Its output can be read directly by the Gene code which will be described later.

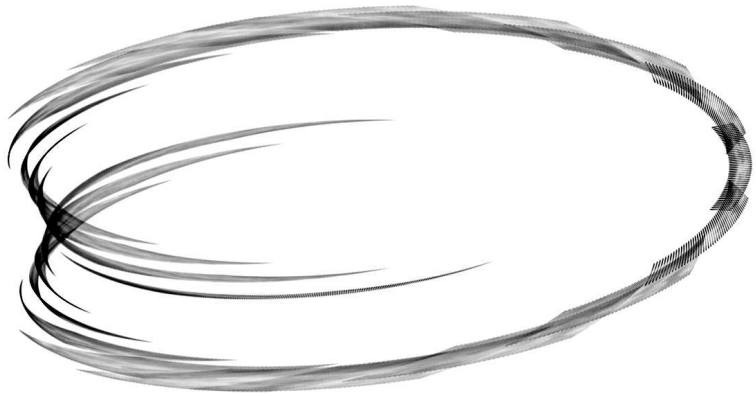

Figure 2.2: $\hat{s}$-α geometry flux tube with turbulent GENE data, as visualized with the RZG VisualKit (see Ch. 3). The scale separation between the parallel and perpendicular coordinates becomes evident in this figure.

2.2.2 $\hat{s}$-α Flux Tubes

In many cases, however, it is sufficient to use a simplified geometry that uses only a constant magnetic shear,

$$\hat{s} = \frac{r_0}{q_0}\frac{\mathrm{d}q(x)}{\mathrm{d}x} \quad , \tag{2.52}$$

to describe the (linear) $q(x)$ profile near a flux surface located at a distance r_0 from the magnetic axis. At finite plasma β, an additional parameter

$$\alpha_{\mathrm{MHD}} = \frac{q_0^2}{R_0}\beta\sum_j(\omega_n + \omega_{T\mathrm{j}})n_{j0}T_{j0} \tag{2.53}$$

is used to describe the Shafranov shift that the flux surfaces are subjected to. Here, the normalized density and temperature gradients are introduced:

$$\omega_{\mathrm{n}} = -\frac{L_{\mathrm{ref}}}{n_{j0}}\frac{\partial n_{j0}}{\partial x} \quad , \quad \omega_{\mathrm{T}j} = -\frac{L_{\mathrm{ref}}}{T_{j0}}\frac{\partial T_{j0}}{\partial x} \quad , \tag{2.54}$$

with the macroscopic length scale L_{ref}, and n_{j0} and T_{j0} are normalized according to the rules detailed below. This so-called $\hat{s}$-α model has been described in detail by Connor et al. [31]. A visualization of an $\hat{s}$-α flux tube is shown in Fig. 2.2. Here, nonlinear simulation data is shown point-wise in global Cartesian space. The center of the flux tube (which is on the far right side in the figure) corresponds the the outboard midplane, i.e., the point farthest away from the reactor center, where the magnetic field strength is at its lowest and thus, turbulence is strongest.

The metric tensor for this case reads

$$g^{ij} = \begin{pmatrix} 1 & \hat{s}z - \alpha_{\mathrm{MHD}} \sin z & 0 \\ \hat{s}z - \alpha_{\mathrm{MHD}} \sin z & 1 + (\hat{s}z - \alpha_{\mathrm{MHD}} \sin z)^2 & 1/r \\ 0 & 1/r & 1/r^2 \end{pmatrix} \tag{2.55}$$

while the magnetic field strength is expressed as a function of the parallel coordinate,

$$B_0 = \frac{1}{1 + \epsilon_t \cos z} \quad , \tag{2.56}$$

with the inverse aspect ratio $\epsilon_t = r_0/R_0$. The parallel boundary condition, Eq. (2.51) requires

$$\mathcal{N} = 2\pi\hat{s}\frac{L_x}{L_y} \quad . \tag{2.57}$$

$\hat{s}$-α geometry is not strictly self-consistent (see, e.g., Merz [29], as well as Lapillonne et al. [32], for more details on limitations of the model). However, it is commonly used as a standard case, and many $\hat{s}$-α results are available in the literature, making it an excellent operation point for cross-code comparisons.

2.3 The GENE Code

For most numerical simulations performed in the context of this thesis, the GENE code (see, e.g., Refs. [33] and [34], as well as Ref. [29] for details on the most recent GENE version) was used. It is an electromagnetic gyrokinetic turbulence code that solves the normalized Vlasov and field equations as given below, making use of large parallel computing devices. In addition to an initial value solver, there exists an eigenvalue solver which provides access to subdominant and stable modes. GENE may be coupled with the aforementioned TRACER code for general geometry investigations, and for postprocessing, the GENE Diagnostics Tool is available which is described in more detail in Ch. 3. Below, the normalized equations are given that GENE is based on, as well as details on the numerical methods which are employed; as only collisionless plasmas are investigated in this thesis, Ref. [29] is referred to for a discussion of the implementation of collisions in GENE.

2.3.1 Normalization of the Equations

Since computer-based calculations have to operate on dimensionless equations, a suitable normalization is used, i.e., one that takes into account the physical scales. However, if one aims to study physical scenarios with widely varying scales, it is

useful to retain some freedom in the normalization; more specifically, reference scales can be chosen according to the specific requirements of a simulation. The normalization rules for the basic variables are

$$\left[\begin{array}{rclrcl} \{x,y\} & \rightarrow & \rho_{\rm ref}\{x,y\} & z & \rightarrow & z \\ v_\parallel & \rightarrow & c_{\rm ref} v_{{\rm T}j} v_\parallel & \mu & \rightarrow & \frac{T_{\rm ref}}{B_{\rm ref}} T_{j0}\mu \\ t & \rightarrow & \frac{L_{\rm ref}}{c_{\rm ref}} t & B_0 & \rightarrow & B_{\rm ref} B_0 \\ q_j & \rightarrow & e q_j & m_j & \rightarrow & m_{\rm ref} m_j \\ n_{j0} & \rightarrow & n_{\rm ref} n_{j0} & T_{j0} & \rightarrow & T_{\rm ref} T_{j0} \end{array}\right] \tag{2.58}$$

Here, e denotes the elementary charge, and the following relations are used:

$$c_{\rm ref} = \left(\frac{T_{\rm ref}}{m_{\rm ref}}\right)^{1/2} \quad , \quad \rho_{\rm ref} = \frac{m_{\rm ref} c_{\rm ref} c}{e B_{\rm ref}} \quad , \quad v_{Tj} = \left(\frac{2T_{j0}}{m_j}\right)^{1/2} \quad . \tag{2.59}$$

The distribution functions and fields are normalized as follows:

$$\left[\begin{array}{rclrcl} \{f_j, g_j\} & \rightarrow & \frac{\rho_{\rm ref}}{L_{\rm ref}} \frac{n_{\rm ref} n_{j0}}{c_{\rm ref}^3 v_{Tj}^3} \{f_j, g_j\} & F_{j0} & \rightarrow & \frac{n_{\rm ref} n_{j0}}{c_{\rm ref}^3 v_{Tj}^3} F_{j0} \\ \{\Phi, \chi\} & \rightarrow & \frac{\rho_{\rm ref}}{L_{\rm ref}} \frac{T_{\rm ref}}{e} \{\Phi, \chi\} & \{A_\parallel, B_\parallel\} & \rightarrow & \frac{\rho_{\rm ref}}{L_{\rm ref}} B_{\rm ref} \{\rho_{\rm ref} A_\parallel, B_\parallel\} \end{array}\right] \tag{2.60}$$

The general normalized form of the plasma pressure is

$$\beta = \frac{8\pi n_{\rm ref} T_{\rm ref}}{B_{\rm ref}^2} \quad , \tag{2.61}$$

and the new form of G_j reads

$$G_j = g_j + \frac{q_j}{T_{j0}} F_{j0} \chi \quad . \tag{2.62}$$

At this point, it shall be noted that for small β, one may neglect the $B_\parallel$ fluctuations (as $B_\perp$ and $\beta B_\parallel$ are of similar magnitude), as well as take $B_{0\parallel}^* \approx B_0$, dropping a term of order $\mathcal{O}(\beta)$.
The curvature terms are defined as follows,

$$\begin{aligned} \mathcal{K}_x &= -\frac{L_{\rm ref}}{B_{\rm ref}} \left(\frac{\partial B_0}{\partial y} + \frac{g^{xx} g^{yz} - g^{yx} g^{xz}}{g^{xx} g^{yy} - g^{yx} g^{xy}} \frac{\partial B_0}{\partial z} \right) \qquad (2.63) \\ &\rightarrow -\frac{L_{\rm ref}}{R_0} \sin z \\ \mathcal{K}_y &= \frac{L_{\rm ref}}{B_{\rm ref}} \left(\frac{\partial B_0}{\partial x} + \frac{g^{xy} g^{yz} - g^{yy} g^{xz}}{g^{xx} g^{yy} - g^{yx} g^{xy}} \frac{\partial B_0}{\partial z} \right) \qquad (2.64) \\ &\rightarrow -\frac{L_{\rm ref}}{R_0} (\cos z + \sin z (\hat{s} z - \alpha_{\rm MHD} \sin z)) \end{aligned}$$

with the relevant z components of the metric g^{ij} normalized to L_{ref}^{-1}; the reduction of the terms in $\hat{s}$-α geometry is specified after the respective definitions. As a result, the normalized Vlasov equation, as solved by the GENE code, reads

$$\begin{aligned}
&\frac{\partial g_j}{\partial t} + \frac{B_0}{B_{0\parallel}^*}\left[\omega_n + \omega_{Tj}\left(v_\parallel^2 + \mu B_0 - \frac{3}{2}\right)\right] F_{j0}\frac{\partial \chi}{\partial y} + \\
&\quad + \frac{B_0}{B_{0\parallel}^*}\left(\frac{\partial \chi}{\partial y}\frac{\partial g_j}{\partial x} + \frac{\partial \chi}{\partial x}\frac{\partial g_j}{\partial y}\right) + \frac{B_0}{B_{0\parallel}^*}\frac{T_{j0}(2v_\parallel^2 + \mu B_0)}{q_j B_0}\cdot \\
&\quad \cdot\left[\mathcal{K}_x\frac{\partial G_j}{\partial x} + \mathcal{K}_y\frac{\partial G_j}{\partial y} - \mathcal{K}_x F_{j0}\left(\omega_n + \omega_{Tj}\left(v_\parallel^2 + \mu B_0 - \frac{3}{2}\right)\right)\right] - \\
&\quad - \frac{B_0}{B_{0\parallel}^*}\frac{T_{j0}v_\parallel^2}{q_j B_0^2}\beta\left(\sum_j n_{j0}T_{j0}(\omega_n + \omega_{Tj})\right)\frac{\partial G_j}{\partial y} - \\
&\quad - \frac{v_{Tj}v_\parallel}{JB_0}\frac{\partial G_j}{\partial z} + \frac{v_{Tj}\mu}{2JB_0}\frac{\partial B_0}{\partial z}\frac{\partial f_j}{\partial v_\parallel} = 0
\end{aligned} \tag{2.65}$$

with the Jacobian $J = B^\phi/B_{\mathrm{ref}}$. The terms can be identified with, in order: the time evolution of the distribution, the driving term, the $\mathbf{E}\times\mathbf{B}$ nonlinearity, the curvature term, the pressure term, the parallel advection term, and the mirror term.

The Vlasov equation is complemented by the normalized field equations,

$$\begin{aligned}
&\left(\frac{B_{\mathrm{ref}}^2}{4\pi c^2 m_{\mathrm{ref}} n_{\mathrm{ref}}}k_\perp^2 + \sum_j \frac{q_j^2 n_{j0}}{T_{j0}}(1 - \Gamma_0(b_j))\right)\Phi - \\
&\qquad - \left(\sum_j \frac{q_j n_{j0}}{B_0}(\Gamma_0(b_j) - \Gamma_1(b_j))\right) B_\parallel = \\
&\qquad = \sum_j \pi q_j n_{j0} B_0 \int J_0(\lambda_j) g_j \mathrm{d}v_\parallel \mathrm{d}\mu
\end{aligned} \tag{2.66}$$

$$\begin{aligned}
&\left(\sum_j \frac{q_j n_{j0}}{B_0}(\Gamma_0(b_j) - \Gamma_1(b_j))\right)\Phi + \\
&\qquad + \left(-\frac{2}{\beta} + \sum_j \frac{2n_{j0}T_{j0}}{B_0^2}(\Gamma_0(b_j) - \Gamma_1(b_j))\right) B_\parallel = \\
&\qquad = -\sum_j \frac{\pi q_j v_{Tj} B_0^{3/2} n_{j0}}{k_\perp}\int \mu^{1/2} J_1(\lambda_j) g_j \mathrm{d}v_\parallel \mathrm{d}\mu
\end{aligned} \tag{2.67}$$

$$A_\parallel = \left(\sum_j \frac{\pi}{2} q_j v_{Tj} n_{j0} B_0 \beta \int v_\parallel J_0(\lambda_j) g_j \mathrm{d}v_\parallel \mathrm{d}\mu\right)\cdot$$

$$\cdot \left(k_\perp^2 + \sum_j \frac{q_j^2}{m_j} \pi n_{j0} B_0 \beta \int v_\parallel^2 J_0(\lambda_j)^2 F_{j0} \mathrm{d}v_\parallel \mathrm{d}\mu \right)^{-1} \tag{2.68}$$

with the square of the perpendicular wavenumber defined as

$$k_\perp^2 = g^{xx} k_x^2 + 2 g^{xy} k_x k_y + g^{yy} k_y^2 \tag{2.69}$$

in Fourier representation. Note that Eqs. (2.66) and (2.67) constitute a system of two coupled equations which may be solved in a straightforward manner.
Since for many applications, it is unnecessary to resolve the full dynamics of both ion and electron species, one may, performing small and large mass limits, respectively, make use of adiabatic responses, which are given by

$$\frac{n_{\mathrm{e1}}^{\mathrm{ad}}}{n_{\mathrm{e0}}} = -\frac{q_{\mathrm{e}}}{T_{\mathrm{e0}}} (\Phi - \langle \Phi \rangle_{\mathrm{flux\,surface}}) \tag{2.70}$$

$$\frac{n_{\mathrm{i1}}^{\mathrm{ad}}}{n_{\mathrm{i0}}} = -\frac{q_{\mathrm{i}}}{T_{\mathrm{i0}}} \Phi \tag{2.71}$$

Technically, knowledge of the distribution functions simultaneously means knowledge of the complete physical state of a system. However, there is no experimental access to the distribution function, and it can be difficult to interpret its physical meaning directly. At the same time, the distribution function data is a seven-dimensional field, with five phase space, one time, and one species dimension, making it a very cumbersome quantity for any analysis. Instead, one usually diagnoses simulations by looking at moments of the distribution or radial flux quantities; prominent examples of the latter are the particle and the heat flux, which one arrives at by multiplying the radial component of the $\mathbf{E}\times\mathbf{B}$ velocity with the perturbed part of the density or pressure, respectively. After performing a spatial average, the results of this prescription read

$$\Gamma_j = -n_{j0} \left(\int J \mathrm{d}z \right)^{-1} \left[\int \sum_{k_x,k_y} i k_y J \chi \left(\pi B_0 \int f_j \mathrm{d}v_\parallel \mathrm{d}\mu \right)^* \right] \tag{2.72}$$

$$Q_j = -n_{j0} T_{j0} \left(\int J \mathrm{d}z \right)^{-1} \left[\int \sum_{k_x,k_y} i k_y J \chi \left(\pi B_0 \int v^2 f_j \mathrm{d}v_\parallel \mathrm{d}\mu \right)^* \right] \tag{2.73}$$

in normalized units of $c_{\mathrm{ref}} n_{\mathrm{ref}} \rho_{\mathrm{ref}}^2 / L_{\mathrm{ref}}^2$ and $c_{\mathrm{ref}} n_{\mathrm{ref}} T_{\mathrm{ref}} \rho_{\mathrm{ref}}^2 / L_{\mathrm{ref}}^2$, respectively. Note that since in both fluxes, the combined potential χ appears, it is possible to split both expressions into three parts, corresponding to the transport caused by the electrostatic potential (the Φ component), as well as the perpendicular (the $A_\parallel$ component) and parallel (the $B_\parallel$ component) magnetic field fluctuations. The

first is then referred to as electrostatic transport, while the sum of the second two is called (electro-)magnetic transport.
Instead of the particle and heat flux, one may equivalently consider the particle and heat diffusivity, D_j and χ_j, respectively. Their relations to the fluxes are

$$D_j = \frac{\Gamma_j}{n_{j0}\omega_n} \quad , \quad \chi_j = \frac{Q_j}{n_{j0}T_{j0}\omega_{Tj}} \quad . \tag{2.74}$$

In the following, a brief discussion of the numerical implementation of the above Vlasov and field equations is given.

2.3.2 Time Stepping Schemes

To describe the time evolution of the distribution function, the time derivative in Eq. (2.65) is resolved either by one of three explicit schemes or one implicit time stepping scheme. The former are Runge-Kutta schemes; for third order and a Vlasov equation of the general form

$$\frac{\partial g(t)}{\partial t} = \mathcal{V}(g(t)) \quad , \tag{2.75}$$

the scheme can be written as

$$\begin{aligned} g(t+\Delta t) &= g(t) + \\ &+ \frac{\Delta t}{4}\left[\mathcal{V}(g(t)) + 3\mathcal{V}\left(g(t) + \frac{2\Delta t}{3}\mathcal{V}\left(g(t) + \frac{\Delta t}{3}\mathcal{V}(g(t))\right)\right)\right] \quad . \end{aligned} \tag{2.76}$$

Additionally, a fourth order and a modified fourth order Runge-Kutta scheme are available. Unlike implicit time stepping, their time step Δt is limited by their respective stability regions in the complex plane, along with the shape of the eigenvalue cloud of the simulation (one aspect of this stability constraint is discussed in Ch. 4). GENE allows for automatic adjustment of the time step, either continuously (for nonlinear simulations) or at the beginning of the simulation by calculation of the eigenvalue most critical for the stability (for linear simulations). The time evolution of linear simulations is characterized by exponential growth (or decay); thus, after the growth rate γ is converged, the simulation s stopped. In typical nonlinear cases, however, a saturated phase is reached eventually, and in order to optimize the statistics, a simulation may be continued at liberty. Not to be limited by machine restrictions on the simulation time, the distribution functions are written into a `checkpoint` file (for more on GENE output files, see Ch. 3) at the end of a run; the simulation may be resumed from that point by choosing these distributions as the initial condition for the next run. Apart from this, initial conditions for multiple scenarios are available; most prominently, all

physical modes may be initialized with identical amplitudes for linear simulations, and spectral power laws may be used to reach the saturation phase more quickly in nonlinear scenarios.

2.3.3 Coordinates and Parallelization

Since the perpendicular coordinates are represented in Fourier space, calculating derivatives is reduced to performing multiplications by the respective wavenumbers; however, since computation of the nonlinearity in Fourier space is very inefficient, the respective quantities (or, more precisely: their derivatives) are transformed into real space via inverse Fourier transforms, multiplied, and transformed back into Fourier space. This transformation is accompanied by Fourier-based interpolation (i.e., adding of zeroed modes) to reduce effects due to aliasing [29]. As a consequence of the above measures, nonlinear simulations are significantly more expensive than linear simulations with identical grid resolutions.
The parallel direction, however, has to be represented in real space due to its nonlocal character and its (generally) quasiperiodic boundary conditions. Since Eq. (2.65) involves parallel derivatives, stencil-based finite difference schemes have to be employed; details on the properties of those schemes and resulting problems can be found in Ch. 4.
For the parallel velocity coordinate, an equidistant grid is used, while the μ coordinate is defined on a grid based on Gauss-Legendre polynomials. Similarly to the parallel coordinate, the parallel velocity coordinate employs finite difference schemes for the derivative in the mirror term of the Vlasov equation.
The use of GENE on (massively) parallel computers is implemented both via MPI and via OpenMP directives, splitting the calculation for different grid points between multiple cores. The dimensions over which parallelization is possible are: species, y, z, $v_\parallel$, and μ. Since exchange of data between cores is the main problem where parallel computing efficiency is concerned, the species and μ parallelization are the primary choices, as they require very little communication. Between eight and 4000 cores were used to obtain the results presented in this thesis, and the code has been tested and shown to perform with excellent scaling on up to 32000 cores.

2.3.4 The Eigenvalue Solver

Alternatively to the initial value solver mentioned above, linear problems may be investigated by use of direct solution of the eigenvalue equation of the matrix that a numerical implementation of the Vlasov and field equations constitutes.

As part of the GENE code, an eigenvalue solver (see Kammerer [35] and Roman et al. [36]) is available that is based on the SLEPc library [37, 38]. However, instead of solving for a complete set of eigenvalues (which would be enormous in size and contain many physically irrelevant data points), only the most unstable eigenmodes are retrieved by use of test vectors. More details on the physics of subdominant and stable modes can be found in Ch. 5.

2.4 Chapter Summary

The gyrokinetic Vlasov equation was derived in this chapter by Lie transforming a one-form to gyrocenter coordinates, deriving the equations of motion from the Lagrangian, and subsequently inserting them into the Vlasov equation. Hereafter, an overview of the GENE code – which solves said equation – was given. The following chapter focusses on the visualization of results obtained with this code.

Chapter 3

Visualization of Simulation Results

With a gyrokinetic simulation operating on a time-dependent five dimensional distribution function, it becomes virtually impossible to display the entire information in a way that promotes understanding of the underlying physics. Thus, it is imperative that one condenses the available data and then chooses appropriate ways to visualize it. The condensation can be achieved most easily by either selecting only one point along one or more of the six available dimensions, or by averaging over one or more dimensions. The resulting reduced Fourier or real-space data can then be displayed either as a single numerical value, a line, contour, or surface plot. Additionally, when using real-space data, one can choose the coordinate system to either follow the local grid, or one can transform the simulation points into a toroidal system which gives an accurate picture of the physical locations of all points in the simulation grid.

In the following, detailed descriptions of two tools will be given that, together, produce a variety of analyses and visualizations of GENE output data.

3.1 The GENE Diagnostics Tool

Being part of the official GENE distribution, the GENE Diagnostics Tool is designed to provide easy access to post-processing of simulation data. Written in IDL language, it runs on a variety of systems and can also be used without an IDL license in its IDL Virtual Machine version.

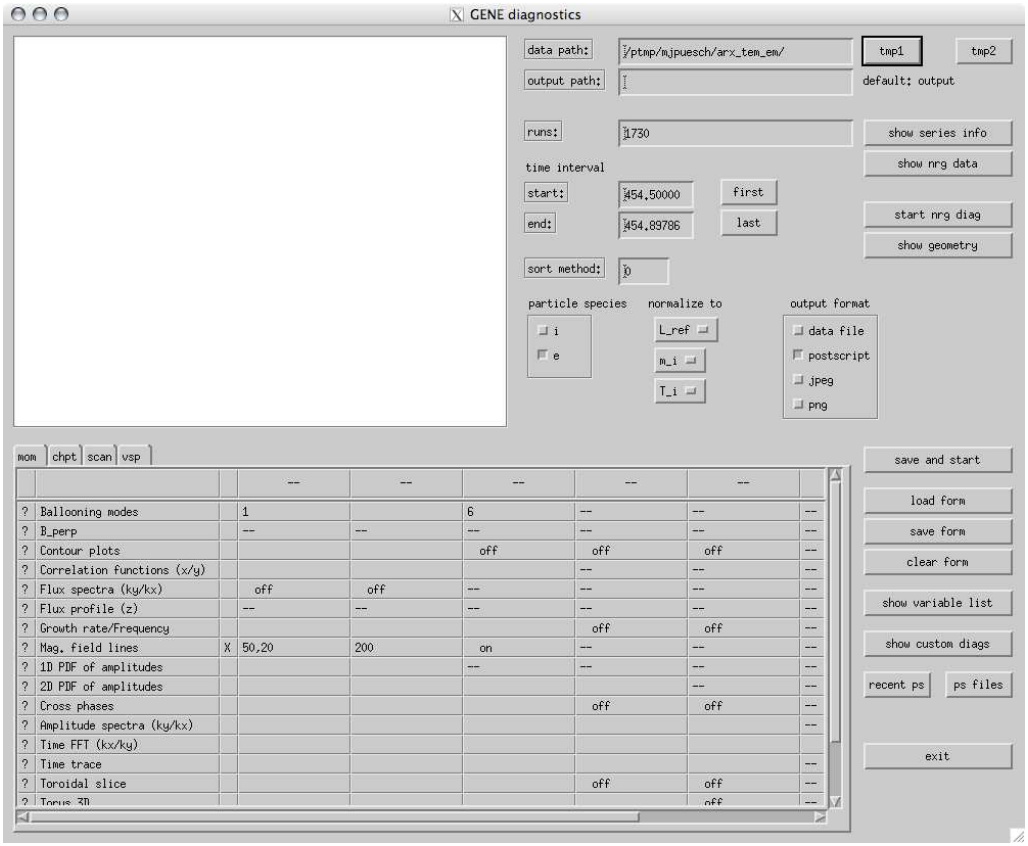

Figure 3.1: Graphical user interface of the GENE Diagnostic Tool. The white empty region to the upper left is used for interactive display of data; to the right from this area, general settings pertaining the runs to be analyzed can be adjusted, while some basic information about those runs may be requested. The table below contains the available diagnostics – diagnostic-specific parameters may be entered here. To the lower right, there are buttons to start the diagnostics loop, handle the state of the user interface, and open postscript output files.

3.1.1 Structure of the Diagnostics Tool

The graphical user interface (see Fig. 3.1) of the Diagnostics Tool enables the user to specify the following parameters: which simulations are to be analyzed in what time range; which species are to be considered; which normalization should be used; what format should the output be saved in; and which diagnostics are to be run with what diagnostics-specific settings. For convenience, functions are included such as displaying time traces of the `nrg` file or listing the most important simulation parameters.

When starting the analysis, the state of the graphical user interface is saved, and all settings are passed on to the diagnostics. The latter consist of four parts: info, init, loop, and output. The info section contains the name, description, and parameters specific to the corresponding diagnostic. In the init section, one may access those user-set parameters, define diagnostic-specific internal variables, and generally prepare the diagnostic for handling time-resolved data. This data, along with Fourier transforms, has to be requested in the init section so unnecessary load is avoided.

Hereafter comes the loop section which will be called as many times as time steps exist in the specified time range. Depending on the loop type – loops exist for handling GENE output in `field`, `mom`, and `checkpoint` files, as well as scan output produced by the GENE scan script – different normalized (and possibly Fourier transformed) data for every time step is passed on to the diagnostic which can then be manipulated and stored. For storing, one may use internal variables or one of two pre-defined functions, `time_avg` and `store_step`. The former performs time averaging with effects due to adaptive GENE time steps included, while the latter simply stores a variable for every time step in pointer lists so that all time steps may be made use of separately in the output section.

After looping over all time steps in the time range, the output section is called, where data may be processed additionally (e.g., renormalization to previously unknown global extrema) and then plotted. Here, the IDL output device is selected by calling the `set_output` procedure to allow for postscript, image, or data file output. Rudimentary movie encoding is available in IDL, but writing image files and then encoding separately is recommended for higher image quality.

Unless the IDL Virtual Machine is used, one can add diagnostics to the Diagnostics Tool by placing a file containing the required procedures in either the `prog` or the `custom` subdirectory. The latter will cause recompilation of the procedures upon starting the analysis, while to achieve this for the former, one has to restart the Diagnostics Tool.

A range of diagnostics are part of the official GENE distribution. Those, along with some additional diagnostics, are presented below.

3.1.2 Built-in Diagnostics

In the following, the term *variable* refers to a field in the `field` or `mom` file.

Time Traces

A very intuitive way of looking at simulation data is to simply select a mode in the perpendicular plane by specifying a pair of k_x and k_y, either at a single parallel point or averaged over the parallel direction, and then look at the time evolution of a variable at that grid point. This functionality is provided by the `timetrace` diagnostic which plots this data and additionally allows for smoothing the output curves.

Amplitude Spectra and Parallel Profiles

The `spectra` diagnostic plots k_x and k_y spectra of the amplitudes of the selected variable logarithmically; by default, the data for the spectra is averaged over the respective other perpendicular coordinate, but selecting single modes is possible, as well. Since the slopes with which the spectra fall off for higher k are of relevance for the physics involved, power laws are fit to the data if the user specifies the relevant k ranges.
This leaves the parallel coordinate, the amplitudes for which can be viewed for the standard $-\pi \ldots \pi$ range using the `zprofile` diagnostic. Like with the spectra, the perpendicular directions can be treated by either averaging or selecting single modes. A modified version that plots parallel pseudospectra – which is especially useful for diagnosing slab simulations – also exists.
Additionally, modified versions exist for both diagnostics that include the respective plots of the vorticity for cases with adiabatic electrons.

Flux Spectra and Parallel Profiles

For viewing spectra and parallel structures of nonlinear fluxes, separate diagnostics are required, `fluxspectra` and `fluxzprofiles`, respectively. Here, no variables have to be specified; heat and particle fluxes – if available, both the electrostatic and the electromagnetic component – are plotted. In the case of the `fluxspectra` diagnostic, plots of the fluxes multiplied by $k_{x,y}$ may be added; a

modified version that can analyze linear simulations exists, as well, in case one aims to conduct quasilinear investigations.

Ballooning Representation

The ballooning representation is a useful choice to view mode structures that extend beyond the standard 2π parallel range. Modes usually center on the $k_x = 0$ mode, and get shifted to higher k_x values as they reach the parallel end of the box. Making use of the parallel boundary condition, the full mode can be reconstructed, which is done by the `ball` diagnostic. One may select a variable and a k_y for plotting. Additionally, a zoom range can be specified if one is interested in the fine structure of strongly extended modes.

Contour Plots

Plotting contours of the perpendicular plane, be it in Fourier, mixed, or real space, is done via the `cont` diagnostic. After choosing a single point along the parallel coordinate, it plots contours of selected variables. An IDL direct movie function is implemented; however, for high quality movies, use of a slightly modified diagnostic is encouraged.

Toroidal Geometry: Constant ϕ Surfaces

The `torslice` diagnostic takes $\hat{s}$-α flux tube data for a selected variable, transforms that data into toroidal geometry, and plots contours of a constant ϕ slice. This works similarly to the procedure used to create GENE data sets for the RZG VisualKit (which is described below), with linear interpolation along the y coordinate. Direct movie output as well as high quality image output is available.

Correlation Functions

To compute real space correlation functions in the x-y plane, one may use the `corr` diagnostic. It accepts two variables and calculates their correlation at a single parallel point. To study correlations between variables of different particle species, one has to use a separate, modified diagnostic.

Probability Distribution Functions

The `pdf1d` and `pdf2d` diagnostics count the occurrence of function values of specified variables among all real space points on the simulation grid. The former

does so for a single variable, the second counts using a two-dimensional bin array; consequently, 1-D or 2-D histograms are plotted, respectively.

Growth Rates and Frequencies

Linear growth rate and frequency analysis is one of the standard instruments in numerical plasma physics; the `gamom` diagnostic can handle both linear and nonlinear simulations. Separated into k_y modes, it takes the electrostatic potential – averaged or for selected k_x modes, and similarly: averaged or for a selected parallel point – and computes complex frequencies based on the time dependence of the complex phase. These frequencies may be weighted with the amplitude of the electrostatic potential at that point; for typical extended mode structures, this tends to reduce the influence of high-k_x modes.
While generally, this works for nonlinear frequencies, as well, a second diagnostic, `timefft`, is also available for that case. It takes data for a specified variable at specified coordinates and Fourier transforms the time coordinate of that data; the raw signal, as well as spline-interpolated and windowed data is plotted. Note that it can be useful to run both diagnostics presented here if one aims to study nonlinear frequencies, since both versions have advantages and drawbacks; e.g., the former, while providing fast and unambiguous spectra, may give polluted results as soon as a second mode starts to compete with the dominant mode; the latter may resolve multiple (sub-)dominant frequencies simultaneously, but one can encounter statistical issues, and operation is more difficult due to the required settings for the windowed Fourier transform.

Phase Relations

The `phases` diagnostic computes phase relations by evaluating complex phases of (multiple) pairs of variables, with the possibility of averaging over x and z direction. The result is shown as a contour plot that includes the k_y dependence – this makes it a useful tool for investigating linear effects in nonlinear simulations. Amplitude weighting along the k_y direction is available to single out dominant contributions. For this diagnostic, a modified version exists that allows separation of composed `mom` variables (e.g., separation of $q_\parallel + 1.5 p_{j0} u_\parallel$ into $q_\parallel$ and $u_\parallel$).

Zonal Flows and Zonal Fields

Zonal flows and zonal fields can influence the properties of plasma microturbulence significantly. In order to estimate their quantitative impact, one may use the `zonal` diagnostic which computes the shearing rate due to zonal flow activity,

as well as the shear fluctuations due to magnetic perturbations. This is done for all nonzero or only selected k_x modes. Similarly to the `timefft` diagnostic, a windowed Fourier transform of the zonal potential is possible. Additionally, a correction functionality is available if a decorrelation time is specified. See Ch. 5 for more details on zonal flows and finite frequency corrections.

Velocity Space Diagnostic

For the analysis of the velocity space data from the `vsp` file, the `vsp1` diagnostic should be employed. It plots the time-resolved heat or particle fluxes, or the distribution function, for specified parallel points, averaged over the perpendicular spatial coordinates.

3.1.3 Additional Diagnostics

Perpendicular Magnetic Field Fluctuations

The `bperp` diagnostic plots time traces of the spatial root mean square of the radial and toroidal magnetic field fluctuations, B_x and B_y, respectively. It requires nonlinear electromagnetic simulations.

Magnetic Field Lines

Integrative field line reconstruction based on perpendicular magnetic field fluctuations is done by the `magfline` diagnostic. Since it was used to produce the Poincaré sections presented in Ch. 7, it is explained in more detail here than the other diagnostics.
First, the perpendicular magnetic field fluctuations, B_x and B_y, are calculated in Fourier space, and then transformed into real space at high resolution; possibly missing Fourier modes are set to zero. This way, a smooth field can be guaranteed. Additionally, B_x and B_y are interpolated in the parallel direction by a very large factor, with the standard resulting N_z being 3000. Into this field, a set of field lines (whose size can be specified freely) is inserted with initial positions at a toroidal angle $\phi = 0$ and with equidistant spread in both the radial and the poloidal coordinate.
Then, those field lines are successively integrated, proceeding one (interpolated) Δz at a time while using the following prescription: the perpendicular shift per parallel step is calculated at the current z position; from there, the field line position at $z + \Delta z/2$ is calculated, and the shift extracted there; this new shift is then applied at the original z position, this time proceeding to the next point at

$z + \Delta z$. This method helps avoid curvature-caused errors which otherwise may add up quickly [39].
Every time a field line passes the $\phi = 0$ plane, its position is stored; after a specified number of toroidal cycles, the integration loop exits. The thus obtained Poincaré data is then plotted both point-wise and as a histogram which allows for distinguishing locations where multiple field line passings have occurred.
In addition, the perpendicular field fluctuations at the outboard midplane (i.e., the central parallel point) can be plotted as contours in the perpendicular plane. Besides those fluctuations being of possible interest by themselves, this allows the user to make sure that the magnetic structure is physical, sufficiently resolved, and smooth enough with the current resolutions specified for the Fourier transforms.
Benchmarking of the results of this diagnostic against the GOURDON code [40] is planned for the future.

Magnetic Transport Model

A model for the magnetic transport which will be explained in detail in Ch. 7 can be applied with the `chi_e_em` diagnostic. It uses the $A_\parallel$ field data to predict the (time-resolved) electron magnetic heat transport and then multiplies it by a scalar factor in order for its temporal average to match that of the actual heat flux (as given by the `nrg` data). Together with the thus obtained curve, the `nrg` heat flux may be plotted for direct comparison.

Toroidal Representation

The `torus3d` diagnostic produces output much like that of the RZG VisualKit GENE data set production tool described below: local $\hat{s}$-α flux tube data is transformed into toroidal geometry, with the original flux tube being duplicated to fill the entire flux tube. Two output variants are available: either the data can be used as textures for a 3-D torus model, yielding surface contours of a $\phi_0 \ldots \phi_1$ angular section of the torus including the cut surfaces; or the data can be plotted into four separate image files: two constant ϕ cut surfaces, and the inner and outermost flux surfaces. This second functionality is intended to be used with the external rendering tool POV-RAY [41, 42] which allows for more advanced visualization than IDL.
It is to be noted that the `torus3d` diagnostic is designed for high quality image output to allow for subsequent movie encoding.

Velocity Space Diffusivity

Another diagnostic to operate on velocity space data is `vsp2`. Here, either for a single μ value or the entire range, the particle diffusivity is calculated, allowing for zooming in on the high-T tails of the Maxwellian. An application of this diagnostic is shown in Ch. 7.

3.2 The RZG VisualKit

Interactive display of non-interpolated flux tube data is still possible using IDL technology; however, to get a visually meaningful result, one has to compensate for the large ratio of the parallel to the perpendicular length scale with significant interpolation of the parallel coordinate (one to two orders of magnitude; see below). Additionally, it can be useful to make use of the toroidal boundary condition to expand the data to a hollow torus, increasing the amount of data to be displayed by another order of magnitude. As shown above, the GENE Diagnostics Tool can still cope with this data, but interactive manipulation is no longer possible. If one requires such interactivity, use can be made of the RZG VisualKit instead which will be presented here.

3.2.1 Technology

The RZG VisualKit was developed by Ralph Bruckschen and José Mejia to be used with GENE data sets, while employing visualization techniques similar to those described in Refs. [43] and [44]. As it is Java-based – using the Java OpenGL 2.0 wrapper library [45] for OpenGL [46], it can be run on almost all operating systems; however, there is a hardware limitation that will be discussed further down.

The tool is able to read the position of any number of data points in Cartesian coordinates, along with (time dependent) data values for each point, as long as the graphics adapter has sufficient memory available. It provides a graphical user interface which can be used to rotate or translate the point cloud, allows for zooming, adjusting of the point size and brightness, and lets the user select data sets and color tables. Additionally, clipping planes can be activated and manipulated to get more specific visual access; time steps can be displayed continuously, which, along with the integrated screen shot function, allows for simple creation of encoding-ready image sequences. Moreover, using specifically prepared color tables, one can use the RZG VisualKit to investigate isosurfaces.

As input data, it accepts point clouds on a short integer normalized Cartesian

grid, along with values corresponding to those points which are also normalized to the short integer range to optimize memory throughput and save disk space – this theoretically limits both the spatial and the color resolution, but not enough to have any significant impact on typical visualizations of GENE data, even at maximum zoom rate. The data is then, one time step at a time, copied to the memory of the graphics adapter. This puts a constraint on the RZG VisualKit in that it requires access to computers with modern graphics adapters (more specifically, Shader Model 3 or higher is required). For fully toroidal data sets, at least 256MB of dedicated GPU memory are recommended.

The graphics adapter renders the 3-D point cloud via direct point splatting. For every point, its data set value is retrieved via a 3-D texture lookup of its relative position within the data set. This value is then transformed into an RGB color value via a 1-D color table lookup. These lookups are implemented in a combined fashion as a fragment shader on the GPU. The points are rendered as anti-aliased flat round disks with a normal vector parallel to the line of sight.

If correctly sorted, use can be made of an additional feature. The RZG VisualKit is able to connect the points corresponding to a flux surface, – i.e., points with constant local x coordinate – by covering the surface with quad strips. Locally neighboring points are connected so that physical structures are highlighted. However, those quads are opaque, and while two such surfaces may be used simultaneously, the inner one will be visible only if one uses the feature in conjunction with clipping planes.

3.2.2 GENE Data Sets

Routines for creating RZG VisualKit data sets from GENE output data exist for both $\hat{s}$-α geometry (so far, effects due to finite α are neglected) and general geometry (via the Tracer output file). Since all three-dimensional GENE output is provided in local (x, y, z) coordinates, one has to transform this data into global Cartesian (X, Y, Z) coordinates. If GENE is run in $\hat{s}$-α flux tube geometry, use of the following transformations can be made:

$$r = r_0 + \left(x - \frac{N_x}{2}\Delta x\right) \tag{3.1}$$

$$\theta = \frac{2\pi}{N_z} z - \pi \tag{3.2}$$

$$\phi = -\frac{q_0}{r_0}\left(y - \frac{N_y}{2}\Delta y\right) + q_0\left[1 + \frac{\hat{s}}{r_0}\left(x - \frac{N_x}{2}\Delta x\right)\right]\theta \tag{3.3}$$

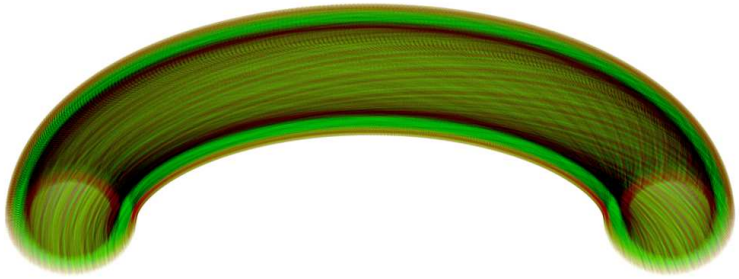

Figure 3.2: Tokamak flux tubes spanning a hollow torus; GENE data for the parameter set described in Ch. 6 is visualized using the RZG VisualKit. $\mathcal{M} = 10$ identical flux tubes are shown here. With the parallel coordinate interpolated from 48 to 800 points, a total of 73.7 million points are included in the data set, half of which are shown here after clipping ϕ values from π to 2π for illustrative purposes.

This set of torus coordinates can easily be further transformed to a global Cartesian grid:

$$X = r\cos\phi\cos\theta \tag{3.4}$$

$$Y = r\sin\phi\cos\theta \tag{3.5}$$

$$Z = r\sin\theta \tag{3.6}$$

These rules are applied to every single data point; considering the different length scales in gyrokinetic flux tubes, namely a parallel direction much more elongated when compared to its perpendicular counterparts, it is necessary to interpolate said parallel direction. To allow for a more regular (X, Y, Z) structure, the point density in all original coordinate directions has to be of the same order. Consequently, interpolations of the parallel direction by factors of ~ 50 are typical, depending on the choices for the major radius R_0 and the gyroradius ρ_s. Exemplary $\hat{s}$-α visualizations are shown in Figs. 3.2 and 3.3 for point splatting and quad surfaces, respectively. Here, $\mathcal{M} = 10$ flux tubes were used to fill the flux surfaces.

Mapping dimensionless local coordinates onto a real-space Cartesian grid requires settings for the normalization lengths; in the new reference frame, two free scaling parameters remain, one of which is chosen to be the major radius R_0 of the magnetic axis. Fixing R_0 simultaneously sets the parallel length scale since the parallel coordinate is defined as $z = 2\pi\hat{z}q_0R_0/N_z$ (here, $\hat{z}$ denotes the nondimensional value). As a result, without loss of generality – at least as far as the

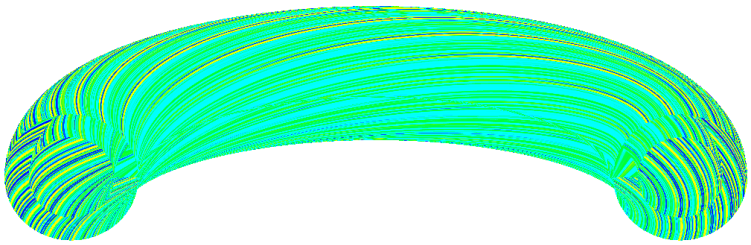

Figure 3.3: Shown here is the same data set as in Fig. 3.2; while before, all points were splatted, now only the outermost and innermost flux surfaces are visualized by connecting points with quad strips. From this figure, it becomes apparent that the turbulence amplitudes are highest on the outside of the torus where the magnetic field is weakest.

visualization is concerned – the major radius can be set to $R_0 = 1$.
For the perpendicular coordinates, the scaling length is the gyro radius. Any choice of ρ_s (in units of R_0) needs to be consistent with the boundary conditions, however, at least if one aims to cover the entire (hollow) torus with $\mathcal{M}$ multiple identical flux tubes. Parallel structures need to be closed after a full poloidal turn. Thus, the position of the field line at $\theta = 2\pi$ needs to coincide toroidally either with itself or with one of its L_ϕ-shifted copies, as is illustrated in Fig. 3.4. Given that $\mathcal{M}L_\phi = 2\pi$, and that the field line has to end at the toroidal position

$$\phi = \bar{\mathcal{M}} L_\phi \quad , \qquad \bar{\mathcal{M}} \in \{0, \ldots, \mathcal{M} - 1\} \quad , \tag{3.7}$$

one finds the boundary condition to be

$$\begin{aligned} (2\pi q_0) \bmod (2\pi) &= \bar{\mathcal{M}} L_\phi & (3.8) \\ \Leftrightarrow (\mathcal{M} q_0) \bmod 1 &= 0 \quad . & (3.9) \end{aligned}$$

Even for rational values of q_0, this can require extremely large values of $\mathcal{M}$, resulting not only in more data being produced, but also in structures being too small to provide a meaningful visualization. Therefore, it is sometimes useful to slightly alter the original value of q_0, for instance by allowing only one digit after the decimal point.
With a choice of $\mathcal{M}$ being made, one may use the torus covering condition $\mathcal{M}L_\phi = 2\pi$ to arrive at the required gyroradius:

$$\rho_s = \frac{2\pi r_0}{\mathcal{M} q_0 \hat{L}_y} \quad , \tag{3.10}$$

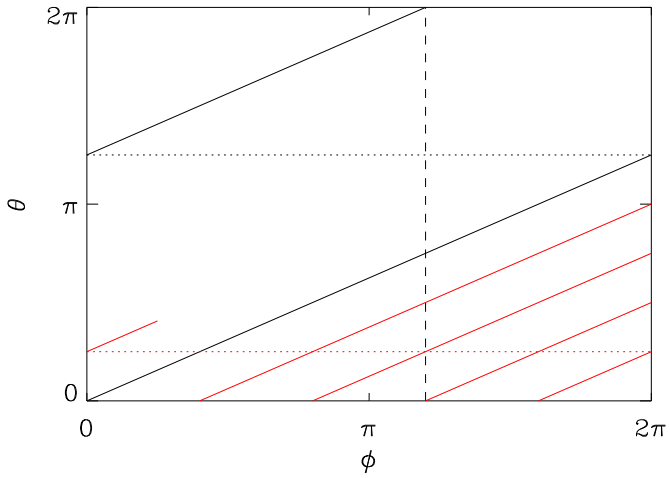

Figure 3.4: Field lines on a fully covered flux surface. In the absence of magnetic fluctuations, field lines are represented by lines with slope $q(r)^{-1}$ in the ϕ-θ plane. Here, an example is given with $q = 1.6$, where the surface is covered by $\mathcal{M} = 5$ flux tubes; the first field line of the original flux tube is shown as a bold black line, those of the copies as red lines. As the primary field line reaches $\theta = 2\pi$, its toroidal position matches that of the third copy ($\bar{\mathcal{M}} = 3$), thus complying with the condition imposed by Eq. (3.8).

with $\hat{L}_y$ denoting the box size in the y direction in units of the gyroradius.
Alternatively, general geometry data sets can be created. In general, such geometry does not allow for periodic use of the flux tube; thus, only one flux tube is visualized, leaving the user with a free choice of both R_0 and ρ_s. Apart from that, the procedure is similar to its $\hat{s}$-α counterpart, with a new set of coordinate transformations:

$$X = \left[\bar{r}(\phi) + \left(x - \frac{N_x}{2}\Delta x\right)\mathcal{P}(\nabla x, \nabla\bar{r}(\phi))\right]\cos\phi \tag{3.11}$$

$$Y = \left[\bar{r}(\phi) + \left(x - \frac{N_x}{2}\Delta x\right)\mathcal{P}(\nabla x, \nabla\bar{r}(\phi))\right]\sin\phi \tag{3.12}$$

$$Z = \left[\bar{z}(\phi) + \left(x - \frac{N_x}{2}\Delta x\right)\mathcal{P}(\nabla x, \nabla\bar{z}(\phi))\right] \tag{3.13}$$

which are completed by the previous definition of ϕ (see Eq. (3.3)). Here, $\mathcal{P}(i, j)$ represents a projection of i on j, and the quantities $\bar{r}(\phi)$ and $\bar{z}(\phi)$ are given by the TRACER code, just like the employed projections.

Figure 3.5: RZG VisualKit visualization of a Wendelstein 7-X flux tube. The physical data was calculated by P. Xanthopoulos using the GENE code, with the geometry stemming from the TRACER code. In the case depicted here, the flux tube seems to loop onto itself after one toroidal cycle, but this effect is purely coincidental.

An example for RZG VisualKit output based on a GENE data set in stellarator geometry – more specifically, Wendelstein 7-X geometry – is given in Fig. 3.5. Here, only one flux tube is shown which happens to nearly close in itself after one toroidal turn. Generally, one can only achieve closure in general geometry if one has data for all flux tubes that span a flux surface.

3.2.3 Limitations and Further Requirements

While being a powerful instrument which can handle large amounts of data, the RZG VisualKit is suffering from some limitations. It is to be noted that high resolution GENE data sets can have very large file sizes ($\sim$ 100 MB per time step) and require high-end graphics hardware for interactive manipulation. Considering that this constraint comes practically solely from the excessive parallel interpolation, it would be useful to adjust interpolation in the RZG VisualKit itself, depending on the zoom factor and the area being displayed. At the same time, handling the data in local coordinates internally in the RZG VisualKit

would lift some load off the data set preparation process which can take multiple hours. In addition, one would be able to select points on a local (i.e., physical) basis rather than via clipping planes. And lastly, this way not only flux surfaces could be spanned by quads, but any shapes, being it slices of constant ϕ, single flux tubes, or isosurfaces.

3.3 Chapter Summary

In this chapter, tools of simulation data analysis were presented which allow for versatile visualization of GENE simulation output. The GENE Diagnostics Tool – which was redesigned and extended in the context of this thesis – bundles a wide range of diagnostic programs and provides a graphical user interface for convenient use; it can be augmented by adding arbitrary numbers of new programs. Official and additional such programs are described, some of which were fundamental for the investigations performed in this thesis. Additionally, the RZG VisualKit was introduced which relies on dedicated graphics hardware to handle vastly larger amounts of data interactively than would be possible within the IDL framework. Advantages and limitations are discussed, and examples of visualizations are given for both $\hat{s}$-α and general (here: stellarator) geometry, making use of an IDL-based program which creates GENE data sets for the RZG VisualKit.

Chapter 4

Numerical Diffusion in GENE

In this chapter, the versatile uses of (hyper-)diffusion terms in the Vlasov equation are discussed, presenting ways to minimize unphysical effects due to the occurrence of numerical modes. An emphasis is put on numerical dissipation in the parallel dynamics; parallel velocity space and radial diffusion are investigated, as well. The chapter mainly follows Pueschel et al. [47].

4.1 Finite Difference Schemes

While in Fourier space, derivatives are calculated through multiplication by powers of the corresponding wave number, k, real space numerical derivatives require knowledge of function values at neighboring points on the discretization grid. For instance, the simplest way of calculating a first derivative of a function $f(x)$ which is discretized on a grid with spacing Δx using this principle is

$$\left[\frac{\partial f}{\partial x}\right](x) = \frac{f(x) - f(x - \Delta x)}{\Delta x} \quad . \tag{4.1}$$

In the shorthand notation used in this chapter, this scheme reads

$$[\,-1 \quad 1 \quad 0\,] \quad . \tag{4.2}$$

By definition, the center value is the coefficient for the function value at x, to the left are the coefficients for function values at positions $< x$, and to the right those for function values at positions $> x$.

4.1.1 Centered and Upwind First Derivatives

Centered stencils are defined as those with entries antisymmetric about the center (i.e., $a_i = -a_{-i}$, $a_0 = 0$), while upwind schemes are asymmetric, with the

$\mathcal{O}$	type	stencil
1	u	ξ^{-1} $[-1 \quad 1 \quad 0]$
2	c	$(2\xi)^{-1}$ $[-1 \quad 0 \quad 1]$
3	u	$(6\xi)^{-1}$ $[1 \quad -6 \quad 3 \quad 2 \quad 0]$
4	c	$(12\xi)^{-1}$ $[1 \quad -8 \quad 0 \quad 8 \quad -1]$
5	u	$(60\xi)^{-1}$ $[-2 \quad 15 \quad -60 \quad 20 \quad 30 \quad -3 \quad 0]$
6	c	$(60\xi)^{-1}$ $[-1 \quad 9 \quad -45 \quad 0 \quad 45 \quad -9 \quad 1]$
7	u	$(420\xi)^{-1}$ $[3 \quad -28 \quad 126 \quad -420 \quad 105 \quad 252 \quad -42 \quad 4 \quad 0]$
8	c	$(840\xi)^{-1}$ $[3 \quad -32 \quad 168 \quad -672 \quad 0 \quad 672 \quad -168 \quad 32 \quad -3]$

Table 4.1: First derivative stencils; the first column specifies the stencil order, the second column the type, with u and c denoting upwind and centered schemes, respectively. The centered stencils shown here have maximal order for their size, while the upwind stencils have order one less than the centered stencils of the same width.

last stencil coefficient being zero. Unlike centered stencils, upwind stencils are diffusive in nature, a property described in more detail later. It shall be noted at this point, however, that in order to exploit the stabilizing nature of upwind stencils, one has to take into account the total sign of the derivative term: in case it changes (which may happen, e.g., when the parallel velocity sign changes in the parallel term of Eq. 2.65), the upwind stecil has to be inverted to avoid destabilization of the simulation.
A prescription of how to construct a centered first derivative stencil is detailed below. Starting with the Taylor expansion of a function $f(x)$, one may calculate its values at the neighboring points on a grid of spacing ξ. On thus obtains

$$\begin{aligned}
f(x \pm \xi) &= f(x) \pm \xi \tfrac{f'(x)}{1!} + \xi^2 \tfrac{f''(x)}{2!} \pm \ldots &&= \sum_{k=0}^{\infty} \xi^k \tfrac{f^{(k)}(x)}{k!} \\
f(x \pm 2\xi) &= f(x) \pm 2\xi \tfrac{f'(x)}{1!} + 4\xi^2 \tfrac{f''(x)}{2!} \pm \ldots &&= \sum_{k=0}^{\infty} (2\xi)^k \tfrac{f^{(k)}(x)}{k!} \\
&\vdots &&\vdots \\
f(x \pm l\xi) &= f(x) \pm l\xi \tfrac{f'(x)}{1!} + l^2\xi^2 \tfrac{f''(x)}{2!} \pm \ldots &&= \sum_{k=0}^{\infty} (l\xi)^k \tfrac{f^{(k)}(x)}{k!}
\end{aligned} \tag{4.3}$$

with $l \in \mathbf{N}$ and $f^{(n)}(x) \equiv \partial_x^n f(x)$. These terms can now be combined to an arbitrary stencil – which, in general, has neither a physical meaning nor an effect that is numerically desirable – of width l with coefficients a_i:

$$a_{-l} f(x - l\xi) + \ldots + a_{-1} f(x - \xi) + a_0 f(x) +$$

$$+ a_1 f(x+\xi) + \ldots + a_l f(x+l\xi) \mathrel{\hat{=}} \tag{4.4}$$
$$\mathrel{\hat{=}} \begin{bmatrix} a_{-l} & \ldots & a_{-1} & a_0 & a_1 & \ldots & a_l \end{bmatrix} \quad .$$

To give meaning to this stencil while imposing conditions on its entries, it may be equated to the first derivative of $f(x)$. Hence, one arrives at a linear system of equations with the variables a_i, $i = -l \ldots l$. This system is homogeneous save for the entry resulting from the term $\partial_x f(x)$:

$$\left(\begin{array}{ccccccccc|c} a_{-l} & & a_{-2} & a_{-1} & a_0 & a_1 & a_2 & & a_l & \xi^{-1} \\ \hline 1 & \cdots & 1 & 1 & 1 & 1 & 1 & \cdots & 1 & 0 \\ -l & & -2 & -1 & 0 & 1 & 2 & & l & 1 \\ l^2 & & 4 & 1 & 0 & 1 & 4 & & l^2 & 0 \\ -l^3 & & -8 & -1 & 0 & 1 & 8 & & l^3 & 0 \\ \vdots & & & & \vdots & & & & \vdots & \vdots \\ (-l)^n & \cdots & (-2)^n & (-1)^n & 0 & 1 & 2^n & \cdots & l^n & 0 \end{array}\right) \tag{4.5}$$

Here, the j-th line corresponds to the equation for the j-th derivative, $\partial_x^j f(x)$, $j = 0 \ldots n$. In the column marked ξ^{-1}, the right hand side inhomogeneity due to the original derivative term is found (which the stencil is equated to), while the other columns contain the left hand side coefficients a_i of the stencil entries.

Generally, there is some freedom as to how to choose the dimension parameters of this system, l and n. However, it is intuitive to comply with the rule $2l+1 = n+1$ in order not to have an under- or overdetermined system. n determines the order of the stencil; e.g., for a first derivative, considering $n+1$ equations leads to an n-th order stencil. A centered stencil of maximal order thus always has even order. Alternatively, one may impose conditions on the entries, with each condition – generally – reducing the order by one. To calculate upwind stencils, a_l must be set to zero. Results obtained using the above prescriptions can be found in Tab. 4.1. If one aims to construct stencils with additional properties (e.g., certain symmetries), one may substitute the corresponding conditions for an equal number of lines in the above system, starting with the last and working one's way up.

Note that with increasing order, the minimal stencil width grows, making a computation more precise yet more expensive at the same time: large stencils make parallel computations rather inefficient due to the increased communication between cores, while very small stencils require larger grid resolutions; in practice, a good compromise is usually achieved with stencils comprised of 5 or 7 entries, corresponding to 4-th or 6-th order centered first derivatives, respectively.

n	stencil
2	$\xi^{-2} \quad [1 \; -2 \quad 1]$
4	$\xi^{-4} \quad [1 \; -4 \quad 6 \; -4 \quad 1]$
6	$\xi^{-6} \quad [1 \; -6 \quad 15 \; -20 \quad 15 \; -6 \quad 1]$
8	$\xi^{-8} \quad [1 \; -8 \quad 28 \; -56 \quad 70 \; -56 \quad 28 \; -8 \quad 1]$

Table 4.2: Higher derivatives as required for (hyper-)diffusion terms; the derivative ∂_x^n is specified in the first column. All stencils shown here are of second order.

4.1.2 Higher Derivatives

Going to higher derivatives, one must simply place the inhomogeneity in Eq. (4.5) in another line; for the n-th derivative, it has to be in the $(n+1)$-th line, with an adjusted exponent of $\xi - n$. For diffusion and hyperdiffusion terms – which are investigated in this work – derivatives ∂_x^n with even n are required. Stencils for some common choices of n are found in Tab. 4.2.
Henceforth, hyperdiffusion ($n \geq 4$) and diffusion ($n = 2$) are both referred to as simply diffusion. While generally, this term may also be used for physical processes in fusion plasmas (see, e.g., Ch. 7), here it means inclusion of a numerically dissipative term in the Vlasov equation that involves an n-th derivative of the (possibly modified) distribution function.

4.2 Parallel Dissipation

4.2.1 A Simplified Model

The Adiabatic Slab Case

In order to gain a deeper understanding of the dynamics parallel to the magnetic field lines, a simplified model is used; it is derived from the full gyrokinetic framework (see Eqs. (2.65) and (2.66) to (2.68)), making the following assumptions:

- the magnetic field is homogeneous and static,
- the (singly charged) ions may be treated in a drift-kinetic fashion,
- the electrons behave adiabatically, and
- the nonlinearity is dropped.

The first of these assumptions implies that $B_0 = 1$, $\mathcal{K}_x = \mathcal{K}_y = 0$, $\epsilon_t = 0$, and $\beta = 0$. Additionally, in the drift-kinetic limit – corresponding to the long-wavelength regime – $b_i, \lambda_i \ll 1$, which leads to $J_0(\lambda_i) \approx 1$ and $\Gamma_0(b_i) \approx 1$. Note that unlike in the general case, the parallel direction is now periodic, allowing for Fourier representation of the parallel coordinate. The velocity space coordinate μ may be integrated out (as shown by Jenko and Scott [48]), and one is left with two coupled equations,

$$\frac{\partial F_1}{\partial t} + \left[\omega_n + \omega_{T\mathrm{i}}\left(v_\parallel^2 - \frac{1}{2}\right)\right] ik_y \Phi F_0 + \alpha_\mathrm{i} v_\parallel \frac{\partial F_1}{\partial z} + \tau_\mathrm{e}\alpha_\mathrm{i} v_\parallel \frac{\partial \Phi}{\partial z} F_0 = 0 \qquad (4.6)$$

and

$$\Phi = \int F_1 \mathrm{d}v_\parallel \quad , \qquad (4.7)$$

for the complex quantities $F_1(z, v_\parallel, t)$ and $\Phi(z, t)$. Here, the distribution functions' species subscript i was dropped, and the parameter $\tau_\mathrm{e} = T_{\mathrm{e}0}/T_{\mathrm{i}0}$ was introduced. The equilibrium distribution function becomes

$$F_0(v_\parallel) = \frac{1}{\sqrt{\pi}} \mathrm{e}^{-v_\parallel^2} \quad . \qquad (4.8)$$

The binormal y direction is represented in Fourier space, and the radial x direction is averaged over (corresponding to $k_x = 0$). For Eqs. (4.6) and (4.7), the dispersion relation can be written as

$$1 + \tau_\mathrm{e} + (\tau_\mathrm{e}\varpi + \varpi_{n\mathrm{i}}) Z(\varpi) + \varpi_{T\mathrm{i}} Y(\varpi) = 0 \quad , \qquad (4.9)$$

with the plasma dispersion function $Z(x)$ [49] and the derived function $Y(x) = x + (x^2 - 1/2)Z(x)$. The other quantities are $\varpi \equiv \omega/(\alpha_\mathrm{i} k_\parallel)$, $\varpi_{n\mathrm{i}} \equiv \omega_{n\mathrm{i}} k_y/(\alpha_\mathrm{i} k_\parallel)$, and $\varpi_{T\mathrm{i}} \equiv \omega_{T\mathrm{i}} k_y/(\alpha_\mathrm{i} k_\parallel)$. For certain parameters, this dispersion relation has one solution with a positive imaginary part, corresponding to a slab ITG mode. Eq. (4.9) can be evaluated numerically in a straightforward fashion, allowing for comparisons with direct numerical solutions of Eqs. (4.6) and (4.7). This is useful when investigating the role of numerical dissipation in the parallel dynamics, as is done below.

Numerical Approach

For the numerical solution of Eqs. (4.6) and (4.7), a simple $(1 + 1)$-dimensional Vlasov code was used, which amounts to a reduced version of the GENE code. The spatial parallel z coordinate is defined on the range $-\pi \ldots \pi$, while the parallel velocity coordinate ranges from $v_\parallel = -4$ to 4 in the same normalized units that are described in Ch. 2. Real space and velocity space are discretized by employing

N_z and N_v equally spaced grid points, respectively. In slab geometry, the spatial boundary conditions are taken to be periodic, and for the integration procedure in velocity space, a simple trapezoidal rule is used. A standard third-order explicit Runge-Kutta scheme is employed for the time stepping. Unless stated otherwise, the physical and numerical parameters are chosen as follows: $\tau_\mathrm{e} = \omega_n = 1$, $\omega_{T\mathrm{Ti}} = 10$, $\alpha_\mathrm{i} = 0.34$, and $k_y = 0.3$ – this corresponds to rather typical parameters of gyrokinetic simulations, where growth rates tend to peak around this value of k_y. For the basic scenario, the phase space grid is characterized by $N_z = 16$ and $N_v = 32$, and the time step is always chosen to be well below the Courant limit. Usually, the total run time is about $100 c_s/L_\mathrm{ref}$, with the initial transients typically dying off after only a few time units. In order to compute a linear growth rate, the spatial average of the absolute of the (complex) electric potential perturbation is evaluated. Then, a straight line is fitted to the logarithmic plot of that average, excluding effects from the initial transient time range.

4.2.2 Occurrence of High-$k_\parallel$ Modes

When discretizing Eqs. (4.6) and (4.7) on the aforementioned phase space grid – including the time domain – one encounters the following problem: Naturally, every finite difference representation of the spatial derivative ∂_z can only be an approximation to the exact expression. For example, using a second-order centered stencil (as provided in Tab. 4.1),

$$\frac{\partial \Phi}{\partial z} \to \frac{\Phi(z+\Delta z) - \Phi(z-\Delta z)}{2\Delta z} \quad , \tag{4.10}$$

on an equidistant z grid with grid spacing Δz, and assuming a disturbance of the form $\Phi(z) \propto \exp(ik_\parallel z)$, one obtains

$$ik_\parallel \Phi \to \frac{\sin(k_\parallel \Delta z)}{k_\parallel \Delta z} ik_\parallel \Phi \equiv h(k_\parallel) ik_\parallel \Phi \quad . \tag{4.11}$$

The same applies to $\partial_z F_1$. This means that the physical value of $k_\parallel$ in Eq. (4.9) is replaced by an effective value $k_\parallel^\mathrm{eff} = h(k_\parallel) k_\parallel$. In the case of Eq. (4.11), $h(k_\parallel)$ is symmetric about $k_\parallel \Delta z = \pi/2$; in particular, $k_\parallel^\mathrm{eff} \to 0$ as $k_\parallel \to \pi/\Delta z$. This latter property is shared by higher-order centered schemes as well as other non-dissipative schemes.

It is well-known that the growth rates of linear ITG modes in unsheared slab geometry fall off with increasing $k_\parallel$ and even become negative, provided $k_\parallel$ is sufficiently large (see Goldston and Rutherford [50]). At the same time, centered finite difference representations of Eqs. (4.6) and (4.7) will yield modes with

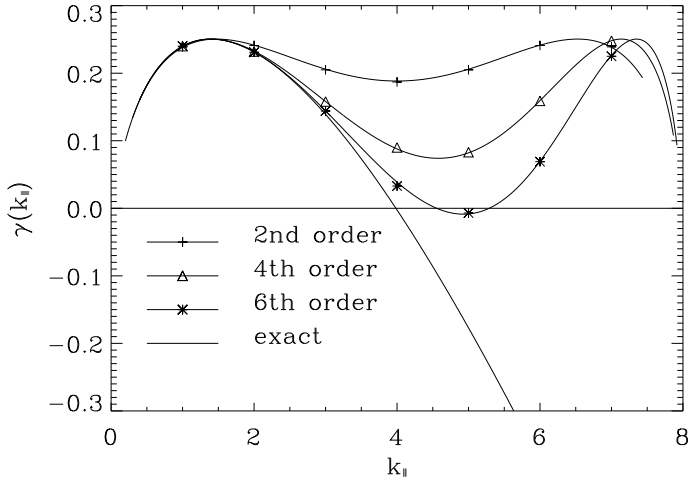

Figure 4.1: Linear growth rates of slab ITG modes as functions of the parallel wavenumber, $k_\parallel$, for different parallel discretization schemes. The curve labeled *exact* was obtained by numerically solving the dispersion relation, Eq. (4.9), while the other curves show the impact of centered schemes of different order and their respective values of $k_\parallel^{\mathrm{eff}}$. The corresponding data points have been obtained using the initial value code described in the text. Note that here, $k_\parallel$ is given in units of $2\pi/N_z$.

high $k_\parallel$ that are linearly unstable. This effect is clearly unphysical and may pollute gyrokinetic simulations of plasma turbulence. In a saturated quasi-steady state, such numerically destabilized modes may contain a significant amount of energy which is transferred to them via nonlinear processes. The profiles of Φ or other fluctuating quantities in z space may then exhibit a sawtooth-like structure. Although in a more realistic case that includes magnetic curvature, this problem tends to be reduced, slab-like modes can be important even then (see Ref. [51]), making it necessary to deal with the issue of high-$k_\parallel$ perturbations in order to retain physicality of simulation results. An intuitive approach to deal with this problem is to introduce numerical dissipation. In the following, this method is discussed in more detail.

In Fig. 4.1, the linear growth rates $\gamma(k_\parallel)$ of slab ITG modes are shown for cases where low-order centered discretization schemes (as listed in Tab. 4.1) were used for the parallel coordinate; the solutions of the dispersion relation, Eq. (4.9), using the exact and the modified effective values for $k_\parallel$, are displayed for comparison.

For the lowest $k_\parallel$ mode ($k_\parallel = 1$ in the figure), the exact solution of the dispersion relation and the Vlasov code show very good agreement, independently of the employed parallel scheme. As $k_\parallel$ is increased, however, significant deviations are observed – in particular, the numerical growth rates do not follow the exact solution into the range of negative values for high $k_\parallel$. Instead, they increase again and reach values comparable to the growth rate of the $k_\parallel = 1$ mode.
This behavior can be understood in terms of the fact that $k_\parallel^{\text{eff}} \to 0$ for $k_\parallel \to \pi$, as has been discussed above. In the case of the second-order scheme, specifically, $\gamma(k_\parallel)$ is symmetric about $k_\parallel = \pi/2$, which is reflected by Eq. (4.11). While higher order centered schemes perform slightly better (due to the fact that the symmetry is broken), they ultimately encounter the same problem for sufficiently high $k_\parallel$. Two possible solutions – using upwind differencing schemes and introducing diffusion terms to stabilize high-$k_\parallel$ modes – will be discussed next.

4.2.3 The Impact of Upwind Schemes and Diffusion Terms

Upwind Schemes

Unlike their centered counterparts, upwind-type schemes (see Tab. 4.1) are known to be numerically dissipative. In the present context, this feature is important in that it has a stabilizing effect on the high-$k_\parallel$ modes which otherwise are destabilized numerically. The disadvantage of upwind differencing is two-fold: Firstly, upwind schemes are of lower order than centered schemes for a given stencil width; for the same number of allocation points, the maximum order of the upwind scheme is one less than that of the corresponding centered scheme. Secondly, the dissipative effect of the scheme cannot be controlled, possibly resulting in an unphysical influence on the simulation or causing inapplicability in different areas where significant numerical dissipation may be required.
It is important to note that upwind differencing in Eq. (4.6) should not be applied to the potential Φ. This would lead to severe time step restrictions, as has been shown by Dannert and Jenko [52]. For this reason, only the term $\partial_z F_1$ may be treated by upwind schemes, while the term $\partial_z \Phi$ is always discretized by means of a centered scheme with a stencil width identical to that of the upwind scheme for $\partial_z F_1$. More specifically, for a given upwind scheme in Tab. 4.1, the centered scheme in the line directly below it is used.
Upwind schemes exhibit some similarities to diffusion terms, as will be shown below. In particular, high-$k_\parallel$ modes are stabilized – as they should be, physically, according to the solutions of the dispersion relation, Eq. (4.9). Thus, upwinding is one way to solve the issue of numerical high-$k_\parallel$ instability.

Numerical Diffusion

High-$k_\parallel$ modes can also be damped by introducing an additional diffusive term $D_n F_1$ on the right-hand side of the Vlasov equation (4.6) which contains an n-th spatial derivative of the distribution function (with an even number n). The resulting new Vlasov equation reads

$$\frac{\partial F_1}{\partial t} + \left[\omega_n + \omega_\mathrm{i}\left(v_\parallel^2 - \frac{1}{2}\right)\right] ik_y \Phi F_0 + \alpha_\mathrm{i} v_\parallel \nabla_\parallel F_1 + \tau_\mathrm{e}\alpha_\mathrm{i} v_\parallel \nabla_\parallel \Phi F_0 = D_n F_1 \quad , \tag{4.12}$$

where n is an even and positive integer number, $\nabla_\parallel \equiv \partial_z$, and D_n is defined as

$$D_n \equiv -i^n \eta_n \nabla_\parallel^n \quad . \tag{4.13}$$

The inclusion of $-i^n$ requires the factor η_n to be positive in order to obtain a stabilizing effect, and is motivated by the ansatz $F_1 \propto \exp(ik_\parallel z)$. η_n can be used to regulate the strength of the diffusion, as well as include additional dependencies, as desired.
Using a stencil with $n+1$ points and centered finite difference schemes for both $\nabla_\parallel$ (n-th order) and $\nabla_\parallel^n$ (second order), the addition of the diffusive term to the Vlasov equation can be interpreted as a mere modification of the finite difference scheme for $\nabla_\parallel F_1$. For instance, in the $n = 2$ case, the second order centered schemes for $\nabla_\parallel$ and $\nabla_\parallel^2$ read

$$\nabla_\parallel^{\{2\}} = \frac{1}{2\Delta z}\,[-1 \quad 0 \quad 1] \quad , \quad \left(\nabla_\parallel^{\{2\}}\right)^2 = \frac{1}{(\Delta z)^2}\,[1 \quad -2 \quad 1] \quad , \tag{4.14}$$

where the number in curly brackets denotes the order of the scheme. On the other hand, the first order scheme for $\nabla_\parallel$ is given by the one parameter (c_2) family

$$\nabla_\parallel^{\{1\}} = \nabla_\parallel^{\{2\}} + c_2 \Delta z \left(\nabla_\parallel^{\{2\}}\right)^2 \quad . \tag{4.15}$$

For arbitrary scheme orders, this relation becomes

$$\nabla_\parallel^{\{n-1\}} = \nabla_\parallel^{\{n\}} + c_n \Delta z^{n-1} \left(\nabla_\parallel^{\{2\}}\right)^n \quad , \tag{4.16}$$

such that, for the present case,

$$\frac{\partial F_1}{\partial t} + \alpha_\mathrm{i} v_\parallel \nabla_\parallel^{\{n\}} F_1 + i^n \eta_n \left(\nabla_\parallel^{\{2\}}\right)^n F_1 = \ldots \tag{4.17}$$

can be replaced by

$$\frac{\partial F_1}{\partial t} + \alpha_\mathrm{i} v_\parallel \nabla_\parallel^{\{n-1\}} F_1 = \ldots \quad , \tag{4.18}$$

assuming that $\eta_n \propto (\Delta z)^{n-1}$, and splitting off the prefactor $\alpha_\mathrm{i} v_\parallel$ from η_n. If one chooses $\eta_n \propto (\Delta z)^m$, with $m < n$, the combined scheme is of m-th order, while

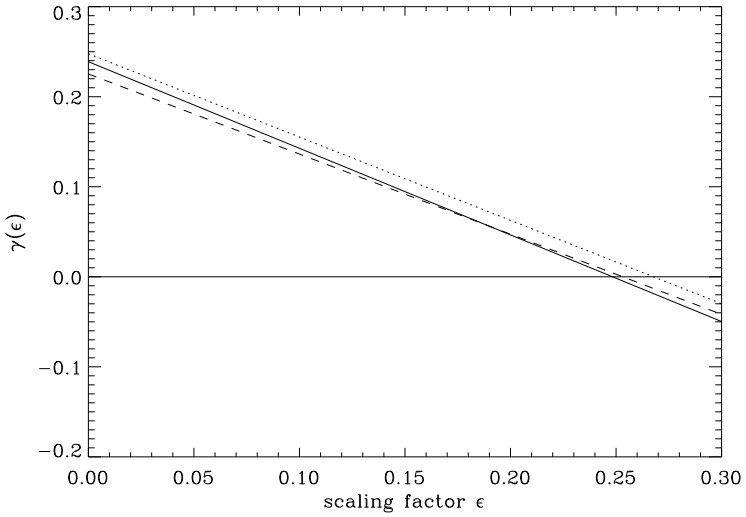

Figure 4.2: Growth of the $k_\parallel = 7$ mode for a spatial resolution of $N_z = 16$, depending on ϵ for second (solid), fourth (dotted), and sixth order (dashed) diffusion term. At $\epsilon = \epsilon_c \approx 0.25$, the curves cross the abscissa, marginally stabilizing the seventh mode at this point. Here, $k_\parallel$ is specified in units of $2\pi/N_z$.

for $m \geq n$, it is of n-th order, just as the original scheme. This will prove to be relevant later on, when the scaling $\eta_n \propto (\Delta z)^n$ is chosen in order to make the diffusion coefficient ϵ – to be defined below in Eq. (4.22) – independent of the spatial resolution.

In the following, a critical diffusion coefficient $\eta_n^{\rm crit}$ shall be presented for which all physically stable modes of the curve in Fig. 4.1 representing the solution of the dispersion relation are also numerically stable. The value of $\eta_n^{\rm crit}$ depends on the order of the scheme, as well as on the spatial resolution and the set of physical parameters. For the dispersion relation, Eq. (4.9), the fastest growing mode is usually characterized by $k_\parallel = 1$ (in units of $2\pi/N_z$). However, the mode with the highest $k_\parallel$, here: $(N_z/2 - 1)$, will have a similar growth rate due to $k_\parallel^{\rm eff} \to 0$ for $k_\parallel \to N_z/2$. To identify the value and functional dependencies of $\eta_n^{\rm crit}$, one thus has to find the value of η_n for which the $k_\parallel = (N_z/2 - 1)$ mode is marginally stable.

The diffusion-extended Vlasov equation (see Eq. (4.12)), leads to a modified dispersion relation,

$$1 + \tau_{\rm e} + (\tau_{\rm e}\bar{\psi} + \varpi_{n{\rm i}})Z(\bar{\psi}) + \varpi_{T{\rm i}}Y(\bar{\psi}) = 0 \quad , \tag{4.19}$$

where $\bar{\psi} \equiv \varpi + ik_\parallel^{n-1}\eta_n/\alpha_\mathrm{i}$. Note that Eq. (4.12) is valid only if D_n (and thus η_n) is independent of $v_\parallel$. The new dispersion relation has the same form as the original one (and therefore the same solution, only now for $\bar{\psi}$ instead of ϖ), Eq. (4.9); thus, an imaginary number $ik_\parallel^{n-1}\eta_n/\alpha_\mathrm{i}$ is subtracted when comparing the original ϖ with the new one. The corresponding numerical damping rate is proportional to $k_\parallel^n$ (since $\omega = k_\parallel \varpi$) which is consistent with the goal to stabilize high-$k_\parallel$ modes while influencing low-$k_\parallel$ modes at little as possible. The impact on the growth rate can thus be written as

$$\Delta\gamma \equiv \gamma_\mathrm{diff} - \gamma = -\eta_n (k_\parallel^\mathrm{diff})^n \quad , \tag{4.20}$$

where γ_diff is the growth rate of a mode as given by the diffusive Vlasov equation, Eq. (4.12), and $k_\parallel^\mathrm{diff}$ is the effective wave number for the diffusion term. It is defined similarly to $k_\parallel^\mathrm{eff}$, only for a second order n-th derivative. For $n = 2$, its high-$k_\parallel$ limit is given by

$$\lim_{k_\parallel \Delta z \to \pi} k_\parallel^\mathrm{diff} = \lim_{k_\parallel \Delta z \to \pi} \left(\frac{2 - 2\cos(k_\parallel \Delta z)}{(\Delta z)^2} \right)^{1/2} = \frac{2}{\Delta z} \quad . \tag{4.21}$$

In this particular limit, one always obtains the same result, independently of n. Demanding that $\eta_n \propto (k_\parallel^\mathrm{diff})^{-n}$ – which is suggested by Eq. (4.20) – one can rewrite the diffusion coefficient,

$$\eta_n = \epsilon \left(\frac{\Delta z}{2} \right)^n \quad , \tag{4.22}$$

which yields a new diffusion coefficient ϵ that is independent of both Δz and n. This leads to a new form for the diffusion term:

$$D_n = -i^n \eta_n^{(\mathrm{crit})} \nabla_\parallel^n = -i^n \epsilon_{(\mathrm{c})} \left(\frac{\Delta z}{2} \right)^n \nabla_\parallel^n \quad . \tag{4.23}$$

Using this expression, numerical simulations confirm that the critical value ϵ_c is independent of the resolution Δz and the order n of the scheme. Even for low resolutions, only small deviations were found. As is illustrated in Fig. 4.2, $\epsilon_\mathrm{c} \approx 0.25$ for the present choice of physical parameters. Also note that, as mentioned before, the combination of centered scheme and n-th derivative is of order n, due to $\eta_n^\mathrm{crit} \propto (\Delta z)^n$.

The range of allowed values for the diffusion coefficient is limited on the lower end by the appearance of high-$k_\parallel$ modes, motivating a lower boundary $\epsilon_\mathrm{min} \approx \epsilon_\mathrm{c}$, and by numerical stability issues on the higher end. For a given time step, ϵ cannot be increased indefinitely – at a certain value, the diffusion term will become unstable, losing its previous damping effect; this is illustrated in Fig. 4.3.

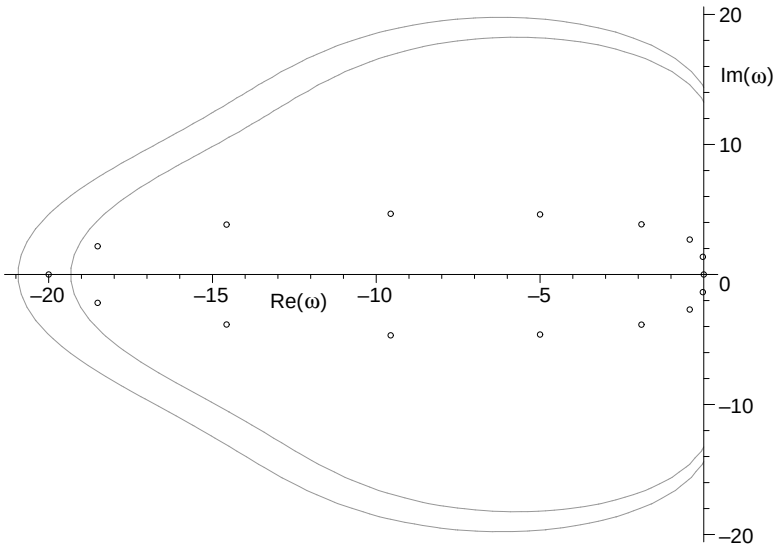

Figure 4.3: Stability regions (contours) of the third order Runge-Kutta explicit time stepping scheme, along with the eigenvalue cloud (circles) of a fourth order spatially differenced Vlasov system ($N_z = 16$) with a diffusion term as described in the text. While the spatial resolution is responsible for stretching the cloud along the imaginary axis, increasing the diffusion coefficient will elongate the cloud along the negative real axis. Once an eigenvalue lies outside the stability region, the simulation will become unstable. The time resolutions shown here are $\Delta t = 0.12$ (outer contour) and $\Delta t = 0.13$ (inner contour). Note that an unrealistically high diffusion coefficient $\epsilon = 20$ has been chosen here to show its time step limiting property.

Analogously to the Courant limit, there exists a maximum ϵ above which the simulation becomes numerically unstable. In reality, however, this value lies far beyond the order of magnitude investigated here. The Courant limit remains the most restrictive factor in determining the time step. Note that while in the case of multi-species, finite-β simulations at non-zero $\hat{s}$, much higher values of ϵ are common, the time step also is much smaller to allow for the inclusion of the electron dynamics. Such cases are discussed in Chs. 5 and 6.
For a third order Runge-Kutta time scheme, the maximum value for ϵ is determined to be

$$\epsilon_{\max}^{\mathrm{RK3}} = \frac{(4+\sqrt{17})^{1/3} - (4+\sqrt{17})^{-1/3} + 1}{\Delta t} \approx \frac{2.5127}{\Delta t} \quad . \tag{4.24}$$

This relation can be obtained by equating the diffusion coefficient ϵ (which, for even N_z, corresponds to the location of the eigenvalue with the most negative real part) to the leftmost zero point of the time stepping stability regime (which is calculated by Taylor-expanding a complex exponential function) and is independent of the spatial resolution if the time step is assumed to be limited by the diffusion term alone, i.e., not by the Courant limit. For practical purposes, one can simply write

$$\epsilon \leq \frac{2.5}{\Delta t} \quad . \tag{4.25}$$

Note that this value is much larger than the above $\epsilon_{\mathrm{c}} = 0.25$ for any realistic time step. For a typical $\Delta t = 0.1$ (which is rather large compared to common values in GENE simulations), $\epsilon_{\max}$ exceeds ϵ_{c} by two orders of magnitude.
In terms of the scaling factor ϵ of the diffusion term, one can recalculate the results for the centered schemes displayed in Fig. 4.1, using values $\approx \epsilon_c$; those new results are shown in Fig. 4.4. Thus, it is demonstrated that the problem caused by the high-$k_\parallel$ modes has been resolved without significantly affecting the physical modes of the system.
By changing the set of physical parameters of the problem, a different choice of ϵ_c may become necessary. In principle, one would have to make a readjustment after every change of a physical quantity. In practice, however, there is some freedom as to what value ϵ_{c} can be set to. This is illustrated by the influence of the diffusion term on the low-$k_\parallel$ modes: A relative deviation of 6×10^{-5} from the diffusion-less result is found for $k_\parallel = 2\pi/N_z$ at sixth order with $\epsilon_{\mathrm{c}} = 0.25$, making the result mostly independent of the precise value. For the next higher $k_\parallel$, the deviation is 3×10^{-3}, which is still reasonably small.
However, if the changes to the physical parameters become significant, one has to identify the new value of ϵ_{c}. Generally, this is done by determining the ap-

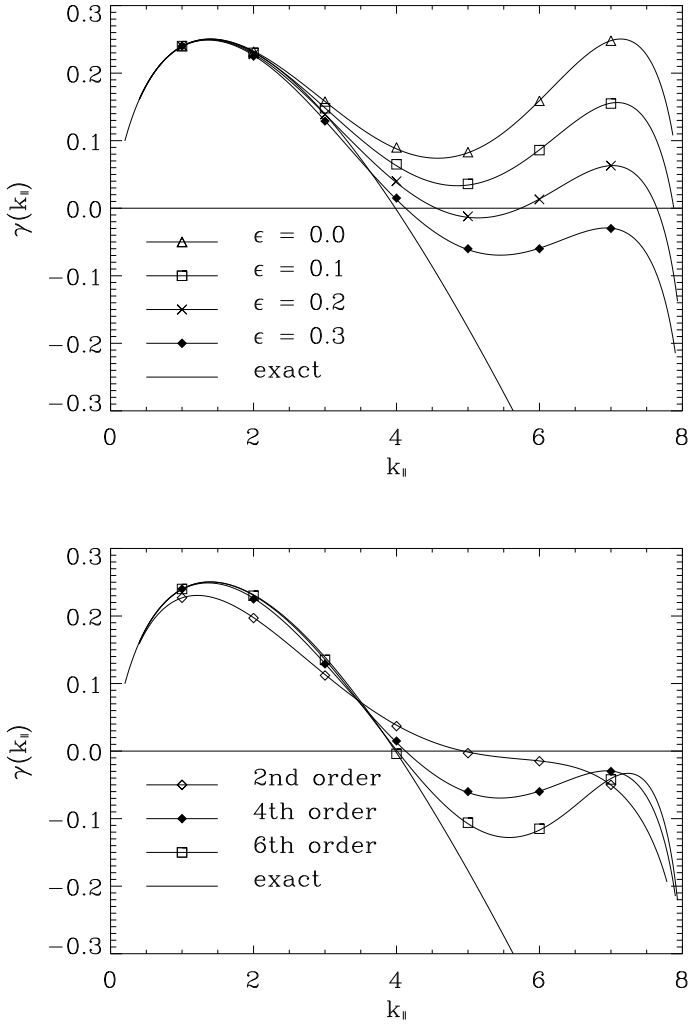

Figure 4.4: Linear growth rates of slab ITG modes for different parallel discretization schemes of constant fourth order for a range of ϵ values (upper graph), and constant diffusion $\epsilon = 0.3$ for a range of scheme orders (lower graph).

proximate linear growth rate of the lowest $k_\parallel$ mode and setting ϵ to that value:

$$\epsilon_\mathrm{c}(\mathcal{PP}) = \gamma(k_\parallel^\mathrm{min}, \mathcal{PP}) \quad , \tag{4.26}$$

where $\mathcal{PP}$ symbolizes a set of physical input parameters. This prescription seizes to work when the dispersion relation changes in a way that the intermediate range (here, this would correspond to a value of $k_\parallel \approx 8\pi/N_z$) is contributing significantly to the physics. However, in such a case, the physics would likely not be resolved sufficiently anyway, requiring a higher parallel resolution; then, the above ϵ_c will again be sufficient to dampen unwanted high-$k_\parallel$ modes.
One can show that the aforementioned upwinding is simply a special case of diffusion: working with a $2n+1$ point stencil, employing an n-th order centered scheme for $\nabla_\parallel$ as well as a second order centered scheme for $\nabla_\parallel^n$, and using the respective choice of the following η_n:

$$\eta_2^\mathrm{upw} = \alpha_\mathrm{i}\|v_\parallel\|\frac{\Delta z}{2} \tag{4.27}$$

$$\eta_4^\mathrm{upw} = \alpha_\mathrm{i}\|v_\parallel\|\frac{(\Delta z)^3}{12} \tag{4.28}$$

$$\eta_6^\mathrm{upw} = \alpha_\mathrm{i}\|v_\parallel\|\frac{(\Delta z)^5}{60} \tag{4.29}$$

one obtains the $(n-1)$-th order upwind stencil.
However, diffusion is the more desirable choice compared to upwind differencing for two reasons: firstly, its order is n, compared to $n-1$ for upwinding, where n is the order of the employed centered scheme; secondly, it can be fine tuned, allowing for more precise regulation of the impact on both the physical and the numerical modes. At the same time, using a diffusion term requires only slightly more effort – to find the value of ϵ_c, one only needs an estimate of the growth rate. Therefore, introducing a diffusion term – or, more correctly for most cases, a hyperdiffusion term – is the preferable choice.
Since for this research, a strongly simplified model was used, it is important to note how directly and with what impact the thus obtained results can be applied to more general cases, i.e.: kinetic electrons, more complex geometry, and magnetic fluctuations, described no longer in a drift-kinetic but a gyrokinetic fashion. Performing simulations with the GENE code, one finds that for most cases, the above prescription (as given in Eq. (4.26)) holds true; one of these scenarios, involving simulations of ETG turbulence, is described in more detail further down in this chapter. However, finite magnetic shear, in conjunction with finite plasma β, will cause zigzag-like structures in the magnetic potential $A_\parallel$ which then are transfered onto other quantities. The reason for this lies in the

properties of $A_\parallel$, along with the parallel boundary conditions at finite $\hat{s}$ and finite radial resolution; however, since the mechanism causing this numerical feature is not identical to the one discussed above, the aforementioned prescription fails if applied without modification. In fact, one can either choose very high radial resolutions, or increase the diffusion coefficient to values of $\epsilon \sim 10$. The latter is computationally much less expensive and thus the preferred solution. Cases where this prescription is applicable are discussed in Chs. 5 and 6. If gyrokinetic simulations are performed in the electrostatic limit or in unsheared geometry, however, the method of determining the diffusion coefficient ϵ as detailed above can be expected to hold.

4.3 Recurrence Phenomena

4.3.1 Decaying Zonal Flows

Zonal flows (see, e.g., Hasegawa and Wakatani [53], or Ch. 5) are modes with a purely radial structure that can be excited nonlinearly by turbulent processes. In a linear, collisionless model, they are damped, typically within a few ten to a hundred time units. In order to investigate zonal flows linearly, one can initialize a k_x mode that is constant in both toroidal and poloidal direction, and subject this mode to time evolution via the Vlasov equation. However, this setup is susceptible to so-called recurrence phenomena in a finite resolution code, i.e.: the initial amplitude of the zonal mode is remembered by the code and reproduced after half the recurrence time $t_{\mathrm{rec}} = 2\pi/(\alpha_{\mathrm{i}} \Delta v_\parallel)$. Again, this recurrence problem can be solved by the use of numerical diffusion. Since the $(1+1)$-dimensional slab model described above cannot capture the physics involved here, the GENE code was used for the numerical simulations detailed below.

As can be seen in Fig. 4.5, a damped mode recurs after a certain time for no physical reason. This behavior may pollute linear as well as nonlinear simulations. While the theoretically predicted residual level (see Rosenbluth and Hinton [54] for more details) of the mode,

$$A_R = \frac{1}{1 + 1.6 q_0^2/\sqrt{\epsilon_t}} \quad , \tag{4.30}$$

is reproduced correctly (again, q_0 is the safety factor and ϵ_t the inverse aspect ratio), energy is reinserted numerically into the system at multiples of the recurrence time t_{rec} after the initial occurrence of the mode. For these simulations, the following set of physical parameters was used: the driving gradients were set to zero in order to isolate the effect of recurrence and a more complex magnetic

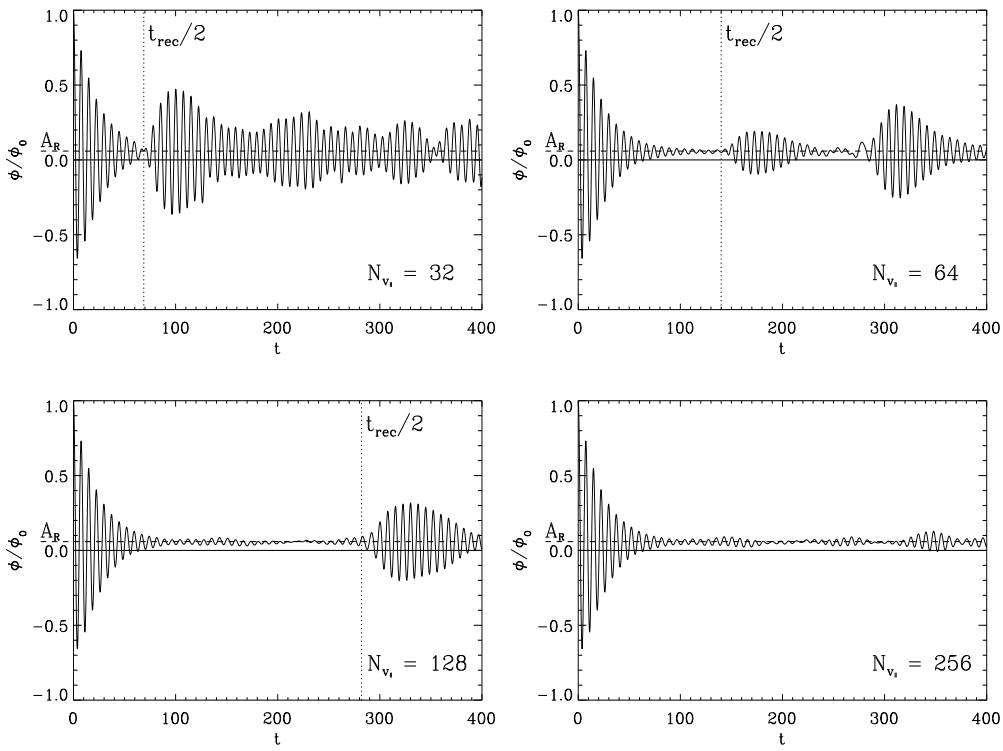

Figure 4.5: Velocity space resolution dependence of linear simulations of zonal modes; the displayed quantity is the normalized electrostatic potential Φ. From the upper left to the lower right graph, the parallel velocity space resolution $N_{v\|}$ is increased successively by factors of 2 from 32 to 256 points. Note that the recurrence time $t_{\rm rec} = 2\pi/(\alpha_{\rm i}\Delta v_{\|})$ doubles for each such step, an effect which is reflected by the results. The dashed line corresponds to the (physical) residual level A_R of the modes, as given in the text.

geometry was introduced to allow for the formation of zonal flows, with $q_0 = 2$, $\hat{s} = 0.8$, and $\epsilon_t = 0.16$. Linear results (with adiabatic electrons) for $k_y = 0.02$ were obtained with resolutions of $N_x = 16$, $N_z = 16$, $N_\mu = 8$, and $N_{v_\parallel} = 64$ unless specified otherwise. Note that for a stable mode ($\gamma \leq 0$), following the prescription for parallel dissipation as given before yields $\epsilon = 0$.

4.3.2 Velocity Space Diffusion

The Impact of Resolution

The problem can be partially mitigated by increasing the velocity space resolution: as a consequence, the recurrence time increases as well, while the strength of the re-emerging oscillations decreases, as illustrated in Fig. 4.5. This method, however, is expensive in that rather high $v_\parallel$ resolutions are required, making it impractical. Instead, one can either include a physical collision term or utilize a diffusion term to solve the problem. The latter approach – while being numerical in nature in contrast with the physical basis for collisions – constitutes the less expensive solution. It will be described in more detail below.

Numerical Diffusion

Parallel (spatial) diffusion as discussed above helps to reduce the amplitude of the oscillations, but cannot be used at liberty, for it would influence other results (e.g., the growth rate) too strongly, especially when a physically stable system is being considered, as is the case with linearly decaying zonal flows. Also, parallel diffusion has an impact on the residual level A_R, since over time, energy is removed from the system numerically. This is illustrated in the upper half of Fig. 4.6, where significant parallel diffusion has to be employed in order for the recurrence to vanish. The required values exceed those for damping high-$k_\parallel$ modes that have been discussed before.
Alternatively, or additionally, a similar diffusion term can be introduced which acts on the parallel velocity space:

$$D_4^{(v\parallel)} = -\epsilon_{v\parallel} \frac{(\Delta v_\parallel)^4}{16} \partial_{v\parallel}^4 \quad . \tag{4.31}$$

This term is inserted into the gyrokinetic Vlasov equation (see Eq. (2.65)) to modify the $v_\parallel$ derivative.
Here, a fourth derivative is chosen for the diffusion term to be used with the first derivative of fourth order in the magnetic mirror term (which contains the $v_\parallel$ derivative). It solves the issue efficiently, as becomes evident from the lower

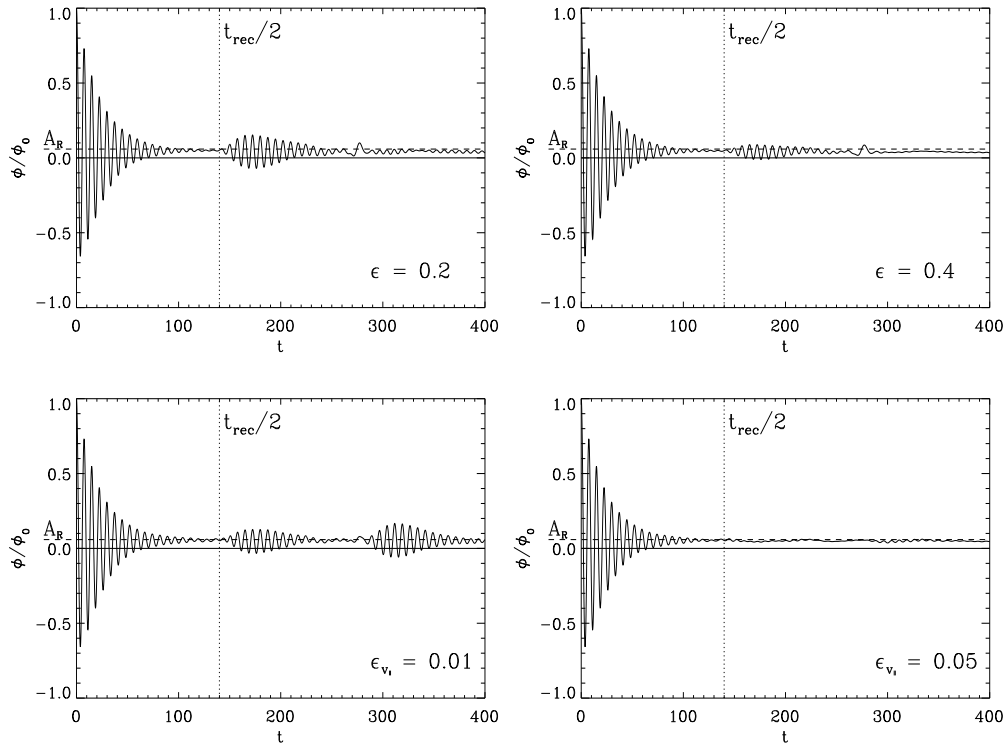

Figure 4.6: Numerical damping of zonal modes; the two upper graphs show the effect of parallel diffusion, whereas in the lower graphs, velocity space diffusion is employed. For the former, the value of ϵ is increased from 0.2 to 0.4, while for the latter, the results shown here are for values $\epsilon_{v\|} = 0.01$ and 0.05, respectively. Again, A_R is the residual level.

graphs in Fig. 4.6; compared with the spatial parallel diffusion approach, only very little velocity diffusion is necessary to avoid practically all recurrence.

While clearly, the point where recurrence vanishes is not well-defined and the necessary damping depends on the resolution, the value $\epsilon_{v\|} = 0.05$ makes for a good starting point for the most efficient solution to the recurrence problem, velocity space damping. Since the value is rather low and changes the (negative) growth rate only by a factor of 10^{-4}, there is some freedom to adjust the velocity space diffusion to higher values, if necessary. In practice, neither recurrence nor alteration of physical effects have been observed for $\epsilon_{v\|} = 0.2$ for a wide range of physical scenarios.

4.4 Treatment of Parallelly Extended Modes

4.4.1 The Extended Ballooning Representation

By using a Fourier-like ballooning transformation (see, e.g., Candy et al. [55]), modes that extend beyond the standard parallel 2π range can be investigated. Linear modes tend to have their maximum at $k_x = 0$ and thus peak in the parallel range of $\theta = -\pi \dots \pi$, while falling off further out on both sides (at nonzero k_x values). Viewing the parallel mode structure by obtaining x averaged data hides this feature; instead, one has to take k_x resolved data and apply the ballooning transformation, shown here for the electrostatic potential Φ:

$$\Phi_{\mathrm{B}}(k_y, \theta_p) = \Phi(k_x(p), k_y, \theta) \quad , \tag{4.32}$$

where $\theta_p = \theta + 2\pi p$, $p \in \mathbf{Z}$ is the extended ballooning angle, and $k_x(p)$ connects the j-th k_x mode with the $(j \pm \mathcal{N})$-th mode. This prescription extends the entire mode parallelly by use of the boundary condition (see Eq. (2.51)), i.e., increasing values of $\|k_x\|$ are considered as one moves away from the central 2π range. Note that for nonlinear simulations, the parallel boundary condition causes the number of relevant k_x modes to drop as k_y increases. Thus, extended ballooning structures are usually only resolved for the lowest k_y values, partially reducing the applicability of the findings reported here to nonlinear cases.
Due to finite resolution, the mode eventually enters the 2π range corresponding to the last connected k_x, and after this, is set to zero (which corresponds to $f(\|i_{kx}\| > N_{kx}) = 0$ if the modes are numbered $-N_{kx} \dots N_{kx}$). Therefore, if the mode has not dropped to sufficiently small amplitudes at this point, it will make a sudden jump to zero; this behavior successively acts back on the other parallel points and k_x modes via the parallel derivative in the Vlasov equation and the boundary condition – because centered stencils tend to couple points which are $2\Delta z$ apart, zigzag-like features can appear in the parallel structure.
Since that effect is clearly unphysical, one has to compensate either by increasing the radial resolution (i.e., adding more k_x modes), by adjusting the parallel diffusion coefficient ϵ, or by introducing a radial diffusion term. While the first solution is expensive, the latter two force one to make sure that the resulting growth rates do not change significantly.
In order to investigate the issue, a standard case is used, taking Cyclone Base Case parameters (see Dimits et al. [56] or Ch. 5 for more details) with adiabatic electrons and performing linear GENE simulations (at $k_y = 0.2$) on a phase space grid with $N_z = 16, N_{v\parallel} = 32$, and $N_\mu = 8$. The velocity space diffusion coefficient is set according to the above result, $\epsilon_{v\parallel} = 0.05$, and parallel diffusion is turned

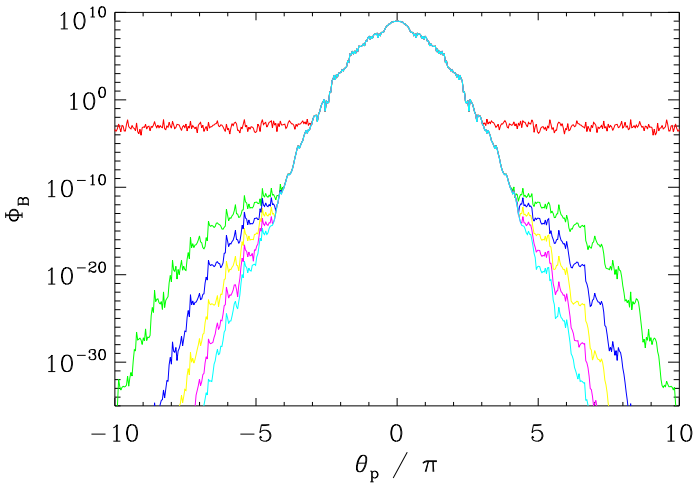

Figure 4.7: Modes in the extended ballooning representation. Turning on radial diffusion damps the ballooning mode more strongly as one connects to higher radial modes, i.e. with increasing $\|\theta_p\|$. The values shown here for the radial diffusion coefficient are $\epsilon_x \in \{0, 1, 2, 3, 4, 5\}$, corresponding to the colors red, green, blue, yellow, magenta, and cyan, respectively. Note that in the center, all curves overlap perfectly.

off. High-$k_\parallel$ modes do not contribute significantly here, but it nonetheless serves for a good description of parallelly extended modes.

4.4.2 Radial Diffusion Term

A radial diffusion term is inserted in the Vlasov equation; since the radial coordinate is represented in Fourier space, no stencils have to be employed, and instead, multiplications by (even) powers of k_x make up the derivatives – a term $\propto k_x^4$ is chosen as the default value. However, to be consistent, the radial diffusion coefficient ϵ_x is defined similarly to ϵ, with the radial diffusion term defined corresponding to its parallel counterpart in Eq. (4.23).
Naturally, the impact of the radial diffusion is effectively zero in the central 2π range (where $k_x = 0$). The further the mode stretches out from that point, however, the more the mode can be damped, as becomes evident from Fig. 4.7. The required strength of the damping varies with the motivation for using the diffusion term; however, if one encounters zigzag-like structures that come from the parallel boundary condition in conjunction with the finite radial resolution,

one may dampen the outer wings of the mode in the extended ballooning representation to reduce the effect. This can be done without altering the central – i.e., the physically dominant – mode structure significantly.
Unlike the other types of diffusion discussed in this chapter, the use of radial diffusion is less universal. Only certain simulation scenarios may benefit from the inclusion of a radial diffusion term, and in some of those cases, it can be avoided by adjusting the parallel diffusion.

4.5 An Application: the ETG Benchmark

4.5.1 Benchmark Parameters

Recently, an effort has been undertaken to construct a standard set of parameters for electron temperature gradient (ETG) driven turbulence; details were published by Nevins et al. [57], as well as by Dimits et al. [58]. It is meant to serve as a benchmark case similar to the Cyclone Base Case – their physical input parameters are mostly identical, with the exception of the magnetic shear, where smaller values are required to achieve saturation, the basic setting being $\hat{s} = 0.1$. Unlike in the Cyclone Base Case, however, the electrons are the primary species, with the ions being treated adiabatically. Using this benchmark case, the influence of parallel diffusion on the nonlinearly saturated heat flux level is investigated, demonstrating the applicability of the results presented above. Also, convergence studies are performed.
The resulting heat flux levels of the (nonlinear) benchmark depend on the number of k_y modes that are being considered. Separate levels are reported in Ref. [57] for $N_{ky} = 8$ and $N_{ky} = 16$, namely $\chi_\mathrm{e} \approx 3$ and $\chi_\mathrm{e} \approx 5$, respectively. The work presented here focusses on the latter case with higher resolution. The other resolutions are chosen as $N_x = 128$ (for a perpendicular box with $L_x \times L_y = 100 \times 62.8$), $N_z = 16$, $N_{v_\parallel} = 32$, and $N_\mu = 8$.

4.5.2 Impact of the Parallel Diffusion Term

Setting the radial and parallel velocity space diffusion coefficients to low but finite values of $\epsilon_x = 0.1$ and $\epsilon_{v_\parallel} = 0.05$, respectively, the parallel diffusion coefficient is increased. The results are shown in Fig. 4.8; clearly, the $\epsilon = 0$ result of $\chi_\mathrm{e} = 1.2$ deviates significantly from the other values, while for higher values, a plateau at $\chi_\mathrm{e} \approx 5$ is reached for $N_{ky} = 16$; the corresponding result for $N_{ky} = 8$ is $\chi_\mathrm{e} \approx 3$, which agrees well with the other codes in Ref. [57], as can be seen in Fig. 4.9.

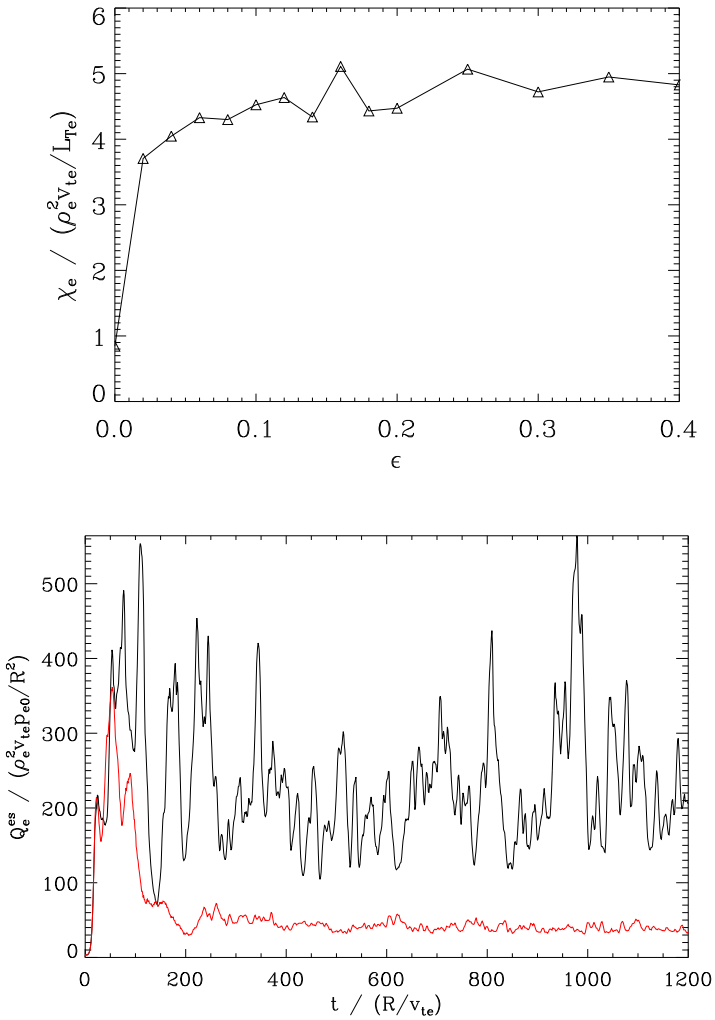

Figure 4.8: Thermal diffusivities for increasing parallel diffusion ϵ and $N_z = 16$ (upper graph) in the ETG benchmark case. While for $\epsilon = 0$, the value is far too low, increasing diffusion creates a stable plateau over most of the range displayed (where small deviations from the plateau are due to the burst-prone nature of the operation point); for higher parallel resolution, the results are practically identical. The picture is corroborated by the time traces of the heat flux, as shown in the lower graph, where the diffusion-less case (red curve) exhibits qualitatively very different behavior from the $\epsilon = 0.3$ case (black curve).

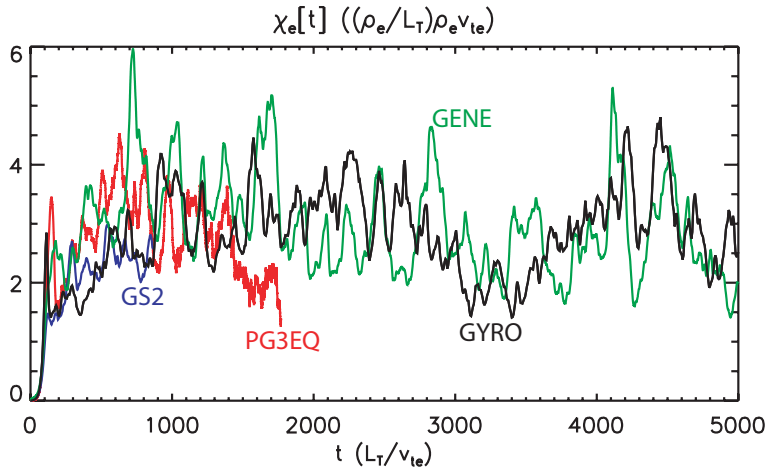

Figure 4.9: Agreement of multiple gyrokinetic codes (both Vlasov and Particle In Cell) at ETG benchmark parameters. The case presented here uses 8 modes to resolve the y direction, resulting in a lower saturation value of $\chi_e \approx 3$ compared with the $N_{ky} = 16$ case. Source: [57]

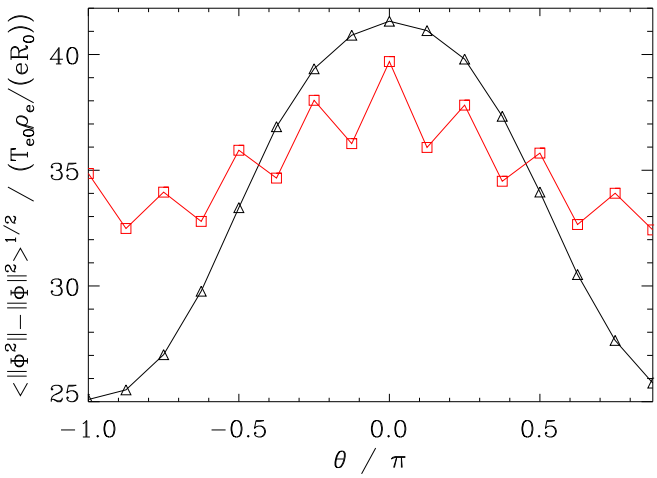

Figure 4.10: Parallel structure of the root mean square of the electrostatic potential for $\epsilon = 0$ (red squares) and $\epsilon = 0.3$ (black triangles). High-$k_\parallel$ modes resulting from the parallel derivative in the Vlasov equation are suppressed at $\epsilon = 0.3$, retaining physicality of the simulation results. Note that for purposes of comparison, the $\epsilon = 0$ results were rescaled by a factor of 1.8.

Fig. 4.10 contains the parallel mode profiles for $\epsilon = 0$ and 0.3. In the diffusion-less case, zigzag-like structures appear which are clearly unphysical. This problem is taken care of by increasing the diffusion coefficient, which is precisely what was aimed for by introducing the diffusion term in Eq. (4.12).
The impact of parallel diffusion also becomes visible in the turbulent field contours in the x-y plane, as shown in Fig. 4.11: zonal flows – which should not dominate in ETG turbulence – are observed if no diffusion is used, while turning on numerical diffusion makes it possible for streamers to take over which corresponds to the physical expectations (see, e.g., Refs. [59] and [60]). Since sometimes, these streamers cover the entire box, it might be necessary to adjust the standard box of the benchmark if one looks to obtain more physical results.

4.6 Chapter Summary

This chapter aimed to solve the issue of numerically excited high-$k_\parallel$ modes, with two approaches being investigated: upwind differencing and diffusion terms. It is found that the most efficient and flexible solution is using a diffusion term $D_n f$ with a diffusion operator of the form

$$D_n = -i^n \epsilon_\mathrm{c} \left(\frac{\Delta z}{2}\right)^n \nabla_\parallel^n \tag{4.33}$$

with a critical diffusion coefficient ϵ_c set to a value roughly equal to the linear growth rate γ. Other possibilities of using numerical diffusion terms are discussed, with parallel velocity space diffusion combating numerical recurrence phenomena, and radial diffusion altering the structure of extended ballooning modes to avoid unphysical effects due to the parallel boundary condition. Lastly, it is shown in the context of an ETG benchmark that those results apply for a standard physical scenario.

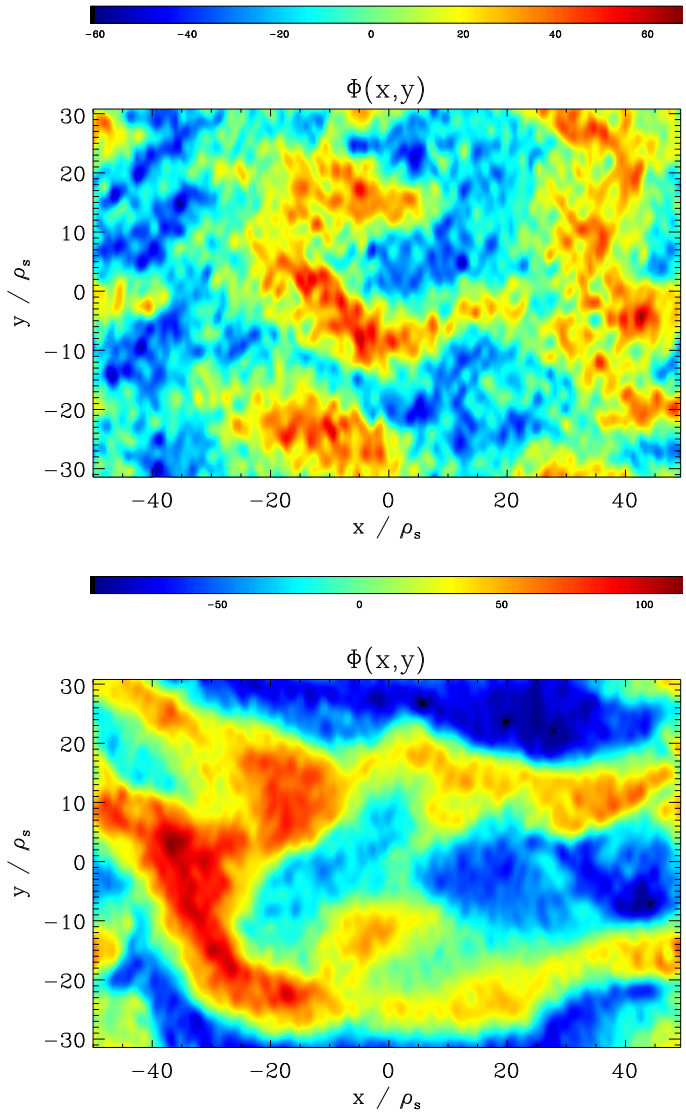

Figure 4.11: Contours of the electrostatic potential in the x-y plane. In the upper graph ($\epsilon = 0$), there are no streamers present, while instead, a tendency to form zonal flows can be observed. Below, diffusion ($\epsilon = 0.3$) can be seen to suppress any occurrence of zonal flows, while streamers are significant part of the turbulence, matching the physical expectations.

Chapter 5

Electromagnetic Cyclone Base Case

Electromagnetic effects – which occur when, due to finite plasma pressure, the magnetic field experiences fluctuations which then act back on the plasma – can modify the strength and even type of plasma microturbulence significantly. Following a brief motivation which includes a discussion of experimental results, such effects are studied by examining the Cyclone Base Case parameter set. In part, this chapter follows Pueschel et al. [61].

5.1 The Normalized Plasma Pressure β

5.1.1 Definition and Significance

The normalized plasma pressure β is one of the most essential dimensionless parameters characterizing a fusion plasma. Reiterating the definition in Ch. 2, it is taken to be

$$\beta \equiv \beta_\mathrm{e} = \frac{8\pi n_\mathrm{e} T_\mathrm{ref}}{B_\mathrm{ref}^2} \quad , \tag{5.1}$$

in words: the ratio of the kinetic to the magnetic pressure, for the present work. Multiple important effects depend on this quantity. Firstly, the bootstrap fraction f_BS is proportional to β. This fraction describes how much of the plasma current that drives the poloidal magnetic field is generated from within the plasma as opposed to being induced by the transformer coil. Generally, the diamagnetic nature of finite orbit radii of charged particles lead to net currents in the presence of density gradients. In a tokamak configuration, trapped particles – which are reflected by the higher magnetic field on the inboard side of the torus – cause a current in the toroidal direction; the resulting net momentum is then transferred

to passing particles via collisions, causing a toroidal current (see, e.g., Refs. [62] and [63]). In recent experiments, f_{BS} values of 100% have been achieved (see, e.g., Ushigome et al. [64]). Even values $f_{\mathrm{BS}} > 1$ are feasible, leading – in principle – to the possibility of using bootstrap current overdrive to extract energy from the plasma via the transformer coil.
Providing a second positive effect, fusion reaction rates are proportional to β^2: in a finite volume, the number of particles are proportional to β, and assuming a given (temperature-dependent) cross-section, the rates of two-particle reactions must be $\propto \beta^2$.
As a consequence, it is desirable to operate a tokamak at the highest β possible without destroying the confinement. Unfortunately, large-scale – magnetohydrodynamic (MHD) – instabilities of various types are known to impose an upper β limit, most prominently the MHD ballooning mode which sets in at a critical value $\beta_{\mathrm{crit}}^{\mathrm{MHD}}$; additionally, neoclassical tearing modes (NTMs) appear at a certain β value, altering the magnetic field structure by creating magnetic islands which reduce the confinement; and even below these thresholds, the confinement may be influenced unfavorably by β (although experimental evidence is still inconclusive, as will be discussed below). Similarly, small-scale – gyrokinetic – instabilities driving turbulent fluctuations may affect the plasma performance in the high β regime. The latter can happen in basically two ways. First, electrostatic microinstabilities like ITG or trapped electron modes (TEMs), along with the respective kinds of turbulence, are altered in the presence of magnetic field fluctuations which are caused by finite plasma pressure (those fluctuations will be discussed in more detail further down). The anomalous transport properties may thus be changed significantly with respect to the electrostatic limit, affecting the plasma confinement. Second, in the framework of a gyrokinetic description, kinetic ballooning modes (KBMs) are potentially prone to be destabilized below the MHD ballooning limit, causing large heat and particle transport and effectively reducing the achievable plasma β. Therefore, in order not to operate reactors at less-than-optimal efficiency, it is important to fully understand the properties of KBM onset $\beta_{\mathrm{crit}}^{(\mathrm{kinetic})}$, its relation to $\beta_{\mathrm{crit}}^{\mathrm{MHD}}$, as well as the behavior of the transport close to that operational point.

5.1.2 Experimental Findings

Experimental β Scalings

Tokamak experiments have yielded widely differing results for the scaling of the energy confinement time τ_E with β (at fixed toroidal field B_t), as is illustrated

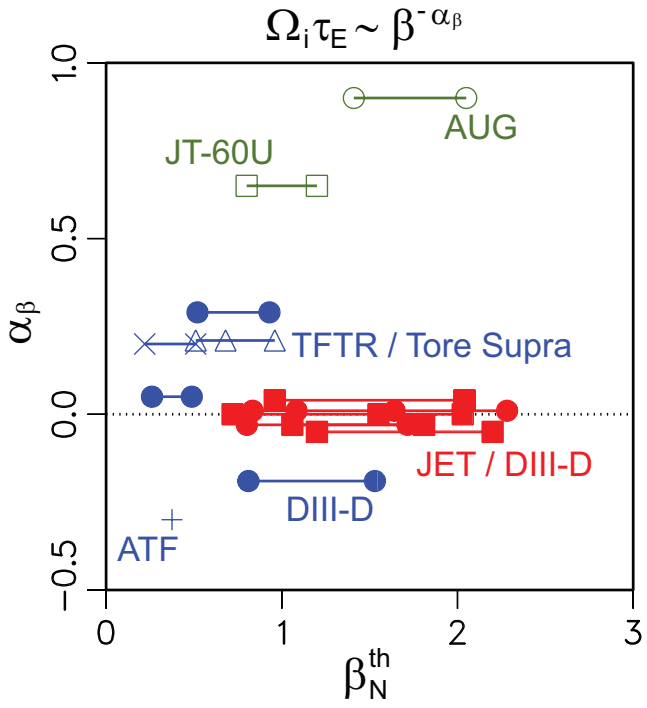

Figure 5.1: Scaling of the normalized confinement time τ_E with $\beta_N^{th} \propto \beta$ for a number of tokamak experiments. The exponent α_β is defined by the relation $\Omega_i \tau_E \propto \beta^{-\alpha_\beta}$; more recent JET data (see Ref. [65]) with $\alpha_\beta = 1.4$ is not included in this figure. From this graph, it becomes clear that experiments produce widely differing results concerning the scaling of the confinement time with β. Source: [66]

in Fig. 5.1 where exponents α_β of the relation $\Omega_i \tau_E \propto \beta^{-\alpha_\beta}$ are shown. For some, very little or no dependence was reported, e.g., for DIII-D and earlier JET discharges (see Refs. [67] and [68], respectively). On the other hand, the predictions for the ITER reactor (as given by the IPB98$(y, 2)$ ITER scaling [69]) have $\alpha_\beta = 0.9$, resulting in a strongly unfavorable scaling, a finding that is corroborated by other experiments: Urano et al. [70] find $\alpha_\beta = 0.6$ at JT-60U, Vermare et al. [71] find $\alpha_\beta = 0.9$, and more recent JET experiments have $\alpha_\beta = 1.4$, as reported by McDonald et al. [65].

Possible Causes for Discrepancies

Clearly, one cannot derive a general scaling from these results which apply only to their respective scenarios. On one hand, fixing all other plasma parameters to perform a pure β scan constitutes a significant experimental challenge; however, if, e.g., the gradients are varied only by a small factor while changing β, confinement may be affected more by the former than by the latter, rendering the interpretation of a β scan questionable. Another problem connected to this fact lies in the large error bars of many measurements.

On the other hand, even if a range of experiments were measured, analyzed, and interpreted flawlessly, they might be operated in parameter regimes that are dominated by different physical effects; for instance, experiments with dominant ITG turbulence would be expected to show a different β scaling than experiments with dominant TEM turbulence, leading to apparently inconsistent results. For more discussion on parameter differences of the scaling experiments, see Vermare et al. [71]. Additionally, it needs to be taken into consideration that plasma edge processes can strongly affect confinement. Lastly, there is a possibility that some of the results suffer from a too small β scanning range [72].

All these factors show that it is highly desirable to gain a more solid understanding of the underlying physical processes. Theoretical advances in this field might help understand where the disagreement in experimental findings may have had its origin.

5.2 The Cyclone Base Case

The so-called Cyclone Base Case (henceforth: CBC) refers to a discharge at the DIII-D tokamak; experimental details concerning that discharge were published by Greenfield et al. [73]. It exhibits typical tokamak core turbulence and has since been established as a standard scenario for numerical simulations, most

ω_{Ti}	6.89
ω_{Te}	6.89
ω_{n}	2.22
$\hat{s}$	0.786
q_0	1.4
ϵ_t	0.18
$T_{\mathrm{ref}} = T_{\mathrm{i}} = T_{\mathrm{e}}$	

Table 5.1: The Cyclone Base Case parameter set used in the present work. A more detailed description is available in Dimits et al. [56].

prominently described by Dimits et al. [56]. However, most past work has been focused on electrostatic simulations, and until recently, gyrokinetic turbulence simulations have been limited to β levels significantly lower than the ballooning threshold.

5.2.1 Physical Parameter Set

The CBC physical parameter set is often adjusted for specific investigations; for instance, one might use adiabatic electrons, or, in the case of kinetic electrons, choose a realistic or a reduced mass ratio. The parameters used in this work are listed in Tab. 5.1.

In the electrostatic limit, this parameter set corresponds to a physical regime that is dominated by ITG modes, both linearly and nonlinearly. However, as β is increased, other instabilities eventually surpass the ITG modes, as will be shown below.

Note that while technically, one has to adjust the geometry parameter responsible for the Shafranov Shift, $\alpha_{\mathrm{MHD}}(\beta) = \beta q_0^2(2\omega_n + \omega_{T\mathrm{i}} + \omega_{T\mathrm{e}})$, consistently with the β value, $\hat{s}$-α geometry is used here with α_{MHD} set to zero unless specified otherwise. This is done to allow for easier comparison with previous work which was using the same setting. However, as will be demonstrated, finite α_{MHD} values have only a very small effect if investigations are confined to β values not too far above the ballooning threshold.

Before listing simulation details and discussing physical effects, some past results of CBC simulations are presented to provide a foundation for this investigation.

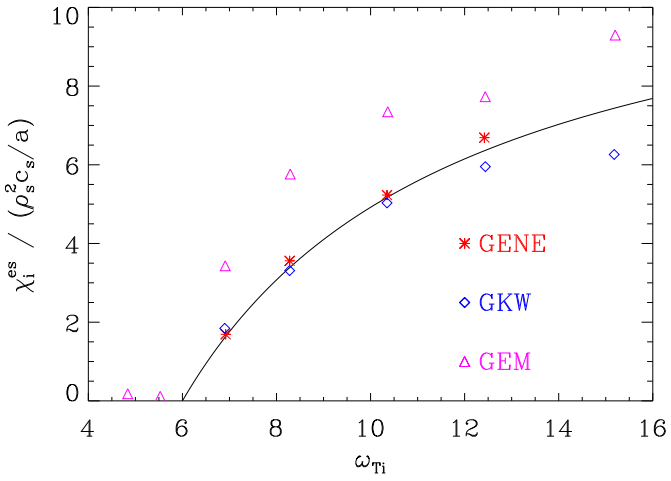

Figure 5.2: Ion heat diffusivities as functions of the ion temperature gradient, $\omega_{T\mathrm{i}}$, from the ITM benchmark. The solid black curve represents the Dimits fit as specified in the text; GENE, GKW, and GEM results are shown as red stars, blue diamonds, and pink triangles, respectively. At $\omega_{T\mathrm{i}}$, ITG modes become stable nonlinearly, a result that is reproduced well by all codes. a denotes the minor radius of the last closed flux surface.

5.2.2 The ITM Benchmark Effort

A benchmark at CBC parameters is used to outline a few more (electrostatic) properties of this physical scenario here while demonstrating good agreement between codes. First results from the international Integrated Tokamak Modeling effort were published by Falchetto et al. [74], some of which are quoted here.
Dimits et al. [56] specifies a fit curve for the ion thermal diffusivity as a function of the ion temperature gradient; it can be written as

$$\chi_{\mathrm{i}}^{\mathrm{es}} \frac{a}{\rho_s^2 c_s} = 12.3 \left(1.0 - 6.0 \frac{L_{T\mathrm{i}}}{R_0}\right) \quad . \tag{5.2}$$

As becomes evident from Fig. 5.2, there is excellent agreement of GENE data with this fit curve; also, reasonably good agreement with GEM (gyrofluid – effects due to magnetic trapping are neglected here; see Ref. [75]) and GKW (gyrokinetic, see Refs. [76] and [77]) is observed. Precise measurement of this dependency is important if one aims to calculate the Dimits shift which predicts a nonlinear upwards shift of the critical gradient for the onset of ITG turbulence compared with the stability threshold of linear ITG modes.

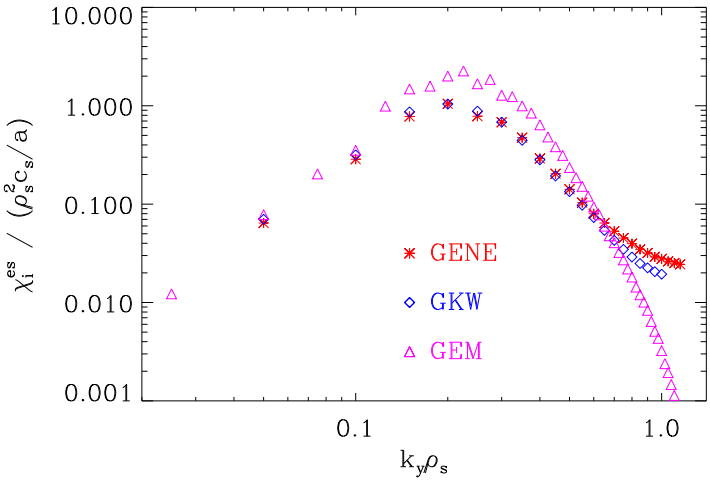

Figure 5.3: k_y spectra of the ion heat flux, from the ITM benchmark. GENE, GKW, and GEM results are shown as red stars, blue diamonds, and pink triangles, respectively. While GENE and GKW agree very well – especially in the larger vicinity of the peak – GEM shows slightly different behavior quantitatively, which is consistent with the results displayed in Fig. 5.2.

Similarly good agreement among codes is found for toroidal flux spectra (as shown in Fig. 5.3). While the moderate differences between GENE and GEM are likely connected to the similarly moderate differences in the transport levels, there is remarkably good agreement between GENE and GKW over a wide range of wave numbers, lending credibility to the physical relevance of the results within the gyrokinetic framework.

5.2.3 Previous Electromagnetic Work

Multiple gyrofluid and gyrokinetic simulations with finite β have been performed over the last few years. On the gyrofluid side, Snyder and Hammett [78] use somewhat different physical parameters than those of the CBC to find a stabilizing effect of β on both the linear growth rate and nonlinear transport levels. These results agree qualitatively with CBC simulations by Scott [79] where ITG transport eventually drops to zero, shortly before saturation can no longer be achieved at higher β.
Gyrokinetic investigations include Jenko and Dorland [59] who found excellent agreement between the onset points of MHD and kinetic ballooning modes (at

CBC parameters), as well as strongly declining transport with increasing β for ETG turbulence. Chen et al. [80] use a modified version of the CBC with $\omega_{T\mathrm{e}} = 0$, linearly reproducing the stabilizing effect due to increasing β, as well as doing so schematically for the nonlinear case at low β values. Parker et al. [81] also have slightly decreasing transport, as does Candy [82]. However, with the exception of Candy [82], no in-depth analyses of the electromagnetic CBC are presented, and even here, β still remains far below the KBM threshold.

5.2.4 Code-Code Comparisons

Growth rates and low-to-moderate β transport levels as computed with GENE, GS2 (for details on the code, see Kotschenreuther et al. [83]), and GYRO (the results for which were reported in Ref. [82]) are presented to provide a good physical basis for further simulations. The physical parameters that these results were obtained for are identical for all three codes and correspond directly to the CBC parameter set.

Fig. 5.4 shows linear growth rates, as computed by these three codes; while there is good qualitative agreement, some quantitative differences are found for higher β values (near the ballooning threshold) where GYRO results deviate from their GENE and GS2 counterparts. So far, the reasons for this discrepancy are unknown, as the GENE and GS2 values were checked thoroughly for convergence, while lack of access to the GYRO code prevented additional probing. Still, β values safely below the threshold show good quantitative agreement of all codes, and GENE and GS2 agree very well over the entire range.

As becomes evident in Fig. 5.5, there is significant overlap of nonlinear GYRO and GENE results in all transport channels. Slight resolution issues are highlighted; however, they do not change the qualitative picture. In Ref. [81], findings for the same scenario are reported where the decrease of the ion transport with increasing β is smaller, but the absolute levels are similar.

An electromagnetic benchmark effort by Nevins (for a previous effort by the same author on ETG turbulence, see Nevins et al. [57] or Ch. 4) has been embarked on recently which is supposed to shed more light on physical as well as numerical properties of microturbulence as β is increased.

Having ascertained that GENE produces robust and inter-code compatible results both linearly and in the nonlinear β range available for comparison, investigations of linear as well as nonlinear properties of electromagnetic effects shall be presented.

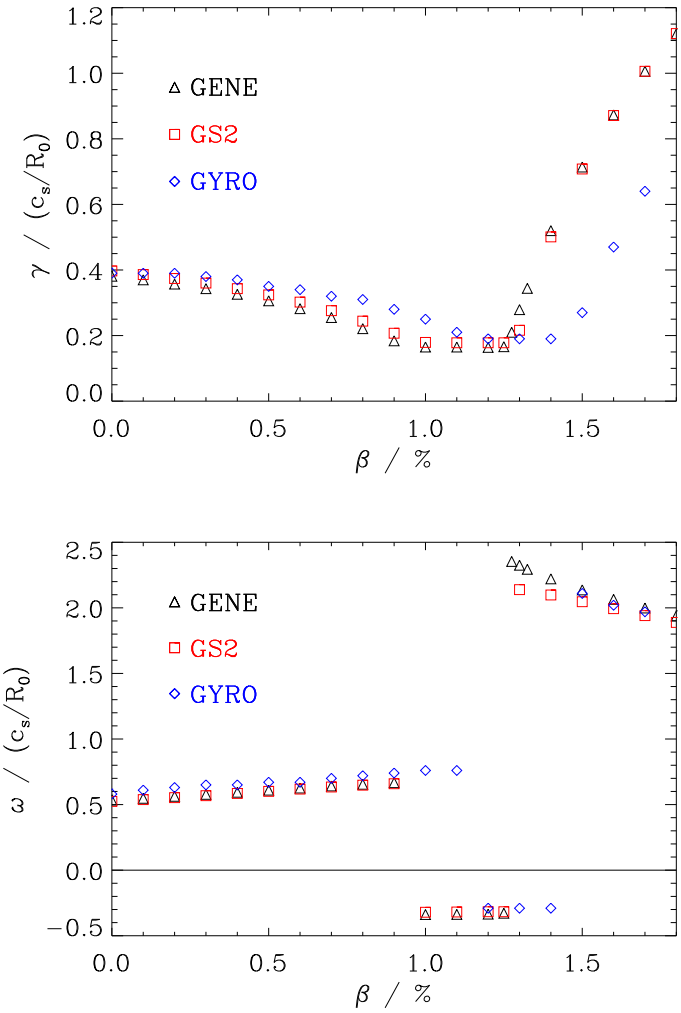

Figure 5.4: Linear growth rate (upper) and frequency (lower) dependence on β as computed with the GENE (black triangles), GS2 (red squares), and GYRO (as reported in Ref. [82]; blue diamonds) codes. While the former two agree remarkably well over the entire range, GYRO results seem to be stretched along the β axis. As of now, the reason for this discrepancy remains unclear.

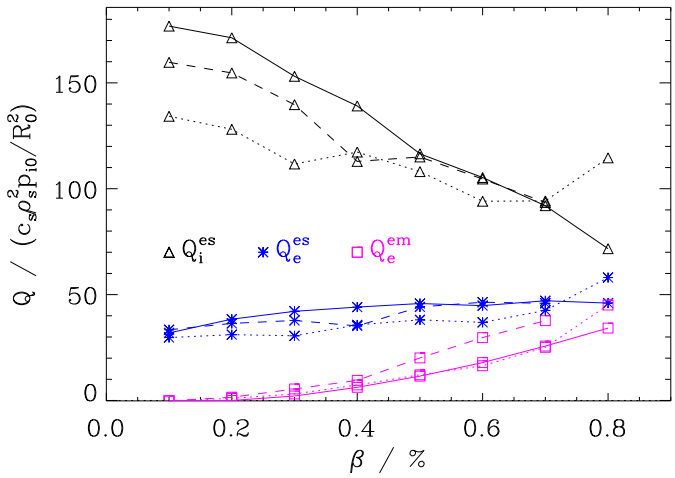

Figure 5.5: Comparison of nonlinear GENE and GYRO (as reported in Ref. [82]; dotted lines) transport levels: black triangles represent the ion electrostatic heat flux, blue stars the electron electrostatic heat flux, and pink squares the electron electromagnetic heat flux). For GENE, both the reference values (solid lines) and additional simulation results (dashed lines; with lower resolution, more comparable to the GYRO results taken from Ref. [82]) are shown.

5.3 Linear Results

5.3.1 Numerical Settings

For most simulations performed here, the following set of numerical parameters is used: The electrons are treated kinetically with a mass of $m_\mathrm{e}/m_\mathrm{i} = 5.669\times10^{-4}$, corresponding to a hydrogen plasma. For the simulation box,

$$L_y = \frac{2\pi}{k_y} \quad , \quad L_x = \frac{1}{\hat{s}k_y} \quad , \quad L_z = 2\pi q_0 R_0 \tag{5.3}$$

are chosen, with $L_{x,y}$ in units of ρ_s (and wave numbers in units of ρ_s^{-1}). Throughout this chapter, $L_{v_\parallel} = v_\parallel^\mathrm{max} = 3$ (in units of the thermal velocity v_{Tj}) and $L_\mu = \mu^\mathrm{max} = 9$ (in units of v_{Tj}^2). As to the diffusion coefficients,

$$D_x = 0.2 \quad , \quad D_z = 4 \quad , \quad D_{v_\parallel} = 0.2 \quad , \tag{5.4}$$

which are motivated by the results for electromagnetic simulations presented in Ch. 4. The grid resolutions are $N_x = 24$ (12 modes per sign), $N_z = 24$,

$N_{v\parallel} = 96$ (required for TEMs), and $N_\mu = 16$, based on convergence studies in every instability regime, to achieve convergence throughout the entire β range.

5.3.2 A Linear β Scan

To get an idea what kind of microinstabilities are likely to be responsible for driving the turbulence for the nominal parameters in various β regimes, linear gyrokinetic simulations are performed first, which allow for covering a much larger parameter range due to being computationally significantly less expensive. k_y is chosen to be 0.2 unless specified otherwise, which corresponds roughly to the position of the maximum of the nonlinear transport spectrum, as will be shown later.

In Fig. 5.6, the behavior of the linear growth rate and the frequency with varying β is presented. It is found that at low β values, the dominant microinstability is an ITG mode, as expected. With increasing β, the growth rate of this mode is diminished, however, until a TEM takes over. As eigenvalue calculations with GENE show, the latter mode is unstable across the entire β range, and its linear growth rate is practically not influenced by changes in β, in contrast to the ITG mode. It shall be pointed out for future reference that the TEM growth rate is roughly half that of the ITG mode in the electrostatic limit. As is apparent in Fig. 5.6, at still higher β values, a KBM starts to dominate. Its linear growth rate increases quite rapidly once the respective β threshold has been crossed. The real frequency exhibits a positive sign, which, in the convention used in this work, corresponds to a drift in the ion diamagnetic direction; moreover, the amplitude of this frequency clearly exceeds the ITG frequency, an effect which is discussed, e.g., in Ref. [84]. Within any single regime, only small modifications of the frequencies are observed. Linearly, one thus has two critical β values (which depend on the toroidal wave number and are presented here for the standard case, $k_y = 0.2$): at $\beta = 0.95\%$, a transition from ITG modes to TEMs takes place, and at $\beta = 1.27\%$, KBMs become dominant. The entire next section is devoted to the properties of this latter critical value, possible modifications, and its deviation from the MHD prediction.

5.3.3 Properties of the Kinetic Ballooning Mode

It is well known that MHD ballooning modes only become linearly unstable when β exceeds a certain (plasma parameter dependent) threshold. The same is true for their gyrokinetic counterpart, the KBMs. These thresholds need not coincide, however. Using a simplified analytical model, Chu et al. [85] estimate the kinetic

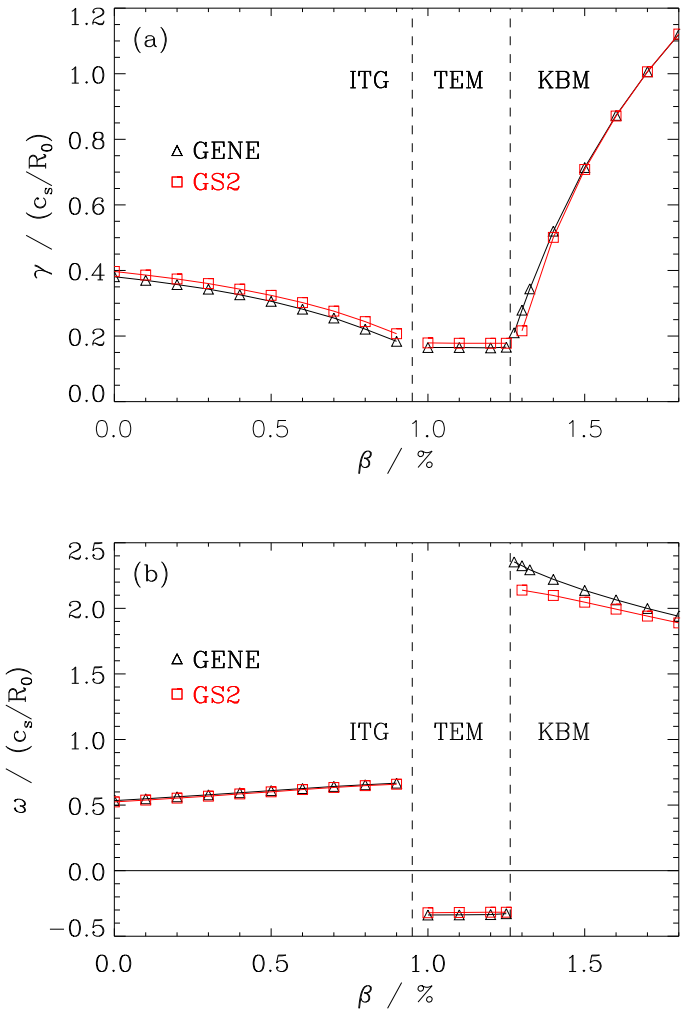

Figure 5.6: Dependence of the growth rate γ (a) and the real frequency ω (b) on β for $k_y = 0.2$. GENE results are shown as black triangles, GS2 results as red squares. Clearly, three instability regimes can be discerned: ITG, TEM, and KBM, with regime changes marked by clear jumps in the frequency.

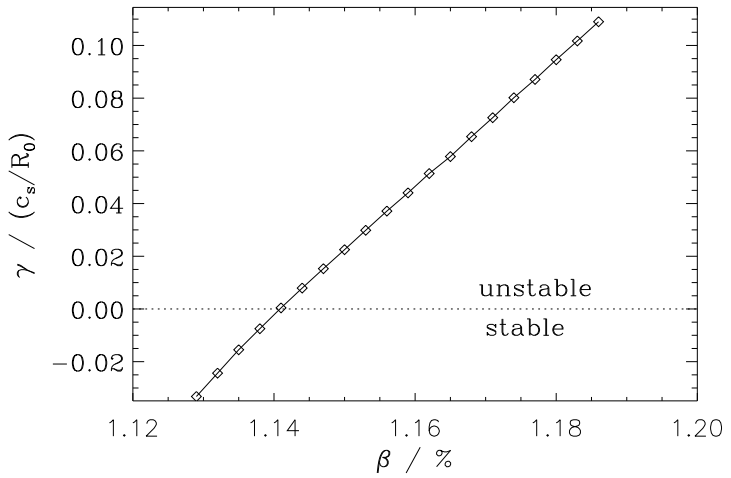

Figure 5.7: Growth rates of the kinetic ballooning mode in the subdominant range where the TEM is dominant. At $\beta = 1.14\%$, the mode becomes linearly unstable. No marginal stability is observed below this value.

value to be reduced compared to the MHD prediction:

$$\beta_{\mathrm{crit}} \equiv \beta_{\mathrm{crit}}^{\mathrm{kinetic}} = \frac{\beta_{\mathrm{crit}}^{\mathrm{MHD}}}{1+\epsilon_t} \quad . \tag{5.5}$$

Similarly, Cheng [86] finds a small but nonzero reduction using numerical methods, but still neglecting some fundamental kinetic effects. Later, Zonca et al. [87], as well as Dong et al. [88], reported that the KBM onset can go significantly below the respective MHD value under certain conditions, with reductions by up to about 50%, a claim that was disputed later by Zhao and Chen [89]. This short summary of previous findings pertains to radially local investigations. For nonlocal results, see, e.g., Falchetto et al. [90]. At present, it is not clear if those numbers can be confirmed in the context of a reasonably comprehensive gyrokinetic approach. The work presented here is supposed to shed some light on this issue.

Since the KBM onset can be obscured in the presence of other microinstabilities like ITG modes or TEMs (as is the case in Fig. 5.6) if growth rates $\gamma(\beta)$ are calculated via an initial value solver, one may use GENE in its eigenvalue solver mode to study the properties of the KBM onset. The (subdominant) behavior of the KBMs obtained this way is shown in Fig. 5.7. Clearly, the respective linear growth rate crosses into the negative range at $\beta_{\mathrm{crit}} = 1.14\%$; however, two addi-

tional aspects are noteworthy about this finding: Firstly, these particular KBMs (at $k_y = 0.2$) are subject to substantial linear damping below the β threshold (i.e., no marginally stable behavior is observed for $\beta < \beta_{\mathrm{crit}}$), rendering it less likely that they play a role in respective nonlinear simulations. Secondly, the inferred value for β_{crit} is about 14% below the MHD ballooning limit; the latter can be estimated as

$$\beta_{\mathrm{crit}}^{\mathrm{MHD}} = \frac{0.6\hat{s}}{q_0^2(2\omega_n + \omega_{T\mathrm{i}} + \omega_{T\mathrm{e}})} \quad , \tag{5.6}$$

which, for CBC parameters, yields $\beta_{\mathrm{crit}}^{\mathrm{MHD}} = 1.32\%$. Note that this reduction agrees very well with the above formula by Chu et al. [85] (see Eq. (5.5)) which, for this case, predicts a value of $\Delta\beta_{\mathrm{crit}}/\beta_{\mathrm{crit}} = 15\%$. Neither this quantitative nor this qualitative behavior is universal, however. Below, cases with very different reduction fractions (as well as cases with $\beta_{\mathrm{crit}} > \beta_{\mathrm{crit}}^{\mathrm{MHD}}$) are presented, as well as scenarios with marginal stability and mode transformations which can occur for different sets of physical parameters. Therefore, Eq. (5.5) is not universally applicable.

Determining the KBM stability threshold by following the mode through the subdominant range until arriving at negative growth rates requires significantly more computational effort than finding the growth rates of dominant modes. If one aims to extract the β values of KBM thresholds for many different sets of physical parameters, this method might thus be somewhat cumbersome. Therefore, it shall be demonstrated how to arrive at a good estimate for β_{crit} by interpolating the dominant growth rate branches of two modes, as well as extrapolating the dominant KBM branch, both of which do not require the less accessible growth rates of subdominant or even stable modes.

The growth rates for the TEM and KBM regime can be fitted well by linear and quadratic functions, respectively. By taking the intersection of these fit functions, the value $\beta_{\mathrm{crit}}^{\mathrm{dom}}$ can be determined at which γ_{KBM} becomes larger than γ_{TEM}; analogously, $\beta_{\mathrm{crit}}^{\mathrm{extrapol}}$ is defined as the value for which the KBM fit function crosses the zero line. Using these prescriptions, one obtains $\beta_{\mathrm{crit}}^{\mathrm{dom}} = 1.26\%$ and $\beta_{\mathrm{crit}}^{\mathrm{extrapol}} = 1.21\%$ for $k_y = 0.2$ in the present case. The corresponding results for other values of k_y are shown in Fig. 5.8, with $\beta_{\mathrm{crit}}^{\mathrm{MHD}}$ included for comparison. It is to be noted that for both the dominant and the extrapolated critical β, the minima lie at $k_y = 0.2$ which is very convenient if one aims to connect linear and nonlinear results – if the minimum had been at very large k_y, it would likely be much more difficult to understand the nonlinear impact of KBMs, as well as their onset.

At this point, it is worthwhile to make a brief remark concerning the effect of

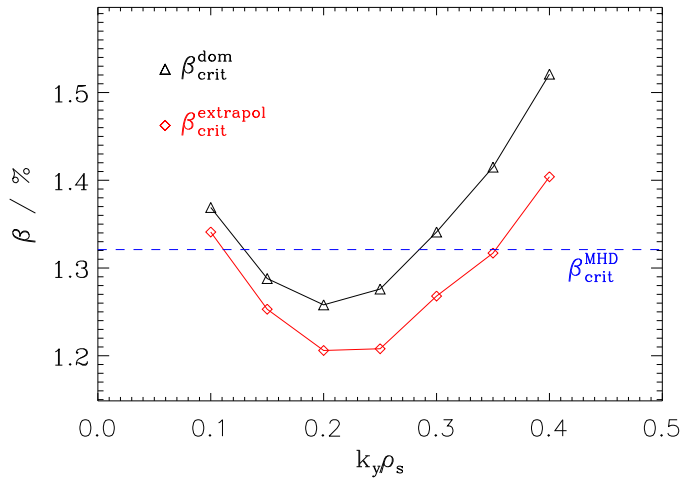

Figure 5.8: Critical values of β for the onset of KBMs and their dominance over TEMs, respectively, for a range of toroidal mode numbers k_y. Black triangles mark the values where the KBMs become dominant, whereas the extrapolated critical β for (subdominant) instability of the KBMs is marked by red diamonds. For comparison, the MHD prediction is shown as a blue dashed line. The minimum lies at $k_y = 0.2$ which roughly corresponds to the nonlinear transport maximum.

setting α_{MHD} to zero. While this was done in the simulations presented here for comparability purposes, one can easily use values consistent with the respective β without any additional computational effort. Little alteration of the growth rates is observed – the critical β values one obtains that way for $k_y = 0.2$ are $\beta^{\mathrm{dom}}_{\mathrm{crit}} = 1.26\%$ and $\beta^{\mathrm{extrapol}}_{\mathrm{crit}} = 1.22\%$, in excellent agreement with the respective $\alpha_{\mathrm{MHD}} = 0$ results. It is concluded that as long as one does not exceed the KBM threshold by a significant factor, α_{MHD} effects are small for the present parameter set. However, it is well-known that for very large β, those effects have to be considered, most prominently for their impact on the so-called second stability regime (see, e.g., Wesson [63]).

Another aspect of interest is how the KBM threshold depends on the density and temperature gradients. Therefore, each gradient is scanned over a certain range, keeping the respective other gradients fixed to their CBC values. Since $\beta^{\mathrm{MHD}}_{\mathrm{crit}}$ is a function of those gradients, it is instructive to look at α_{crit}, as well, for which MHD predicts a near-constant value $\approx 0.6\hat{s}$. The results of this investigation are

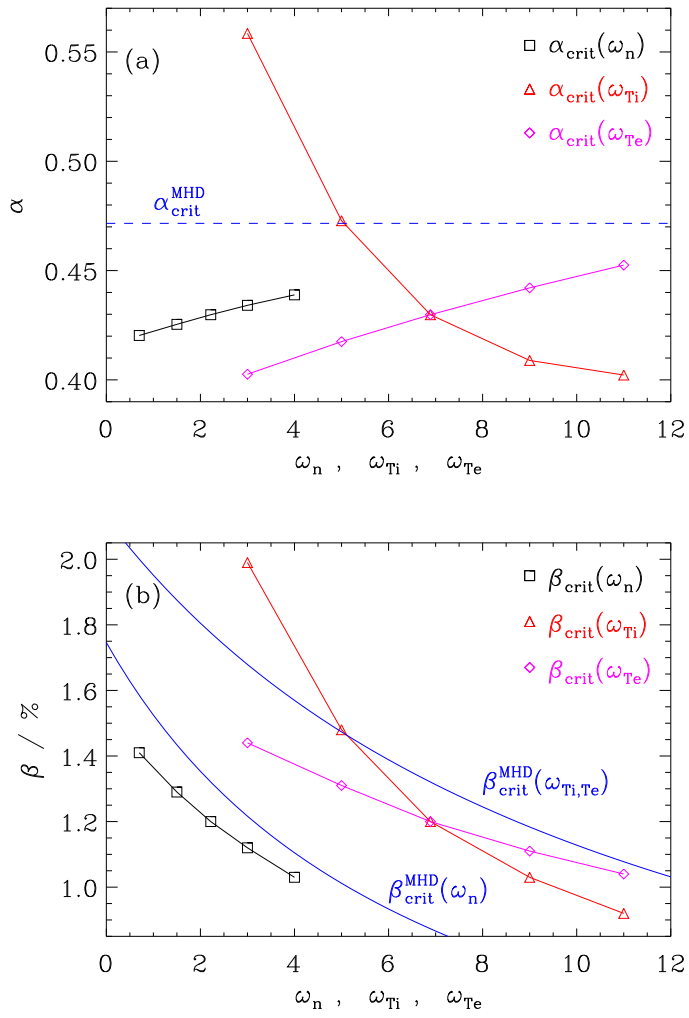

Figure 5.9: Dependence of critical β (a) and α (b) values for the onset of KBMs on the gradients on the density gradient (black squares), the ion temperature gradient (red triangles), and the electron temperature gradient (pink diamonds), at $k_y = 0.2$. For comparison, the MHD predictions are shown in blue. For (b), the $\beta^{\rm MHD}_{\rm crit}(\omega_n)$ line denotes the case where $\omega_{T\rm i}$ and $\omega_{T\rm e}$ are fixed to 6.89, whereas the $\beta^{\rm MHD}_{\rm crit}(\omega_{T\rm i,T\rm e})$ line corresponds to a constant value $\omega_n = 2.22$.

shown in Fig. 5.9. Note that here, only values for $k_y = 0.2$ are included. Obviously, most values of $\alpha_{\text{crit}}^{\text{extrap}}$ deviate only mildly from $\alpha_{\text{crit}}^{\text{MHD}} = 0.472$, especially as far as changes in $\omega_{T\text{e}}$ and ω_n are concerned. However, for large values of $\omega_{T\text{i}}$, the resulting α_{crit} is up to about 15% lower than $\alpha_{\text{crit}}^{\text{MHD}}$. This leads to the conclusion that while, in principle, *all* profile gradients play a role in determining β_{crit}, the biggest effect comes from the ion temperature gradient. This is consistent with previous studies [86, 87] and shows that in a fundamental way, the kinetic ballooning mode is different from its MHD counterpart which relies on the interplay of unfavorable curvature and the density gradient.

As expected, in almost all cases, $\alpha_{\text{crit}}^{\text{extrap}}$ lies below $\alpha_{\text{crit}}^{\text{MHD}}$; however, as $\omega_{T\text{i}}$ is decreased, the KBM stability threshold eventually extends beyond the MHD prediction. While in this regime, no marginally stable low-β behavior was found for $k_y = 0.2$, the $k_y = 0.1$ counterpart shows indeed such a marginally stable tail (marginally stable KBMs are discussed below). Here, $\beta_{\text{crit}} = 1.87\%$ (corresponding to $\alpha_{\text{crit}} = 0.526$) which is again closer to the MHD value. This is consistent with the requirement that as $k_y \to 0$, gyrokinetic results approach MHD theory, in this case: $\beta_{\text{crit}} \to \beta_{\text{crit}}^{\text{MHD}}$.

5.3.4 Mode Transformations and Exceptional Points

As mentioned before, other sets of physical parameters may lead to different scenarios. For example, the KBM may become marginally stable below the threshold. Such a case, using the aforementioned CBC parameters except for $\omega_n = 3$, $\omega_{T\text{i}} = 4$, and $\omega_{T\text{e}} = 6$, can be found in Fig. 5.10. Similarly, an example for the interchange of a KBM with a mode that is stable over the entire β range, leading to marginal stability, is given in Ref. [86]. While an interesting effect in itself, it is more than doubtful, however, that such marginally stable modes can play a significant role in nonlinear simulations.

At least for the present case (as will be shown later), KBMs do not become nonlinearly dominant as long as $\gamma_{\text{TEM}} > \gamma_{\text{KBM}}$; therefore, nonlinear effects do not cause a linearly subdominant more to govern nonlinear transport, at least for the current physical scenario. However, nonlinear interactions of linear modes are possible, making subdominant KBMs more than the subject of academic discussion.

Depending on the physical parameters, the picture can change even more drastically. Generally, one can find so-called exceptional points (see, e.g., Kato [91]) in parameter space; when adjusting parameters continuously to move on a closed loop around such an exceptional point, a mode is transformed into another mode,

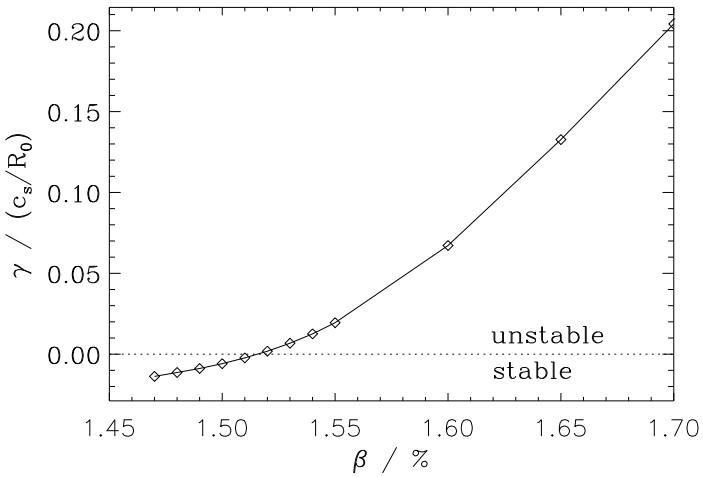

Figure 5.10: Subdominant growth rates of the kinetic ballooning mode for a set of physical parameters differing from the standard set used in this work (as given in the text). Here, one observes a knee below the zero line. For smaller β values, the mode remains marginally stable.

and vice versa. In Fig. 5.11, an example is shown where by adjusting density and temperature gradients, an ITG mode and a TEM are transformed into one another. Similar transformations may occur between all modes that occur in the present case (see Refs. [92] and [29]).
Since following subdominant or even stable modes over a range of parameters can be computationally expensive, it is useful to have a measure of how close a choice of parameters is to an exceptional point. To this end, one can use GENE in the eigenvalue solver mode and then take the eigenvectors of the two modes of interest – which in the context of Vlasov simulations correspond to their respective distribution functions g_1 and g_2; they are available in the `checkpoint` files – and compute their (normalized) scalar product,

$$p = \frac{\|g_1 \cdot g_2\|}{\|g_1\|\|g_2\|} \quad . \tag{5.7}$$

If p is found to be close to one, it indicates near-identicalness of the modes, and thus proximity to an exceptional point, making mode transformations possible.
In Fig. 5.12, an example (with $\epsilon_t = 0.16$ and $\omega_n = 6$) is shown where the KBM is continually transformed into a TEM-like instability. While one may use various methods to determine a critical β value for such a case (e.g., by taking the

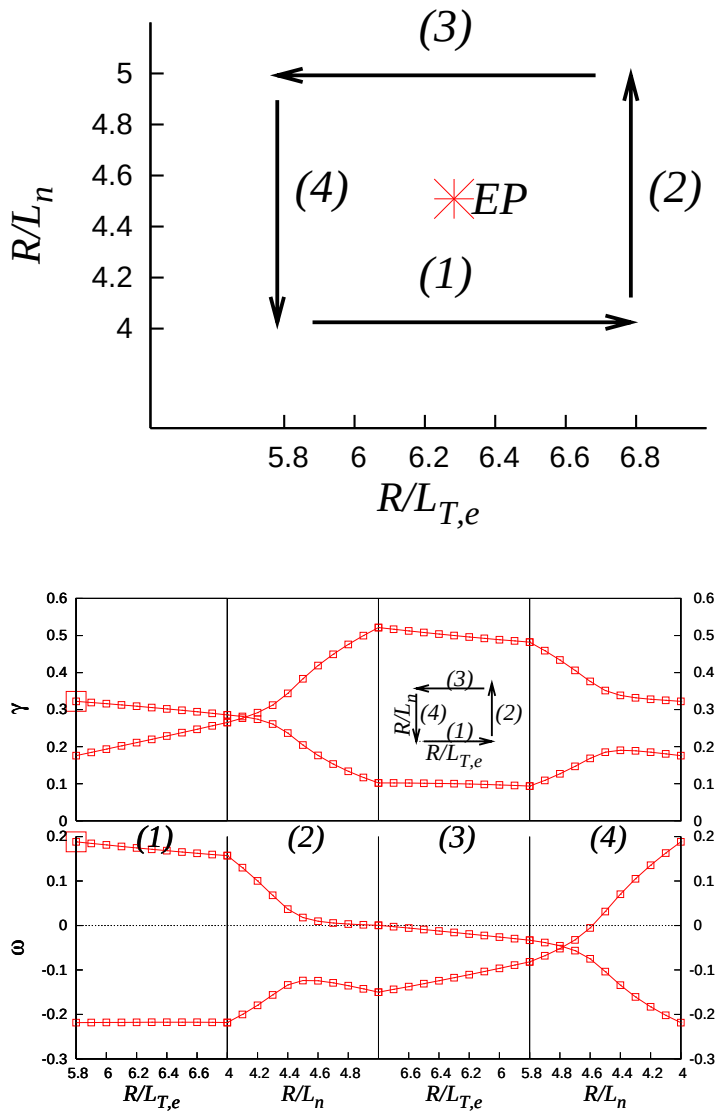

Figure 5.11: Closed parameter space path around an exceptional point (upper graph) and resulting linear growth rates and frequencies (lower graphs). After one cycle, the modes have switched their identity. Source: [29]

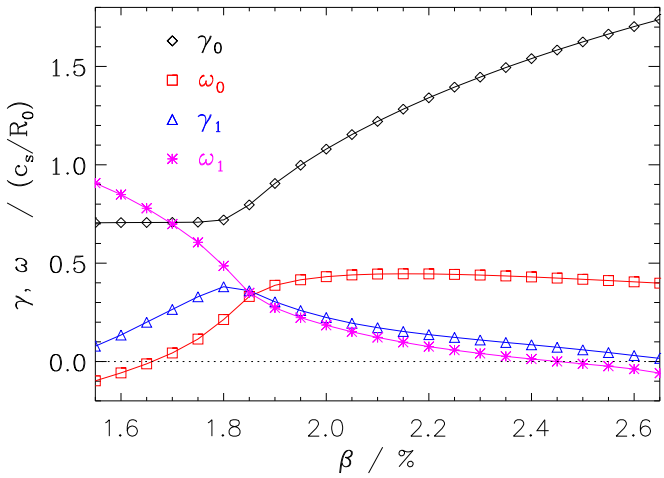

Figure 5.12: Transformation of a KBM into a TEM-like mode. As β is decreased, the KBM frequency ω_0 (red squares) continuously drops to negative levels. Correspondingly, the growth rate γ_0 (black diamonds) stops its descent and becomes constant. This behavior can be understood by taking another mode into account, characterized by γ_1 (blue triangles) and ω_1 (pink stars): originally (i.e., for a smaller density gradient ω_n), the left branch of γ_0 was connected to the right branch of γ_1, and conversely, the KBM-like right branch of γ_0 used to be connected to the left branch of γ_1. The frequencies behave accordingly.

value where the frequency $\omega = 0$), it is obvious that a precise definition of the KBM threshold is not possible. A detailed investigation into the effect of such properties on nonlinear transport and KBM onset would be of interest; however, before embarking on such an endeavor, deepening the general understanding of the nonlinear KBM onset is required. For a more in-depth discussion of mode transformations and exceptional points, Ref. [92] should be consulted.

To summarize the linear investigations, one finds that – at least for physical parameters which are relatively close to the Cyclone Base Case set – the reduction of the linear KBM threshold relative to its MHD counterpart tends to remain below about 20%. Generally, the disappearance of the KBM at lower β can occur in (at least) three different ways: it can turn into a damped mode; it can become marginally stable; or it can transition directly into a different mode (like a TEM or an ITG mode). While these investigations can confine the region of influence of KBMs in linear simulations, they can merely be used as estimates

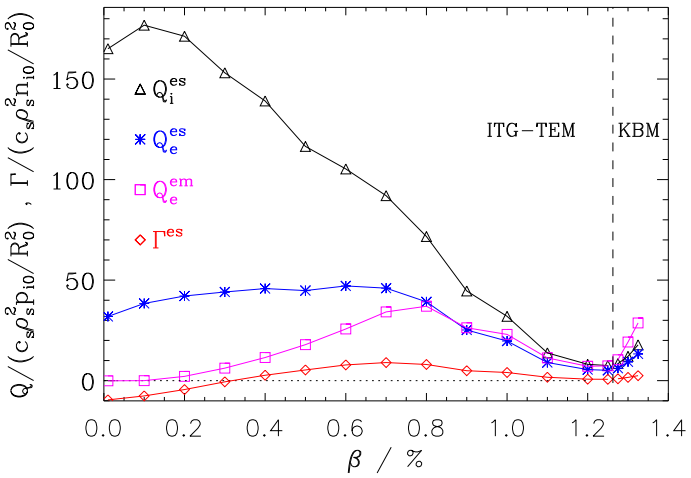

Figure 5.13: Heat and particle transport as a function of β. The values for the ion electromagnetic heat flux and the electromagnetic particle flux are very small in comparison and thus were not included in this figure. The ion electrostatic heat flux partly reflects the behavior of the linear growth rates. However, while a KBM dominant regime can be distinguished, a pure TEM regime is not found.

when going on to turbulent systems. In order to assess the role of KBMs in such environments, nonlinear simulations are called for.

5.4 Nonlinear β Scan

The most important difference between linear and nonlinear resolution requirements is caused by the magnetic field line flutter. The electrons are prone to react violently to perpendicular disturbances of the magnetic field, and therefore, a higher parallel resolution is required for somewhat higher β. In consequence, all nonlinear simulations at $\beta \geq 0.7\%$ that are shown here were done with $N_z = 48$. The perpendicular grid is $N_x = 192$ (positive and negative modes each 96) and $N_{ky} = 24$, with the perpendicular box characterized by $L_y = 125.66$ and $L_x = 101.78$. The parallel diffusion coefficient is modified due to the enhanced requirements of magnetic flutter, and set to $D_z = 8$. Convergence was tested in the ITG dominant regime at $\beta = 0.8\%$.

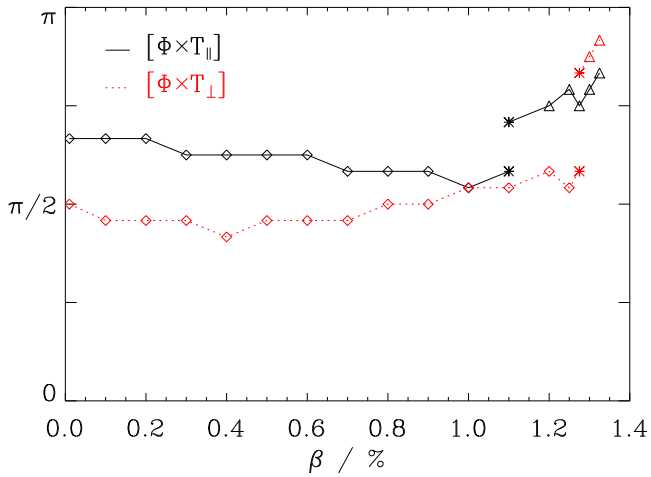

Figure 5.14: Changes of cross-phase relations with increasing β. Solid black lines represent the dominant phases between the electrostatic potential Φ and the parallel ion temperature $T_{\mathrm{i}\parallel}$, whereas dotted red lines represent the dominant phases between Φ and the perpendicular ion temperature $T_{\mathrm{i}\perp}$. Within every regime, phases change only very moderately and continuously (diamonds and triangles), but at two of the characteristic β values, a phase coexistence occurs (stars).

5.4.1 Turbulence Regimes

The nonlinear transport levels over an extended β range are shown in Fig. 5.13. The behavior can be described as follows: first, there is a significant decrease, followed by a flat region, and then a sudden and steep increase. As becomes apparent, even from this plot, there exist at least two distinct turbulence regimes. One is in the low and moderate β range which is dominated by ITG modes or TEMs or both; the second is dominated by KBMs. They are separated by a transitional point at about $\beta = 1.26\%$. Additionally, one finds qualitative changes at $\beta = 0.8\%$ and $\beta = 1.1\%$ – while the electron heat transport (both the electrostatic and the electromagnetic channel), as well as the electrostatic particle flux, are increasing for lower β, they now start to decrease. It shall be noted that the critical KBM value is actually very close to the linearly determined value $\beta_{\mathrm{crit}}^{\mathrm{dom}}$ (for $k_y = 0.2$) at which the KBM growth rate starts to exceed that of the TEM.

Interpreting the other two thresholds represents a greater difficulty. Looking at

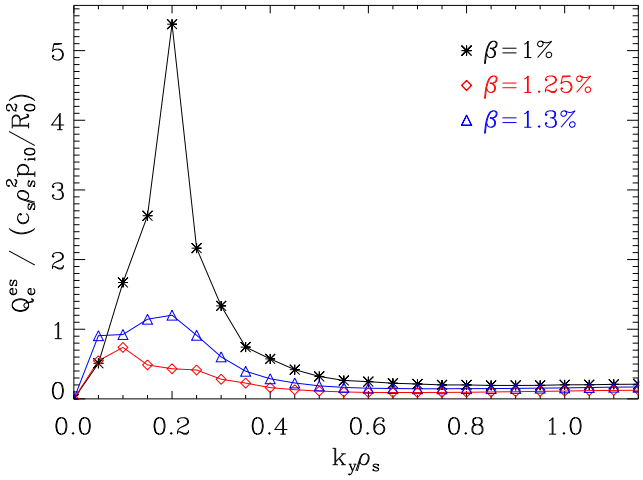

Figure 5.15: Changes in the electrostatic electron transport spectra with increasing β; the ion counterpart shows a very similar behavior. At $\beta = 1.25\%$, the peak shifts slightly to lower k_y while retaining strong transport contributions at $k_y = 0.2$.

the phase relations shown in Fig. 5.14, it can be inferred that at a value of β that roughly corresponds to the linear regime transitions from ITG to TEM and from TEM to KBM, respectively, the nonlinear physics exhibit similar features. Both points are highlighted by changes in the transport spectra, as well – in Fig. 5.15, such spectra are shown for three β values corresponding to the three different linear regimes; one can discern qualitative differences for each of these spectra.

One might thus be led to believe that the nonlinear behavior follows the linear one, including an ITG-TEM transition at roughly the same β. While this picture is also supported by a phase-based frequency analysis that includes all radial connections of the extended ballooning structure (without weighting by amplitude), using Fourier transforms (including only the first radial connections) to determine the nonlinear frequencies yields different results. As can be seen in Fig. 5.16, no negative frequencies occur over the entire β range; there is a frequency shift at $\beta = 0.8\%$, and another at $\beta = 1.2\%$. The second value corresponds to the linear onset of KBMs which dominate the frequency signature while not dominating the transport for $\beta \leq \beta_{\mathrm{crit}}^{\mathrm{dom}}$. The intermediate frequency level at $\omega \approx 1.5$ cannot be motivated by the linear physics, however; additionally, ion electrostatic heat transport exceeds its electron counterpart throughout the β range corresponding

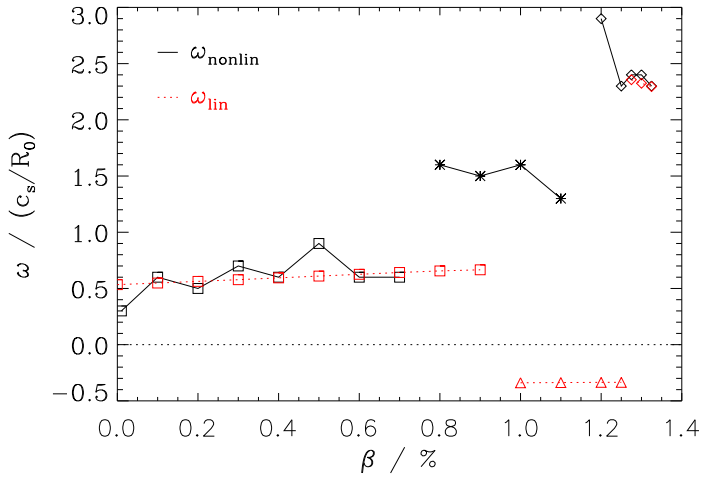

Figure 5.16: Nonlinear frequencies at $k_y = 0.2$ (solid black curves), extracted via (windowed) Fourier transform of the electrostatic potential Φ. The linear frequencies are included for comparison (dotted red curves). Note that the KBM frequencies take over before β reaches the value where the transport is dominated by these modes. Nonlinearly, there is a frequency regime between the ITG and the KBM level (stars) which exists roughly but not exactly at β values that correspond to the TEMs linearly (triangles).

to TEMs linearly, whereas looking at the ratio of the ion to the electron transport in linear simulations, one would expect a much higher electron contribution; this indicates that there is an ion-related process involved in the intermediate regime.

As will be discussed further below, the intermediate range might be caused by nonlinear interactions of the ITG modes with the TEMs; and possibly, magnetic flutter contributes to the change, as well. Consequently, the regime at smaller and moderate β is labeled an ITG-TEM regime. Note that for $\beta < 0.8\%$, one finds pure ITG turbulence. In contrast, all available diagnostics agree very well on the nonlinear KBM onset; its properties can apparently be explained very well by the linear physics – with the exception of the low transport levels at the KBM onset. Those, however, are likely to be attributed the intermediate range and cannot be motivated by the nature of nonlinear KBMs.

In this context, it should be noted that for a few β values in this scan, the simulations are quite numerically challenging. While *all* simulations find saturation, the ones for $\beta = 1.0\%$ and 1.1% (in the ITG-TEM coexistence regime) and for

$\beta = 1.3\%$ and 1.325% (in the KBM regime) display – for the numerical parameters used here – what appears to be a numerical instability in the long-time limit. In these cases, the transport levels would first saturate, and then take off to much larger (by multiple orders of magnitude) values after roughly $(200 - 300)R_0/c_s$, measured from the beginning of the saturation phase. On the other hand, other β values do not seem to be affected. E.g., the $\beta = 1.25\%$ simulation shows no sign of a numerical instability during its full duration of $> 500R_0/c_s$. These difficulties might be related, respectively, to the nonlinear interplay of ITG modes and TEMs (see the discussion below) and to the linear low-k_y behavior of KBMs, but a more detailed analysis (which turns out to be quite involved and is done in the context of the aforementioned electromagnetic benchmark effort) is underway and will be published elsewhere.

As mentioned above, the β value for which the turbulence acquires a clear KBM character is very close to the linear quantity $\beta_{\mathrm{crit}}^{\mathrm{dom}}$ (taking its value at $k_y = 0.2$ which represents both its minimum and the nonlinear transport maximum, and can thus be expected to be the most relevant one compared with those at other k_y) that describes the point at which the KBM growth rate exceeds that of the TEM. In other words, while KBMs already contribute within part of the ITG-TEM regime (where they are already linearly unstable but still subdominant), they only become dominant nonlinearly once the linear KBM dominance threshold is crossed. This means that the exact onset point for linear KBMs seems to be of limited practical relevance if other modes are clearly dominant there. Although deviations from this rule of thumb can be envisioned for different physical scenarios, one is led to think that KBMs are likely to dominate nonlinearly wherever they dominate linearly (in the low-k_y part of the spectrum where the transport usually peaks), and vice versa. This finding further narrows the window of KBM activity; not only do (marginally) stable KBMs not contribute, but even subdominant KBMs seem to have very limited effect on the turbulence. In the present case, the effective onset point is decreased only by less than 5% compared with the MHD threshold. How generic this finding is remains to be investigated, but the basic trend (a very moderate linear reduction which is not extended by nonlinear effects) may be expected to hold.

After this discussion of regime transitions, possible explanations for the low transport at moderate and high β will be presented.

5.4.2 Transport Levels

It is known that nonlinear transport levels often tend to follow the respective linear growth rates. While here, such a model would correctly predict some general tendencies (declining ITG transport, constant intermediate range, KBM threshold), it can not explain some of the other features in Fig. 5.13. Most prominently, the high-β end of the TEM-ITG regime shows saturation levels that are lower than the electrostatic ITG level by a factor of about 20, which exceeds the respective decrease of the linear growth rate by an order of magnitude; and the previously mentioned knee in the electron and particle fluxes at $\beta = 0.8\%$ is not mirrored in any form by the linear simulations, either, which might be due to the same cause. In the following, possible explanations for the low transport levels are provided.

TEM Transport Model

In a first step, the regime around $\beta \sim 1.2\%$ is focused on in which TEMs dominate linearly. TEM-induced transport has been estimated successfully before by means of a transport model which is described in detail in Refs. [93, 94]. Here, a mixing length estimate is used for the thermal diffusivity,

$$\chi_\mathrm{e}^\mathrm{model} \sim \max_{k_y} \left(\frac{\gamma}{\langle k_\perp^2 \rangle} \right) \quad , \tag{5.8}$$

with $k_\perp^2 = k_y^2(1 + \hat{s}^2\theta^2)$ for $k_x = 0$ which is the case for typical TEM streamers. Here, $\langle \ldots \rangle$ denotes averaging according to the prescription

$$\langle f(\theta) \rangle \equiv \frac{\int \|\Phi\|^2 f(\theta) \mathrm{d}\theta}{\int \|\Phi\|^2 \mathrm{d}\theta} \tag{5.9}$$

for a θ-dependent function $f(\theta)$; note that the electrostatic potential Φ is used to model the parallel structure and needs to be taken at the k_y mode under consideration. The resulting heat flux estimate reads

$$Q_\mathrm{e}^\mathrm{model} = \mathcal{C} \omega_{T\mathrm{e}} \max_{k_y} \left(\frac{\gamma}{\langle k_\perp^2 \rangle} \right) \quad , \tag{5.10}$$

where $\mathcal{C}$ is a dimensionless scaling parameter that can be gauged via a single nonlinear reference value for Q_e. To arrive at estimates for the other transport channels (e.g., Q_i), one can make use of quasilinear ratios of those quantities to Q_e at the k_y corresponding to the maximum calculated according to Eq. (5.10). While in the present case, a nonlinear reference value is not available, one may infer many interesting transport properties from linear simulations alone.

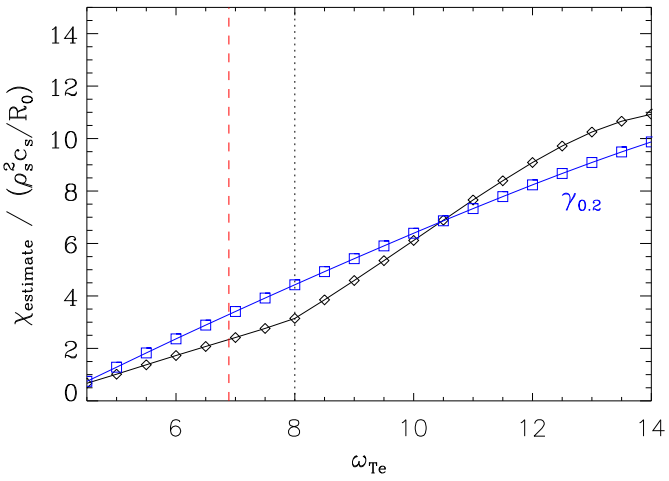

Figure 5.17: Quasilinear TEM transport model. Shown is the predicted scaling of the thermal diffusivity $\chi_{\text{estimate}} = (\gamma/\langle k_\perp^2 \rangle)_{\max}$ with the electron temperature gradient. $\gamma_{0.2}$ – which is the linear growth rate at $k_y = 0.2$, rescaled to arbitrary units – is included for comparison. At $\omega_{Te} = 8.0$ (black dotted line), a knee in the predicted transport is observed where the scaling changes; at this point, the ratio $\chi_{\text{estimate}}/\gamma_{0.2}$ is especially small. The value $\omega_{Te} = 6.89$ (red dashed line) used in the nonlinear simulations lies close to that knee.

In Fig. 5.17, an ω_{Te} scan is presented which is based on this transport model, along with the linear growth rate $\gamma_{0.2}$ for $k_y = 0.2$. One can distinguish two regions, one with slowly and one with more strongly increasing transport, which are separated by a knee at $\omega_e = 8$. Consequently, the values at and just below the knee have the lowest ratio of $\gamma_{0.2}/\chi_e^{\text{model}}$. This means that at these gradients, one is most likely to overestimate transport levels by drawing direct conclusions from the linear growth rate with respect to nonlinear transport levels.

Clearly, the value used for the simulations shown in Fig. 5.13 is in the low transport region just below the knee. While due to the lack of a reference value, there is no absolute meaning to χ_e^{model}, it serves as an indication that one might indeed find a lower saturation level at $\beta \sim 1.2\%$ than one would expect from the behavior of γ (as shown in Fig. 5.6). However, while this effect might contribute to lowering the transport levels, there is no indication that it would do so by an order of magnitude; in the following, more processes are investigated that might be of importance here.

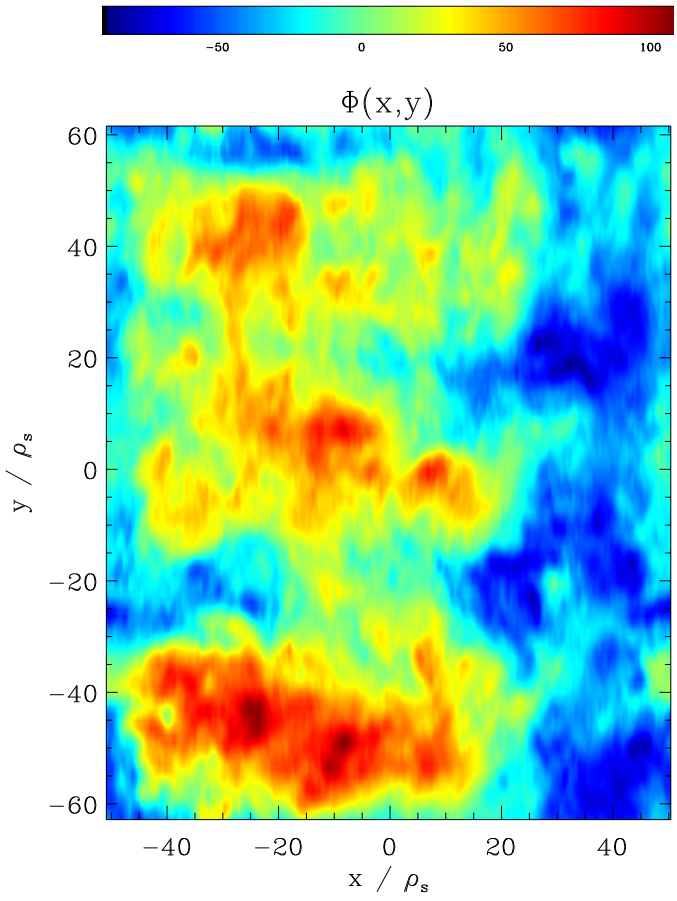

Figure 5.18: Contours of the electrostatic potential Φ in the perpendicular plane. Both a zonal flow structure and an overlaying $k_y \approx 0.15$ pattern are clearly visible. The β value for this data is 0.6%.

Zonal Flows

Zonal flows can play a significant role in suppressing heat and particle transport (see Diamond et al. [95] for a review on zonal flows). In fact, zonal flows are known to be an important saturation mechanism for plasma microturbulence; however, one cannot deduce only from the presence of these flows that they have a strong impact on the transport, as is shown, e.g., in Ref. [29].

For the entire β range, an inspection of contour plots shows that zonal flows are strongly excited (see Fig. 5.18 for an example), becoming even more pronounced as β is increased. A quantitative measure of the impact of zonal flows is the

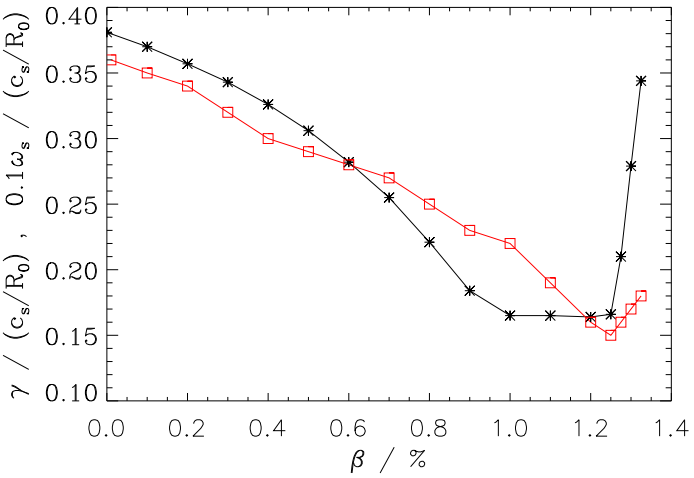

Figure 5.19: Comparison of the shearing rate ω_s (red squares; rescaled) and the linear growth rate γ (black stars). The requirement for zonal flow based transport suppression, $\omega_s \gg \gamma$, is fulfilled marginally at every point in the ITG-TEM regime. At $\beta = 1.0\%$, the ratio ω_s/γ peaks, indicating maximal influence of zonal flows at that point.

shearing rate,

$$\omega_s = \frac{\mathrm{d}^2\Phi_{\mathrm{zon}}}{\mathrm{d}x^2} \quad , \tag{5.11}$$

where Φ_{zon} is the zonal component of the electrostatic potential. Due to finite-frequency corrections [96], the shearing rate needs to be much larger than the linear growth rate, $\omega_s \gg \gamma$, for zonal flows to be able to act as the dominant nonlinear saturation mechanism, controlling the transport levels. As can be seen in Fig. 5.19, this necessary condition seems to be (marginally) fulfilled across the entire β range, with $\omega_s/\gamma \sim 10$. Moreover, for $\beta \leq 1.0\%$, ω_s/γ is steadily increasing. This finding suggests that zonal flows may contribute to the strong decrease of the transport level with increasing β. It shall be noted that here, the finite frequency corrections as described in Ref. [96] are not applied, and instead a simplified order-of-magnitude rule is used, motivated by results published in Ref. [97].

In order to test this hypothesis, some simulations were repeated, removing the zonal component of the electrostatic potential and looking at the impact of this modification on the transport levels. The such altered simulations at $\beta = 0.1\%$ and $\beta = 0.6\%$ yielded no significant increase in the electrostatic heat flux (while

effectively suppressing the electromagnetic contribution), indicating that for the lower-β range of the ITG-TEM regime, zonal flows contribute little to the drop in the turbulent transport with increasing β. However, at $\beta = 1.25\%$, removing the zonal potential results in an increase especially of the ion but also the electron electrostatic transport levels by factors of ~ 3 and ~ 2, respectively. The electron electromagnetic level drops to very low levels, much like in the low β cases. This indicates that at higher β in the ITG-TEM regime, zonal flows become a major contributor in suppressing turbulent transport. However, the caveat remains that removing the zonal component of the potential is a severe and unphysical modification, and results produced that way should be interpreted with great care. For instance, the above factors of ~ 3 and ~ 2 likely cannot be understood as a direct quantitative measurement of the zonal flow suppression effect; this is corroborated by the fact that transport levels drop off continuously and not suddenly over the β range described here.
As a result, the low levels of high-β ITG-TEM transport may in part be explained by the effect of zonal flows; however, the latter cannot account for the full magnitude of the reduction.

Zonal Fields

Analogously, one can measure the effective shear due to magnetic field fluctuations (see, e.g., Holland and Diamond [60]). Following Jenko and Kendl [98], the magnetic shear fluctuation due to zonal fields is computed,

$$\tilde{s} = q_0 \frac{R_0}{B_{\mathrm{ref}}} \frac{\mathrm{d}B_y}{\mathrm{d}x} \quad . \tag{5.12}$$

The results can be found in Fig. 5.20. Note that this effect relies on finite k_x modes of the y component of the magnetic field fluctuations; in Fig. 5.21, this component is shown for $\beta = 0.6\%$, where clearly, vertically elongated structures are visible, corresponding to contributions of values of $k_x \neq 0$.
At $\beta = 0.8\%$, corresponding to its maximum, $\tilde{s}/\hat{s} \approx 15\%$, making $\tilde{s}$ a non-negligible quantity. Since this maximum coincides with a qualitative change in the nonlinear transport, it might follow that the nonlinear frequency shift at that value is in part due to the magnetic shear fluctuations. To investigate how the shear fluctuations due to zonal fields may act back on the linear physics, linear simulations (with $k_y = 0.2$) were performed with a modified shear $\hat{s} = 0.786 \pm 0.15$. However, the results show only small frequency modifications: $\omega = 0.627$ for $\hat{s} = 0.636$ and $\omega = 0.694$ for $\hat{s} = 0.936$, compared with $\omega = 0.656$ for the original case with $\hat{s} = 0.786$. Therefore, this effect cannot cause the frequencies

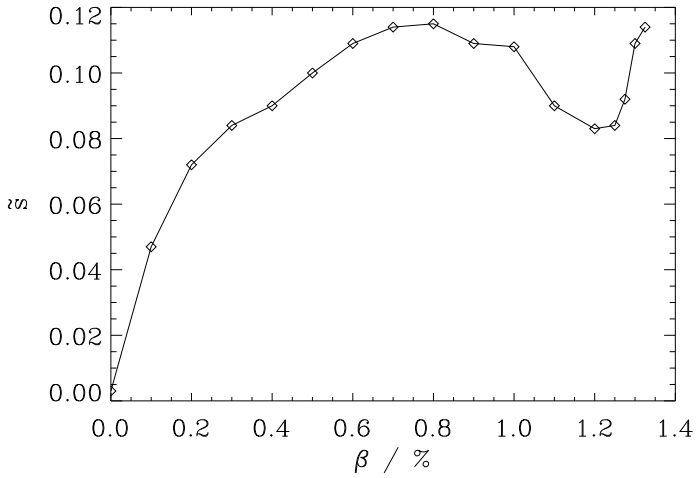

Figure 5.20: Shear fluctuations caused by perturbations of the magnetic field as a function of β. Note that while $\tilde{s}$ always remains much smaller than the global shear $\hat{s} = 0.786$, it still makes for a significant modification. However, as is explained in the text, the influence of these fluctuations on the transport levels is doubtful.

in the nonlinear ITG-TEM regime. Also, these simulations indicate that in the present case, zonal fields may be relatively strong, but still too weak to act as the dominant saturation mechanism.

Nonlinear Mode Interactions

The mechanisms portrayed above may all contribute to the nonlinear reduction of transport as β approaches the ballooning threshold. However, even taken together, they are not sufficient to explain the magnitude of the reduction. One more effect that has the ability to bridge this gap between the linear and the nonlinear results are nonlinear mode interactions of the TEMs with ITG modes, and possibly KBMs, which will be discussed here.

Linear modes can compete nonlinearly and thus cancel each other out to a significant degree, reducing the turbulent transport levels. In Fig. 5.14, coexistence of phase relations at the regime transitions was found; and in Fig. 5.15, the regime signature transport peaks become vague at β values close to the linear ITG-TEM transition. This coexistence implies interaction and possibly competition.

Merz [29] finds that interaction of TEM with ITG turbulence (in the context of a

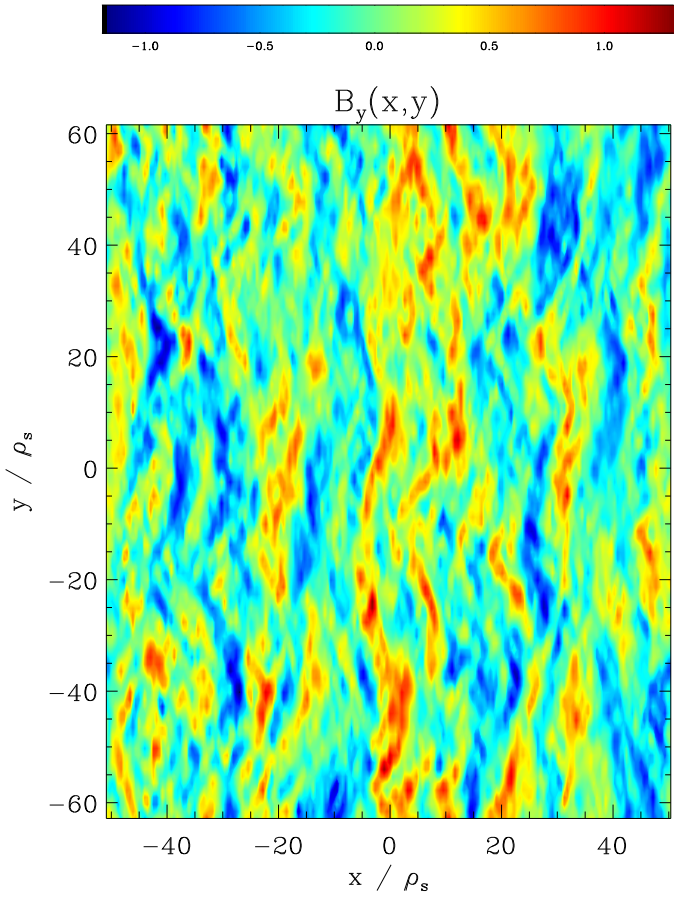

Figure 5.21: B_y fluctuations at $\beta = 0.6\%$. One can distinguish structures which are elongated in the y direction, a requirement for magnetic shear fluctuations to play a strong role in nonlinear simulations.

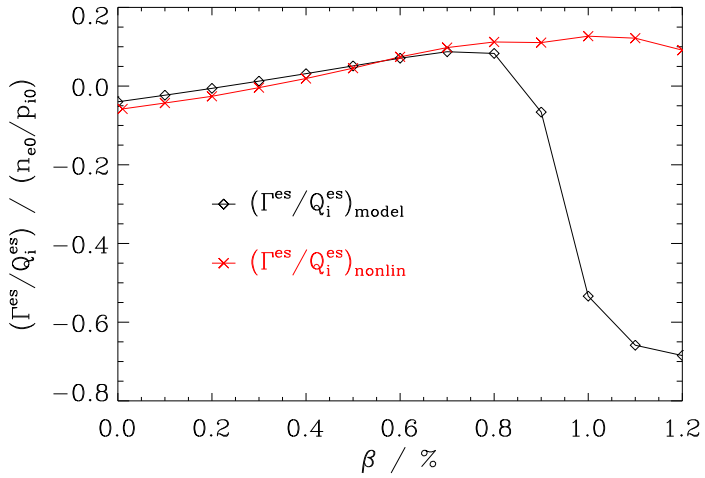

Figure 5.22: β dependence of the ratio of the electrostatic particle transport to the ion electrostatic heat transport, as predicted by the model (black diamonds) and as measured in the nonlinear simulations (red crosses). For low β values, quasilinear and nonlinear results agree, but as the TEMs take over linearly, the corresponding jump in the quasilinear curve is not found in the nonlinear data.

scan over the ion temperature gradient) leads to a reduction of the electron heat flux by a factor ~ 5, while the particle flux vanishes nearly completely. The same model for TEM transport which was described above was applied, and similarly to the present case, it was unable to explain the magnitude of the reduction. Another quasilinear model was then constructed which predicts nonlinear ratios of pairs of transport quantities from linear results. To test the validity of this model for the present case, one can look at the ratio of the electrostatic components of the particle and the ion heat transport, $R^{\Gamma,\mathrm{Qi}} = \Gamma^{\mathrm{es}}/Q_{\mathrm{i}}^{\mathrm{es}}$. According to the model,

$$(R^{\Gamma,\mathrm{Qi}}_{\mathrm{interact}})_{\mathrm{model}} = \frac{\gamma^{10}_{\mathrm{ITG}} R^{\Gamma,\mathrm{Qi}}_{\mathrm{ITG,lin}} + \gamma^{10}_{\mathrm{TEM}} R^{\Gamma,\mathrm{Qi}}_{\mathrm{TEM,lin}}}{\gamma^{10}_{\mathrm{ITG}} + \gamma^{10}_{\mathrm{TEM}}} \quad . \tag{5.13}$$

A comparison of the model with the nonlinear results yields good agreement up to $\beta \sim 0.8\%$, where the system is still clearly dominated by ITG turbulence. However, a strong jump of $(R^{\Gamma,\mathrm{Qi}}_{\mathrm{interact}})_{\mathrm{model}}$ where TEMs become dominant linearly is not found in the respective nonlinear curve, as can be seen in Fig. 5.22. Therefore, the model appears to overestimate the impact of the TEMs for $\beta > 0.8\%$: even while some of the aforementioned features point at a TEM contribution to the turbulence, these modes cannot account for the observed behavior, neither

when looked at separately or in the context of this transport model; it would thus be desirable to turn to a more refined model at a later point.
It remains to be seen to what extent nonlinear mode interactions can be employed to improve confinement in fusion experiments; however, their potential to reduce both heat and particle transport levels makes them an interesting candidate for advanced confinement scenarios.

5.5 Chapter Summary

In the present chapter, finite-β effects on linear modes and nonlinear turbulence have been presented in the context of CBC parameters. Linearly, depending on the β value, ITG modes, TEMs, or KBMs dominate; particular focus is put on the KBM threshold – besides the KBM onset and its parameter dependence, the β threshold for KBM dominance over TEMs is discussed. Nonlinearly, transport levels are presented for a significantly larger range than what was achieved in previous work. Moreover, as β approaches the linear KBM threshold, transport levels are reduced strongly compared to simple linearly motivated expectations. Multiple contributing factors for this effect are discussed, with the quantitatively most important being nonlinear mode interactions.

Chapter 6

Electromagnetic TEM Turbulence

Following the CBC investigation of the previous chapter, a different parameter set is presented, corresponding to density gradient driven TEMs. Similar analyses are performed: linearly, the KBM onset shows somewhat different behavior than in the CBC, and nonlinearly, zonal flows are found to explain the development of the transport with increasing β over a wide range.

6.1 The Parameter Set

Starting from CBC parameters, the density and temperature gradients are modified to move into a TEM dominated regime. Most prominently, the ion temperature gradient is set below the ITG threshold. In order to retain the temperature ratio $T_\mathrm{e}/T_\mathrm{i} = 1$ without exciting ETG modes throughout a significant k_y range in the process, the electron temperature gradient has to be lowered, as well. The resulting gradients are

$$\omega_{T\mathrm{i}} = 2 \quad , \quad \omega_{T\mathrm{e}} = 4 \quad , \quad \omega_n = 3 \quad . \tag{6.1}$$

All other physical parameters are chosen as in the aforementioned CBC.
The physical scales of TEM turbulence are similar to those of ITG turbulence, with linear growth rates peaking near $k_y = 0.4$. This is connected to the fact that the general mechanism of ITG modes and TEMs is the same; only for the latter, electrons on banana orbits take the role that the ions had for the former. In TEM simulations, the passing electrons tend to behave more or less adiabatically. However, while zonal flows are the main saturation mechanism for ITG turbulence, this does not necessarily apply to TEM turbulence which is often

characterized by radial streamer structures. Further details on nonlinear TEM saturation have been published by Merz and Jenko [99].
In terms of the numerical settings, the parallel diffusion parameter ϵ was increased compared with the CBC to a value of 12. For the linear simulations, resolutions similar to those mentioned in Ch. 5 were used.

6.2 Linear Behavior

6.2.1 Linear β Scan

Consistently with the observations reported in Ch. 5, TEM growth rates undergo very little change as β is increased (with slowly declining values of γ; the frequencies experience even less change), as is shown in Fig. 6.1. This is due to the importance of the trapped particles, which do not lead to large magnetic field fluctuations. However, as the KBM limit is crossed, the ballooning modes grow quickly, as is to be expected. Clearly, the KBMs appear first at lower k_y before they reach higher values. Below, an investigation into the KBM onset is performed.

6.2.2 The KBM Threshold

While the general picture of the KBM onset – and their growth rates exceeding those of the TEMs – in Fig. 6.1 shows little variation compared to what was observed for the CBC, there is one fundamental difference: ITG modes and KBMs tend to have their maximal growth rate at more or less the same k_y, but the corresponding TEM value is measurably higher. This means that – due to the absence of ITG modes in the present case – unlike in the CBC, KBMs may dominate at lower k_y long before they overtake the TEMs in the value range where the nonlinear transport peaks. In fact, this is exactly what is observed when the k_y dependence of the KBM onset is plotted (see Fig. 6.2). Moreover, it is to be expected from these results that, as the MHD limit $\beta_{\mathrm{crit}}^{\mathrm{MHD}} = 2.03\%$ is approached with $k_y \to 0$, the KBM threshold reaches its lowest value. Consequently, KBMs may play a prominent role nonlinearly slightly above β_{crit} since nonlinear transport usually dominates at k_y values smaller than those where the linear growth rate reaches its maximum.
The above finding is consistent with that of the previous chapter which shows a strong ion temperature gradient dependence of the KBM threshold – in Fig. 5.9, lowering $\omega_{T\mathrm{i}}$ is found to shift β_{crit} to higher values. The onset value for the

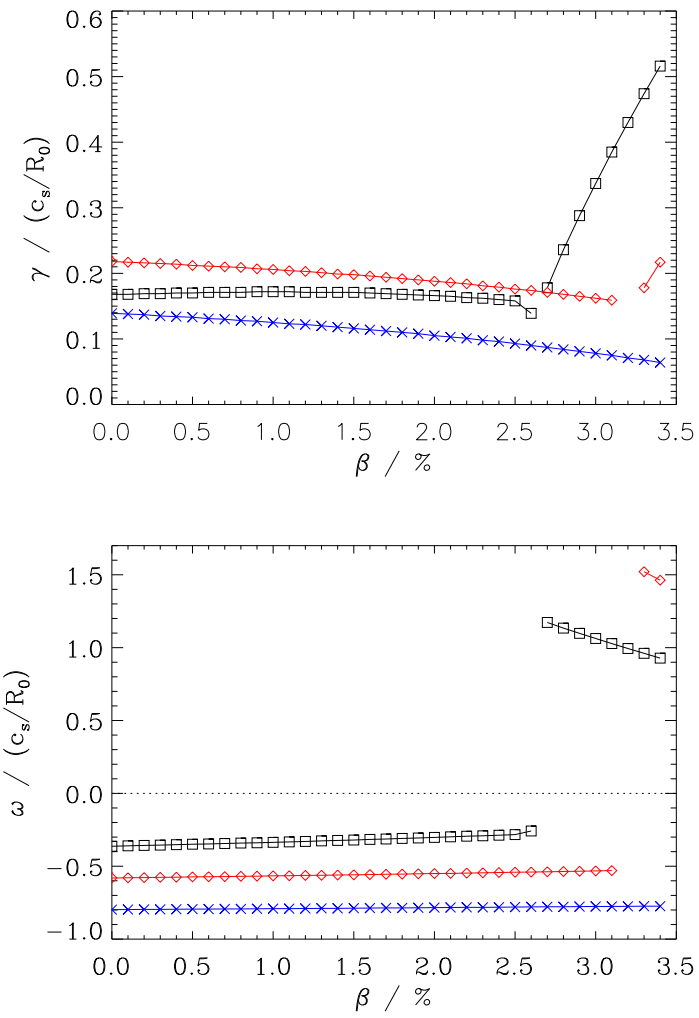

Figure 6.1: Linear growth rate (upper graph) and frequency (lower graph) dependencies on β for density gradient driven TEMs at k_y values of 0.2 (black squares), 0.4 (red diamonds), and 0.6 (blue crosses). As expected, the $k_y = 0.2$ case is the first where KBMs become dominant.

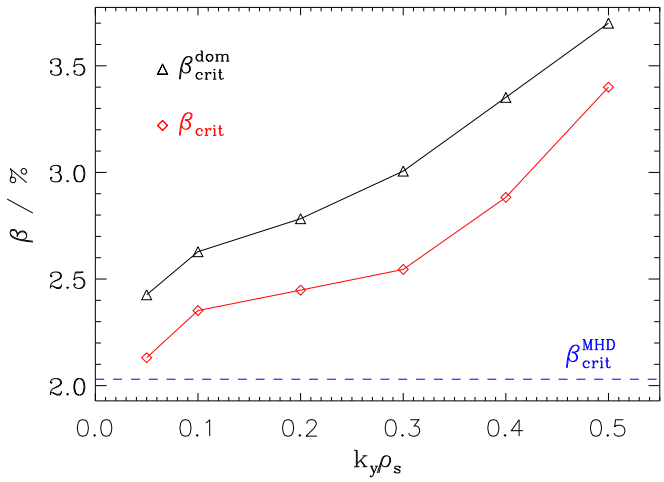

Figure 6.2: Values of the critical β for the onset of KBMs (red diamonds) and their dominance over TEMs (black triangles), respectively, for a range of k_y. The MHD prediction is shown for comparison (blue dashed line). Note that no extrapolation was used for the onset values, and instead, subdominant mode analysis was performed. Slight deviations from Fig. 6.1 are due to the higher resolution used here.

present case, $\omega_{T\mathrm{i}} = 2$, is consistent both qualitatively and quantitatively with this result.

6.3 Nonlinear Results

Nonlinearly, convergence tests were performed, and as a consequence, the resolutions were chosen identical to those for the CBC with the exception of two settings: N_z was set to 48 even for low β values, and a box with increased $L_y = 251.3$ (corresponding to a smallest resolved k_y of 0.025) was used to reduce unphysical finite box influences on the simulations – nonlinear fluxes were found to peak at relatively low k_y, substantiating this choice.

6.3.1 Nonlinear β Scan

Nonlinear transport levels are reported in Fig. 6.3; the electromagnetic particle and ion heat fluxes are not included because of their small relative contribution. Much like in the linear case, the electrostatic flux levels do not react very strongly

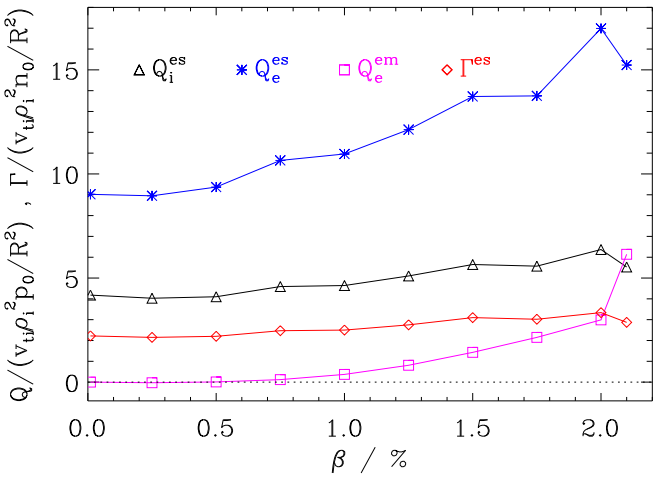

Figure 6.3: β dependence of heat and particle transport levels. For a large range of values, the transport is TEM dominated; at $\beta = 2.1\%$, the picture is less clear, however, as is explained in the text.

to variations of β for the largest part of the scan. However, instead of the slight decrease in the linear growth rates γ, as shown above, an increase can be seen in the nonlinear levels. Possible causes are discussed below.
At values above $\beta = 2.1\%$, saturation could not be achieved. Whether this is due to KBM activity is speculative; the issue is being investigated, and possibly, findings from the aforementioned electromagnetic benchmark exercise concerning stability issues may also apply here.

6.3.2 Transport Levels

Similarly to Ch. 5, a discussion of the transport levels is presented. In the present case of TEM turbulence, the picture is less complicated, however. Frequency analyses agree for a wide range of β values, and the results are very similar to the respective linear values at the k_y corresponding the turbulent transport peaks. Only at $\beta = 2.1\%$ does the picture change: in addition to the (dominant) TEM frequencies, small contributions at KBM frequencies arise; this coincides with a qualitative change in the transport levels. However, this change does not come with a reversal of the dominant species: the electron transport still exceeds the ion transport. The fact that these features occur at values measurably below most of the linear $\beta_{\mathrm{crit}}^{\mathrm{dom}}$ values shown in Fig. 6.2, as well as just barely above

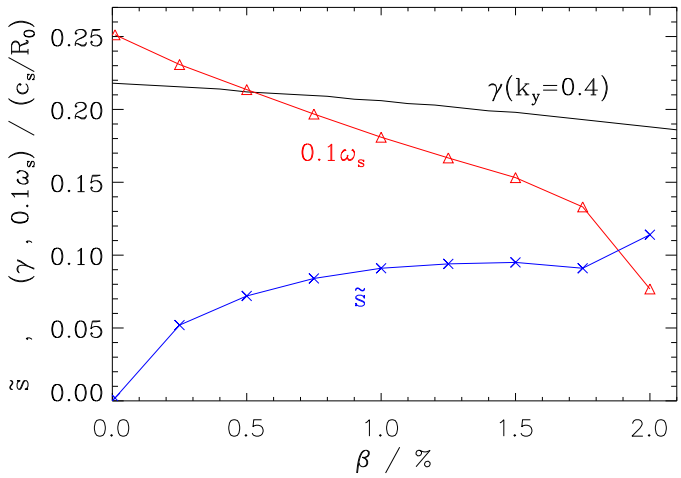

Figure 6.4: Zonal flow and zonal field activity in nonlinear TEM simulations. The shearing rate (rescaled; red triangles) exceeds the linear growth rate (at $k_y = 0.4$, black curve) by more than a factor of 10 in the beginning; this value drops to less than 5 for $\beta = 2.0\%$, signaling decreasing influence on zonal flows. For completeness, the shear fluctuations are included (blue crosses), but their magnitude is too small to constitute a significant effect.

the MHD limit, is not necessarily a sign that the prescription for nonlinear KBM dominance (i.e., KBMs dominate nonlinearly where they dominate linearly; as derived for the CBC) does not hold. For the TEM scenario, the altered spectral structure presented in Fig. 6.2 has to be considered – KBMs may start to influence the transport at the lowest k_y, which is where their threshold is at its lowest.

The increase of transport for values below that point can be explained well by zonal flow activity. Fig. 6.4 shows the (rescaled) shearing rate ω_s in comparison with the linear growth rate for $k_y = 0.4$ which corresponds to a typical TEM value. Recalling that the condition for significant nonlinear zonal flow contributions is $\omega_s \sim 10\gamma$ (see Ch. 5), this illustrates that zonal flows might contribute strongly at low β, with their influence being diminished as β is increased, with little importance at high β values.

This picture is corroborated by x-y contours of the electrostatic potential, which are shown in Fig. 6.5. While for $\beta = 0.01\%$, a zonal flow can be recognized to be competing with radially elongated structures, streamers dominate in the $\beta = 1.75\%$ case.

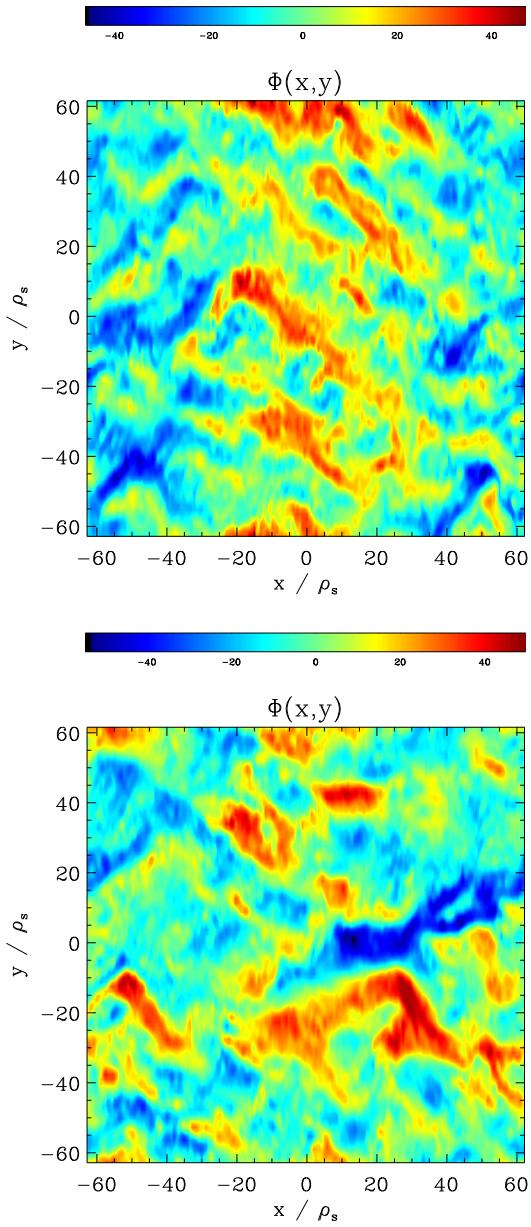

Figure 6.5: Contours of the electrostatic potential Φ in the perpendicular plane. Above, a typical $\beta = 0.01\%$ case is shown, where radial structures are influenced by zonal flow activity. The plot below is taken from a simulation with $\beta = 1.75\%$; clearly, the zonal flow activity has decreased, resulting in stronger streamer-like structures.

Recent studies of TEM turbulence by Lang et al. [100] are in good agreement with the above findings; they show that – in the electrostatic limit – for low $\omega_{T\mathrm{e}}$ and $T_\mathrm{i} \sim T_\mathrm{e}$, significant influence of zonal flows is to be expected, suppressing the transport by a factor > 2. The present results add another dimension to their parameter space, with β suppressing zonal flow activity. It is to be expected, however, that this finding is specific to TEM turbulence, as an opposite effect was found for the ITG turbulence investigated in Ch. 5.

6.4 Chapter Summary

In this chapter, electromagnetic aspects of density gradient driven TEM turbulence were studied. The linear KBM onset shows different behavior – which is likely due to the low ion temperature gradient – in that the MHD limit is exceeded by the kinetic threshold throughout the entire k_y range. This seems to have an effect on the nonlinear transport levels, where a KBM contribution is found just above the MHD threshold. The β scaling of the electrostatic transport levels is characterized by only mild changes. However, unlike the slowly declining linear growth rate, one observes increasing transport nonlinearly. This is explained by a decreasing shearing rate, reducing the influence of zonal flows with growing β.

Chapter 7

Properties of Magnetic Turbulence

After the studies on electromagnetic simulations presented in the last two chapters, additional properties of those simulations are discussed. First, a test particle based model to describe the magnetic transport is given, and its applicability to the simulations is tested. Then, additional properties of the electromagnetic fields are investigated, namely the altered magnetic field structure and fast ion diffusivity in those fields. Last, the effects of realistic geometry on finite-β simulations are examined briefly.

7.1 A Model for the Magnetic Transport

One important question in the context of electromagnetic turbulence simulations is the role of magnetic transport. By this expression, one refers to the contributions to the overall cross-field transport induced by (radial) magnetic field fluctuations. As is well known, the transport channel which is most affected by this process is the electron heat flux Q_e. Its electromagnetic component Q_e^em, due to efficient parallel heat conduction along radially perturbed field lines, is plotted for the ITG regime of the CBC parameter set studied in Ch. 5 – as a function of β – in Fig. 7.1. Both the actual values from nonlinear simulations and quasilinear estimates are shown, normalized to the electrostatic electron heat flux Q_e^es.
Surprisingly, the linear and nonlinear curves deviate substantially from one another. To good approximation, they scale like $Q_\mathrm{e}^\mathrm{em} \propto \beta$ and $Q_\mathrm{e}^\mathrm{em} \propto \beta^2$, respectively, assuming Q_e^es has no significant β dependence. This assumption can be validated by looking at Fig. 5.13. The same findings apply to the transport values reported by Candy [82] which are shown in Fig. 5.5. It is thus desirable to

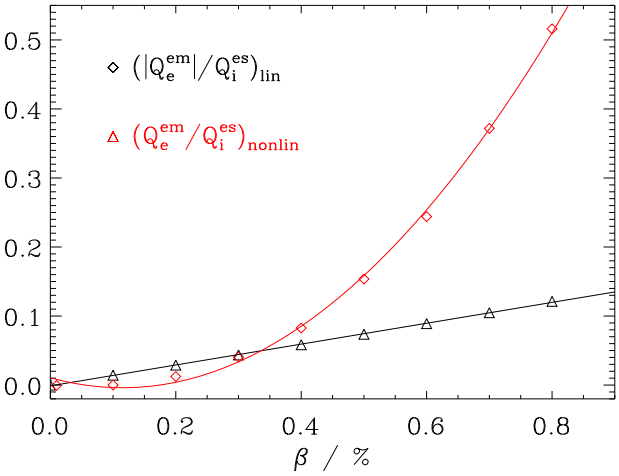

Figure 7.1: Linear and nonlinear scaling of the CBC electron magnetic transport with β: the linear values (black triangles) can be fitted excellently by a straight line, the nonlinear values (red diamonds) by a quadratic function, as shown here. This behavior is reproduced by the transport model.

achieve some theoretical understanding as to why linear estimates and nonlinear results differ this significantly.

7.1.1 The Rechester-Rosenbluth Model

In order to understand these results, use is made of a simple model describing test particle transport along perturbed field lines. Formulated in the present form by Jenko and Dorland [59], it goes back to work done by Rechester and Rosenbluth [101]. The model is based on the ansatz

$$Q_{\mathrm{e}}^{\mathrm{em}} = \frac{\langle \tilde{q}_{\mathrm{e}\parallel} \tilde{B}_x \rangle}{B_{\mathrm{ref}}} \quad , \tag{7.1}$$

with the parallel electron conductivity

$$\tilde{q}_{\mathrm{e}\parallel} = -n_{\mathrm{e}0} \chi_{\mathrm{e}\parallel} \tilde{\mathbf{b}} \cdot \nabla T_{\mathrm{e}\parallel} \quad . \tag{7.2}$$

The gradient can be expanded, yielding

$$\tilde{q}_{\mathrm{e}\parallel} = -n_{\mathrm{e}0} \chi_{\mathrm{e}\parallel} \left(\frac{\mathrm{d}\tilde{T}_{\mathrm{e}\parallel}}{\mathrm{d}z} + \frac{\tilde{B}_x}{B_{\mathrm{ref}}} \frac{\mathrm{d}\tilde{T}_{\mathrm{e}\parallel}}{\mathrm{d}x} + \frac{\tilde{B}_x}{B_{\mathrm{ref}}} \frac{\mathrm{d}T_{\mathrm{e}0}}{\mathrm{d}x} \right) \quad . \tag{7.3}$$

Here, $\tilde{B}_x$ is the radial component of the magnetic field fluctuations, while $\tilde{T}_{\mathrm{e}\|}$ corresponds to parallel electron temperature fluctuations. For convenience, fluctuating quantities are marked with a tilde. The three terms in the brackets describe, collectively, the parallel temperature gradient along perturbed magnetic field lines. For the following discussion, they are labeled $\mathcal{T}_1$, $\mathcal{T}_2$, and $\mathcal{T}_3$, respectively.

This leaves one to determine the parallel diffusivity, $\chi_{\mathrm{e}\|}$. For a sheared slab magnetic field geometry, this quantity was calculated (see Chang and Callen [102]) to be

$$\chi_{\mathrm{e}\|} \approx \frac{1}{k_\|} \left(\frac{T_\mathrm{e}}{m_\mathrm{e}}\right)^{1/2} \sim q_0 R_0 \left(\frac{T_\mathrm{e}}{m_\mathrm{e}}\right)^{1/2} \tag{7.4}$$

in the adiabatic limit. While technically, there is no quantity $k_\|$ for radially extended modes in a sheared magnetic field (due to the quasi-periodic boundary conditions), one can still use this expression as an approximation. Additionally, this result emphasizes that the electromagnetic ion heat flux must be very small, as illustrated by the mass in the denominator.

7.1.2 Phase Relations and β Scaling

One can interpret the findings shown in Fig. 7.1 by analyzing the CBC GENE data with respect to phase relations between pairs of fluctuating quantities entering in the above model.

For linear simulations (see Fig. 7.2), the nonlinear term $\mathcal{T}_2$ vanishes. At the same time, $\tilde{T}_{\mathrm{e}\|}$ and $\tilde{q}_{\mathrm{e}\|}$ have a phase relation of $\sim -\pi/4$, whereas $\tilde{B}_x$ and $\tilde{q}_{\mathrm{e}\|}$ are out of phase. Consequently, $\mathcal{T}_1 \gg \mathcal{T}_3$. With $\tilde{B}_x/B_{\mathrm{ref}} \propto \beta$, one thus obtains the prediction

$$\frac{Q_\mathrm{e}^{\mathrm{em}}}{Q_\mathrm{i}^{\mathrm{es}}} \propto \beta \quad , \tag{7.5}$$

which is in line with the linear result shown in Fig. 7.1.

Nonlinearly, however, one empirically finds

$$\frac{Q_\mathrm{e}^{\mathrm{em}}}{Q_\mathrm{i}^{\mathrm{es}}} \propto \beta^2 \quad , \tag{7.6}$$

as shown in Fig. 7.1. This change can also be explained by the model. Fig. 7.3 illustrates that due to random phases between $\tilde{T}_{\mathrm{e}\|}$ and $\tilde{q}_{\mathrm{e}\|}$, $\mathcal{T}_1$ is small. The same applies to $\mathcal{T}_2$, since $\tilde{B}_x$ and $\tilde{T}_{\mathrm{e}\|}$ have a phase of ~ 0. Moreover, $\tilde{B}_x$ and $\tilde{q}_{\mathrm{e}\|}$ have a phase of $\sim -\pi/4$, resulting in $\mathcal{T}_3 \propto \beta^2$ becoming the dominant term, yielding the overall quadratic scaling. Consequently, for the magnetic component of the

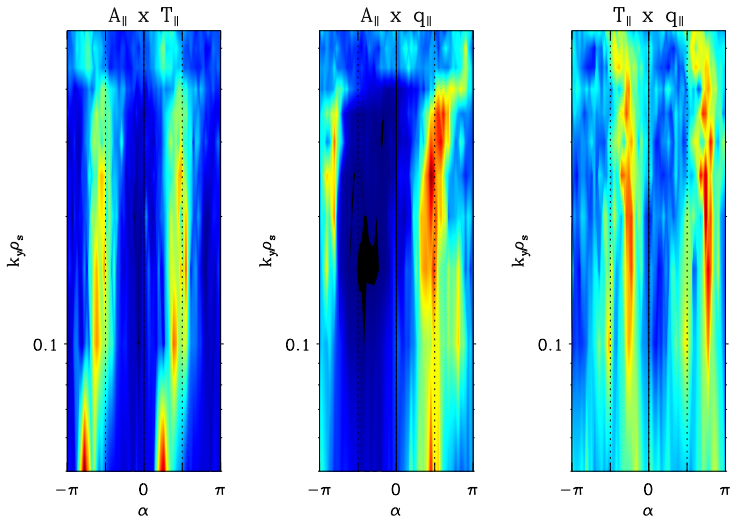

Figure 7.2: Linear cross phases for the Rechester-Rosenbluth model, as obtained from the CBC simulations. From left to right, the phases of $A_\parallel \times T_\parallel$, $A_\parallel \times q_\parallel$, and $T_\parallel \times q_\parallel$ are shown; in the linear case, comparing the second and third (corresponding to terms $\mathcal{T}_3$ and $\mathcal{T}_1$ in the text, respectively) shows that $\mathcal{T}_1$ dominates, while the leftmost graph is included only for comparison with the nonlinear results (see Fig. 7.3). Note that the phase between $A_\parallel$ and $\tilde{B}_x$ is $\pi/2$.

(nonlinear) electron thermal diffusivity, the equation

$$\chi_\mathrm{e}^\mathrm{em} \approx \chi_{\mathrm{e}\parallel} \frac{\langle \tilde{B}_x^2 \rangle}{B_\mathrm{ref}^2} \tag{7.7}$$

may be used. Together with Eq. (7.4), one arrives at

$$\chi_\mathrm{e}^\mathrm{em} \approx q_0 R_0 \left(\frac{T_\mathrm{e}}{m_\mathrm{e}} \right)^{1/2} \frac{\langle \tilde{B}_x^2 \rangle}{B_\mathrm{ref}^2} \quad . \tag{7.8}$$

After showing qualitative agreement between the model and linear as well as nonlinear simulations via transport scaling, the quantitative validity of this relation is demonstrated below.

7.1.3 Application to CBC Simulations

In Fig. 7.4, the predictions due to the transport model are compared with the simulation results. Very good agreement between the model and the real magnetic

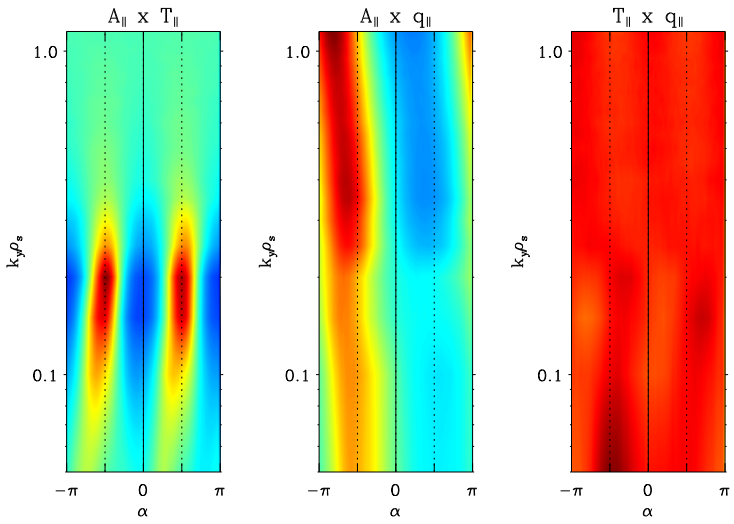

Figure 7.3: Nonlinear cross phases for the Rechester-Rosenbluth model, as obtained from the CBC simulations. The phases shown here correspond to the terms $\mathcal{T}_1$ ($T_\parallel \times q_\parallel$, right), $\mathcal{T}_2$ ($A_\parallel \times T_\parallel$, left), and $\mathcal{T}_3$ ($A_\parallel \times q_\parallel$, center), as described in the text. In this case, $\mathcal{T}_3$ dominates.

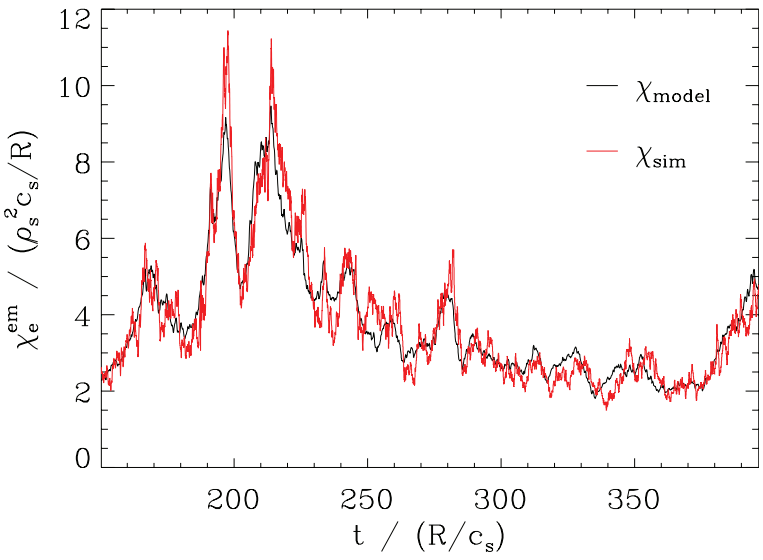

Figure 7.4: Electron magnetic transport as observed in the simulation (red curve) and as calculated by the transport model from the magnetic field fluctuations (black curve), for CBC parameters. Using a scalar gauge factor of order unity, one finds very good agreement of the two curves.

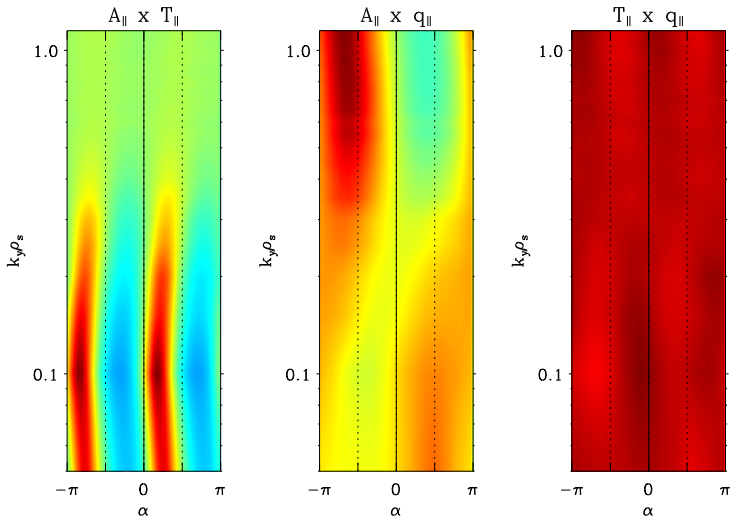

Figure 7.5: Nonlinear cross phases for the Rechester-Rosenbluth model, as obtained from the TEM simulations. The term correspondence of the phases is given in the caption of Fig. 7.3. Unlike in the CBC, the $\mathcal{T}_2$ contributors are not out of phase anymore, with a phase angle similar to those of $\mathcal{T}_3$.

transport is obtained when multiplying $\chi_{\mathrm{e}\|}$ by a scalar quantity η of order unity,

$$\chi_{\mathrm{e}}^{\mathrm{em}} = \eta q_0 R_0 \left(\frac{T_{\mathrm{e}}}{m_{\mathrm{e}}}\right)^{1/2} \frac{\langle \tilde{B}_x^2 \rangle}{B_{\mathrm{ref}}^2} \quad . \tag{7.9}$$

η depends on the shape of the extended ballooning mode structure and will therefore not necessarily be identical for different turbulence regimes. In fact, it is found that $\eta_{\mathrm{ITG}} = 0.625 \pm 0.026$ in the range from $\beta = 0.3\%$ to $\beta = 1.0\%$ (as expected, the model breaks down as $\beta \to 0$); for the high-β end of the ITG-TEM regime, as well as the KBM regime, there is little statistics – the corresponding values are $\eta_{\mathrm{ITG-TEM}} = 0.37$ and $\eta_{\mathrm{KBM}} = 0.46$. It is to be noted that all these values are rather similar and that within any single regime, there is no significant β dependence of η. Also note that this transport model seems to distinguish nonlinear regimes along the lines of the linear regimes, not changing η at $\beta = 0.8\%$.

7.1.4 Modeling Magnetic TEM Transport

When the above formalism is applied to the TEM turbulence simulations presented in Ch. 6, one observes changes in the phase structure which for the CBC

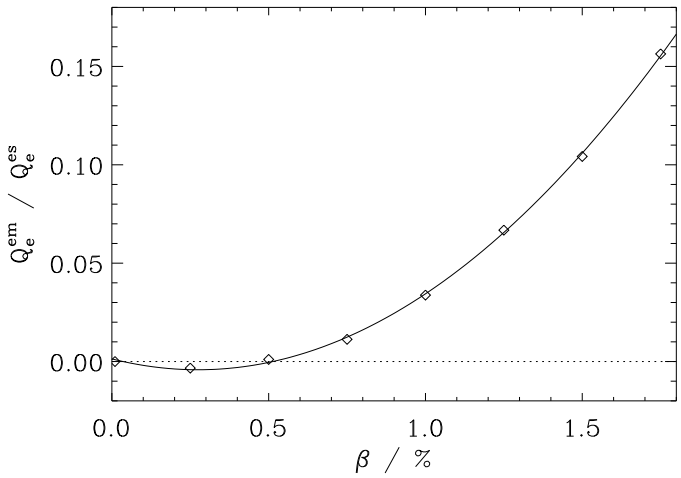

Figure 7.6: Nonlinear scaling of the TEM electron magnetic transport (normalized to the electrostatic component) with β (diamonds). As the data points are fitted well by a quadratic function (solid curve), the transport model seems to be unaffected by the altered cross-phase scenario of the TEM case (as presented in Fig. 7.5).

balances the terms in favor of the Rechester-Rosenbluth model. For the density gradient driven TEMs, the nonlinear phases are different, as can be seen in Fig. 7.5. More specifically, $\mathcal{T}_3$ – which needs to dominate in order for the model to be applicable – now has rather unfavorable phases. However, as the relative magnitudes of the terms are governed not only by their respective cross phases, but also by the amplitudes of their constituents, this seems to have little impact on the scaling of the magnetic transport levels which still grow quadratically with β (see Fig. 7.6). This scaling suggests that the model might indeed be valid, despite the phase relations.

Applying the model to the nonlinear TEM simulation data, one arrives at a picture which is consistent with the β^2 proportionality of the transport – the model matches the measured magnetic heat diffusivity well, with the scaling factor η from Eq. (7.9) being confined to the range of $\eta_{\mathrm{TEM}} \in [0.49, 0.70]$ for β values from 1.0% to 1.75%. Again, β values with very low transport are excluded to avoid statistical errors, and values near the KBM onset are neglected in order not to be affected by mode interactions. It shall be noted, however, that for the CBC, η was found to be more stable within one turbulence regime.

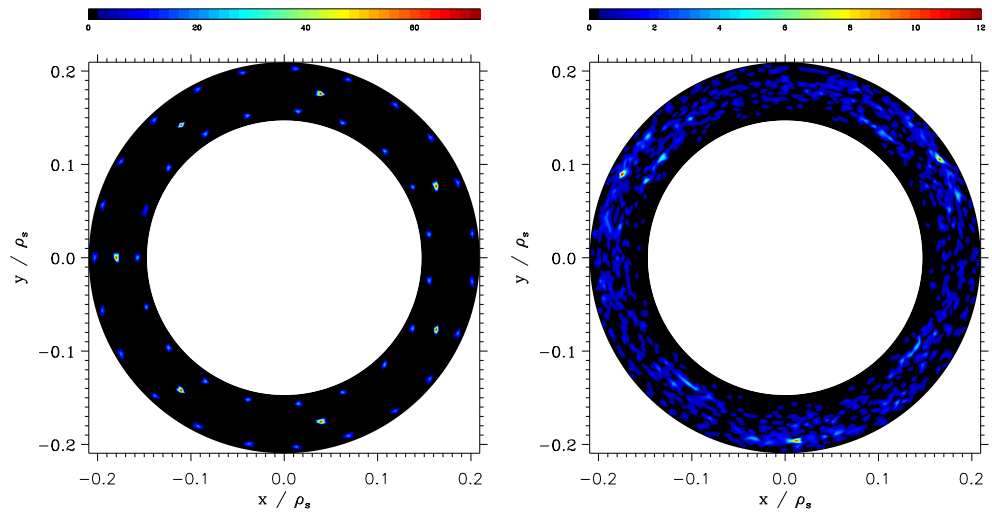

Figure 7.7: Cross-section of the torus with constant toroidal angle ϕ. Poincaré histograms of unperturbed (left) and perturbed (right) magnetic field lines are shown, with the latter obtained from magnetic field data at $\beta = 0.6\%$ for a single time step in the saturated range. As a seed field, three radial positions were used, which were then followed for $N_{\mathrm{tor}} = 500$ toroidal cycles. In the unperturbed case, resonances at all radial positions can be seen, whereas in the perturbed case, only one resonance appears which does not coincide with any of the initial radial positions (see the text for details).

These findings support the transport model and its robustness with respect to non-ideal cross phases. Since the scenarios for which it was tested in the present work cover a wide range of turbulence types, it is inferred that its nature is fairly general, with a wide range of applicability when using a (regime-dependent) scaling factor η.

7.2 Field Line Fluctuations

While magnetic field fluctuations influence the trajectories of charged particles, especially those of the light electrons, finite plasma pressure results in the particles acting back and distorting magnetic field lines; thus, magnetic field fluctuations are both cause and effect in self-consistent simulations.
Using the previously described GENE diagnostic for field line integration (see Ch. 3), the electromagnetic CBC simulations from Ch. 5 are analyzed in order to understand the properties of the altered magnetic field structure. It is to be noted

that in the electrostatic limit (i.e., in the absence of magnetic field fluctuations), every field line that lies on a flux surface with rational safety factor

$$q = \frac{m}{n} \quad , \quad m, n \in \mathbf{N} \quad , \tag{7.10}$$

will produce m points in a Poincaré section of constant ϕ before closing back in itself. In the $\hat{s}$-α geometry employed here, the radial dependence of q can be written as

$$q(r) = q_0 \left(1 + \hat{s}\frac{r - r_0}{r_0}\right) \quad . \tag{7.11}$$

At finite β however, results can be harder to interpret. For instance, very small fluctuations in the $q(r)$ profile will create and destroy such resonances very quickly, increasing the likelihood that these resonances have little chance of influencing the passing particles – more specifically, in order for a particle to feel the effect of such a resonance, it would have to travel $\geq m$ times around the torus toroidally before the resonance disappears; as their observed lifetime usually is only a few to a few ten time steps, hardly any particles fall into this category, especially if there is a typical cutoff in parallel velocity space around $L_{v\parallel} = 3$. A typical case with $\beta = 0.6\%$ is shown in Fig. 7.7, in comparison with the electrostatic limit, both consisting of three seed lines. In the absence of fluctuations, resonances occur corresponding to the (rational) q values at the seed line positions; here, a central field line ($r = r_0$ and $q(r) = q_0 = 1.4$) is accompanied by two lines at $r = r_0 \pm L_x/3$, with $q = 1.533$ (outer line) and $q = 1.267$ (inner line). The resulting resonances thus have m/n ratios of 7/5, 23/15 and 19/15, respectively, which agrees with number of observed points in the graph. In the case with finite β, only one resonance is detected, with three poloidal points. Measuring the radial position of these points, an unperturbed safety factor $q_{\mathrm{equil}}(r) = 1.48$ is obtained. This is very close to the value $q(r) = 1.5$ which corresponds to a 3/2 resonance. Fluctuations of the magnetic shear (and thus the $q(r)$ profile) cause this increase. Quantitatively, this requires an increase of $\hat{s}$ by $\Delta\hat{s} = 0.197$, a value only moderately larger than the (time-averaged) shear fluctuation due to zonal fields for this simulation, $\tilde{s} \approx 0.11$, as given in Ch. 5.

Additionally, magnetic islands may form (see, e.g., Fitzpatrick [103]). Such islands are known to enhance the transport significantly, as particles (and thus energy) caught in island structures can move significant radial distances without crossing field lines. Islands of finite width are not found in the present simulations, however.

Instead of looking for island formation, it is also possible to measure the typical radial dislocation Δr of a field line for a given number of toroidal cycles. The

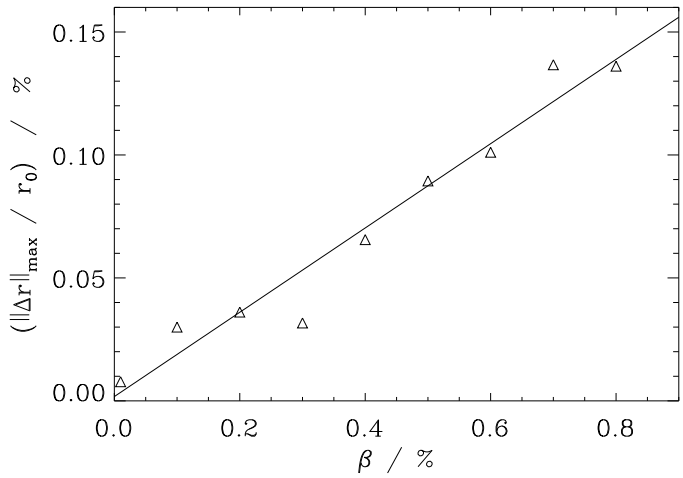

Figure 7.8: Radial dislocation of a central field line after 20 toroidal cycles as a function of β. These values were obtained by evaluating the maximum of the dislocation for every time step in a time interval of $30c_s/R_0$ and then performing a time average. The results may be interpreted as a general scaling estimation, since the low statistics resulting from this generally rather expensive procedure make precise quantitative assessments difficult.

result for the central (i.e., $r = r_0$) field line is shown as a function of β in Fig. 7.8. Here, a single field line was followed for $N_{\mathrm{tor}} = 20$ toroidal cycles at a reduced resolution of $N_z = 1000$ (which is sufficient here since N_{tor} is rather small). Its maximal radial deviation from the original position was evaluated, and the procedure was repeated for multiple time steps, spanning a time range of $30c_s/R_0$ in the saturated phase. Due to the low number of toroidal cycles, as well as the limited time average corresponding to only a fraction of the saturated phase, the interpretation of the results is difficult; however, a linear β scaling is observed – this is in line with $\tilde{B}_x/B_0 \propto \beta$, as found for the CBC simulations and noted in the next section. Radial dislocation of a field line may serve as a measure for how strongly heat and particle transport may be influenced by magnetic field fluctuations. For a precise quantitative model based on the above analysis method, significantly better statistics are required; obtaining these is aimed at in future investigations.

To demonstrate that the diagnostic delivers converged and physical results, while at the same time investigating additional physics, the diffusivity of magnetic field

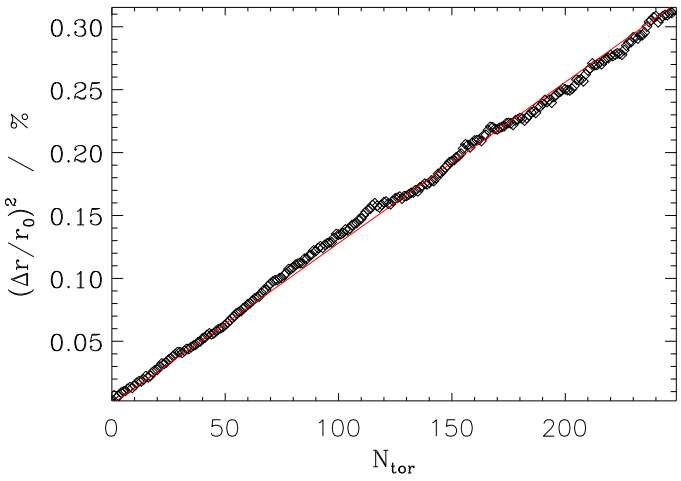

Figure 7.9: Square of the radial dislocation of a central field line as a function of the number of toroidal cycles (black diamonds). The results were obtained at a β value of 0.6%, averaging over a time range of $100 c_s/R_0$ in the saturated regime. A straight line (red) is fitted to the data; clearly, a direct proportionality is found, highlighting the diffusive nature of the system.

lines was evaluated. N_z was set to the standard value of 3000, and a single field line (initially positioned at $r = r_0$) was followed for $N_{\rm tor} = 500$; this was repeated for many time steps, covering a range of $100 c_s/R_0$. For each step, the square of the radial displacement was measured, with the result shown in Fig. 7.9, where only the values for $N_{\rm tor} \leq 250$ were included. Clearly, the points lie on a straight line, corresponding to

$$\left(\frac{\Delta r}{r_0}\right)^2 = 1.3 \times 10^{-5} N_{\rm tor} \quad . \tag{7.12}$$

Using this result, one may evaluate the corresponding diffusion coefficient:

$$D_r = \frac{\langle \Delta r^2 \rangle c_s}{4\pi q_0 R_0 N_{\rm tor}} = 1.3 \times 10^{-5} \frac{\epsilon_t^2}{4\pi q_0} c_s R_0 = 2.4 \times 10^{-8} c_s R_0 \quad , \tag{7.13}$$

where a general form $D_r = \langle \Delta r^2 \rangle / (2t)$ was assumed, and $t = 2\pi q_0 R_0 / c_s$ was inserted. Note that for larger $N_{\rm tor}$ than those shown in Fig. 7.9, the curve slowly starts to flatten; the explanation for this effect is that in those cases, some of the field lines have already reached the end of the radial box. Due to the periodic boundary conditions, the resulting displacement is thus caused to be lower than the physical value.

In order to allow for quantitative assessment of this result, one may obtain an estimate by performing a comparison with electrostatic particle diffusivities. As shown in Ref. [104], the Kubo number $K = v_E \tau_c / \lambda_c$ is a measure for how strongly particles are bound to structures in the turbulent field. Here, v_E is the $\mathbf{E} \times \mathbf{B}$ velocity, τ_c the correlation time, and λ_c the correlation length. For magnetic fluctuations, the expression becomes $K = v_B \tau_\parallel / \lambda_\perp$. From Ref. [105], it follows that

$$K = \frac{\tilde{B}_x}{B_0} \frac{v_\parallel \tau_\parallel}{\lambda_\perp} = \frac{\tilde{B}_x}{B_0} \frac{\lambda_\parallel}{\lambda_\perp} \approx 0.16 \quad , \tag{7.14}$$

taking the $\beta = 0.6\%$ case and inserting typical dimensions of turbulent structures ($5\rho_s$ for the perpendicular and $\pi q_0 R_0/2$ for the parallel coordinate), as found in the simulations, for the respective correlation lengths. In the $K < 1$ regime, a simple random walk behavior is to be expected, and one may therefore write

$$D_r = v_B^2 \bar{\tau}_\parallel = \left(0.36 \frac{\rho_s}{R_0} \right)^2 \frac{\pi}{6} c_s R_0 = 2.8 \times 10^{-8} c_s R_0 \quad . \tag{7.15}$$

Here, use was made of an adjusted correlation time $\bar{\tau}_\parallel = \tau_\parallel / 3$ (see Ref. [105]); for ρ_s / R_0, a value of 6.4×10^{-4} was used, identical to the choice for the magnetic field line integration. Clearly, the results in Eqs. (7.13) and (7.15) agree very well, considering only a simple model was used. A different approach to exploring diffusivities in turbulent electromagnetic fields is detailed in the next section.
Many other investigations into the magnetic structure of gyrokinetic simulations are possible. The results obtained here with the field line diagnostic represent mostly proof of concept studies. In a next step, it is planned to apply the diagnostic to simulations of neoclassical tearing modes which are known to create magnetic island structures.

7.3 Fast Ions in Turbulent Electromagnetic Fields

Following Hauff et al. [105], the behavior of fast passive ions in the turbulent fields of the CBC simulations discussed in Ch. 5 is investigated. Simulations were performed with identical parameters as in that chapter for the active (ion and electron) species, with additional passive ion species at high temperatures.

7.3.1 Background

In fusion plasmas, fast ions occur, e.g., as a result of heating via Neutral Beam Injection or in the form of helium nuclei bred in fusion reactions (see, e.g., Ref. [5]).

Since they carry significant energy, it is important to understand how these particles behave in turbulent fields, and to investigate the diffusive behavior of such particles quantitatively. It shall be noted that fast particle physics also has various applications in astrophysical scenarios; an example may be found in Ref. [106]. Experimentally, multiple fast particle studies have been performed (see, e.g., Refs. [107] and [108]). Previous theoretical investigations (see, e.g., Refs. [109] and [110]), however, have mostly relied on the use of orbit-averaged fields [63], thus making an assumption which is not necessarily valid. In fact, if the particle drifts by more than the correlation length of the potential during one banana orbit, this type of averaging cannot be used. Typically, that is the case when the energies E of the fast ions exceed $E > 3T_\mathrm{e}$.
Due to this reason, a different approach to the problem is taken. By performing gyrokinetic simulations of electromagnetic turbulence, finite orbit radii effects are retained. The results of these simulations are then compared to the scalings obtained by simple orbit analyses (see Ref. [105]), which read

$$D^{\mathrm{es}}_{\mathrm{fi,p}}(E) \approx \frac{v_E^2 \lambda_c}{6\eta^2} \left(\frac{E}{T_\mathrm{e}}\right)^{-1} \tag{7.16}$$

$$D^{\mathrm{es}}_{\mathrm{fi,t}}(E) \approx \frac{v_E^2 \lambda_c^2 \epsilon_t^{1/2}}{12(\pi\eta^2(1-\eta^2))^{1/2}} \left(\frac{E}{T_\mathrm{e}}\right)^{-3/2} \tag{7.17}$$

$$D^{\mathrm{em}}_{\mathrm{fi,p}}(E) \approx \left(\frac{R_0 \tilde{B}_x}{\rho_s B_0}\right)^2 \frac{\lambda_c}{6\eta^2} \tag{7.18}$$

$$D^{\mathrm{em}}_{\mathrm{fi,t}}(E) \propto \left(\frac{E}{T_\mathrm{e}}\right)^{-1/2} \tag{7.19}$$

where $\eta = v_\parallel / v$ is the pitch angle, λ_c is the (perpendicular) correlation length of the corresponding field (electrostatic for es and magnetic for em), and the indices p and t denote passing ($\eta \to 1$) and trapped ($\eta \to 0$) particles, respectively. The quantity $R_0 \tilde{B}_x / (\rho_s B_0)$ is estimated from the β scan in Ch. 5 to be 60β. Note that for the TEM case in Ch. 6, it is smaller by roughly a factor of five.

7.3.2 Passive Fast Ion Simulations

GENE simulations with CBC parameters are performed, using the same numerical parameters as in Ch. 5 (with the exception of an increased resolution in the μ direction, $N_\mu = 16$) in the $\beta = 0.6\%$ case, but adding singly charged passive ion species (denoted by the index fi) with $\omega_{n\mathrm{fi}} = \omega_{n\mathrm{i}} = 2.22$ and $\omega_{T\mathrm{fi}} = 0$ with hydrogen mass. Such species are investigated with temperatures of 30, 50, and 100 in units of $T_\mathrm{i} = T_\mathrm{e}$. These simulations were then analyzed with respect to the structure of the radial particle diffusivity $D_\mathrm{fi}(v_\parallel, \mu)$ in velocity space. As shown

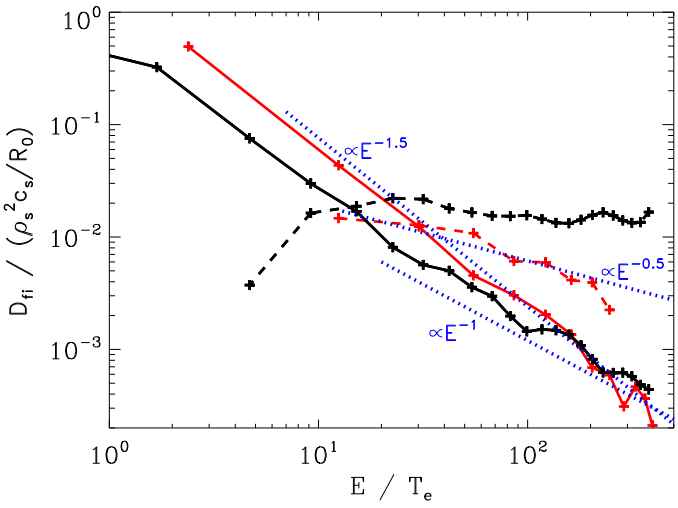

Figure 7.10: Scaling of the particle diffusivities of passive fast ions with the particle energy; power law scalings are provided for comparison (blue dotted lines). For moderate and high energies, the electrostatic component (solid lines) shows scaling powers of -1.5 and -1 in the $\eta \to 0$ (red) and $\eta \to 1$ (black) limits, respectively; for the electromagnetic component (dashed lines), those values are -0.5 for $\eta \to 0$ and zero (constant diffusivity) for $\eta \to 1$.

in Fig. 7.10, the simulation results are in good agreement with the analytical predictions shown in Eqs. (7.16) to (7.19).

7.4 Effects of Realistic Geometry

Considering that one of the main motivations for performing electromagnetic simulations and studying effects therein lies in the attempt to understand experimental β scalings, it is insightful to perform simulations not only in $\hat{s}$-α but also in realistic geometry. The former constitutes a strong approximation of real tokamak equilibria, especially in high β, shaped plasmas; studying the β dependence of turbulence in a realistic geometry instead is expected to yield additional understanding of the connection between simulations and the experiment. The computational results presented in this section were obtained in collaboration with L. Laborde and were published by Pueschel et al. [111]. Recently, Chen and Parker [112] have published first simulation results on the effects of realistic geometry on gyrokinetic simulations at finite β, focussing on numerical aspects.

It may be expected that in the near future, more elaborate studies of the matter will be performed.

7.4.1 Modeling a JET Discharge

The recent dedicated JET β scaling experiment (discharge #68595) reported in Ref. [65] offers a good basis for numerical simulations. The normalized parameters taken at mid-radius are $\omega_n = 1.4$, $\omega_{T\mathrm{e}} = 4.8$, $\omega_{T\mathrm{i}} = 5.8$, $q_0 = 1.6$, $\hat{s} = 1.1$, and $T_\mathrm{i}/T_\mathrm{e} = 0.86$. Fig. 7.11 shows the geometry of the magnetic surfaces identified by the EFIT code constrained by Motional Stark Effect data. The triangularity is relatively high ($\delta = 0.4$), as well as the Shafranov shift which compresses the magnetic surfaces on the low field side. The TRACER code (see Ch. 2) was used to reconstruct the geometry of a flux tube for the GENE code according to this equilibrium.

7.4.2 Transport Levels

Nonlinear simulations were performed in this configuration for four different β values covering the experimental range: $\beta = 0.85$, 1.05, 1.12, and 1.2% (note that for all of these β values, the linearly dominant instability is a TEM). The results are shown in Fig. 7.12. Over this range of β, one observes hardly any changes of the ion and electron heat fluxes. This clearly contrasts with the experimental observation of a strong degradation of confinement time with increasing β – as mentioned before, $\Omega_\mathrm{i}\tau_E \propto \beta^{-1.4}$ –, but agrees with a fluid modeling which suggests that this experimental degradation is due to a mismatch in the dimensionless parameters (see Ref. [65]). It is also worth mentioning that the electromagnetic contribution is negligible compared to the electrostatic fluxes. These findings are agreeing only partially with the $\hat{s}$-α simulations presented before; while the TEM case shows little influence of β on the fluxes over a wide range of values, and its electromagnetic component of the electron heat flux is reduced in comparison with the CBC results, the magnetic transport is still much higher than that which is found here. Whether or not this is a general effect that is to be expected in realistic geometry remains to be seen. A more likely explanation, however, is that it is just a property of this specific parameter set; additional investigations into the issue are planned for the future.

Turning to an issue for which comparisons with previous work are more readily available, the nonlinear upshift of critical driving gradients is discussed below.

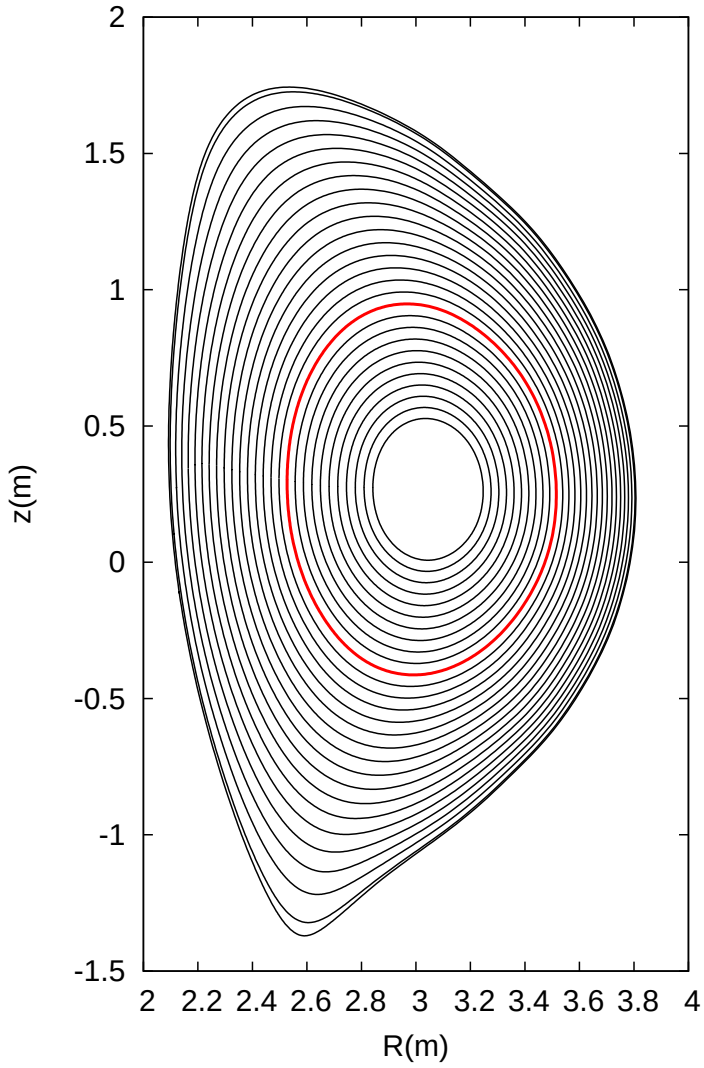

Figure 7.11: JET plasma equilibrium used in the β scaling experiment (pulse #68595); the flux surface considered here (at $r_0 = 0.5a$) is represented by a bold red line. The main difference of this geometry from the $\hat{s}$-α model used before lies in the strong elongation.

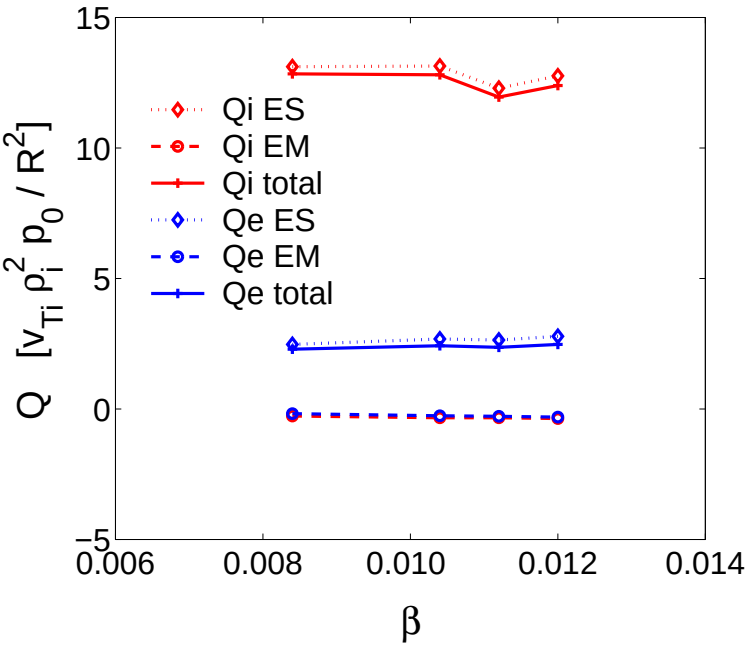

Figure 7.12: Electrostatic (ES) ion (Q_i; upper red curves) and electron (Q_e; lower blue curves) heat fluxes as a function of β, after full saturation of nonlinear simulations. The (negligible) electromagnetic (EM) components are also included (dashed lines). The linearly dominant instability at these parameters is a TEM; nonlinearly however, ion fluxes exceeding their electron counterparts hint at different processes dominating the turbulence.

7.4.3 Dimits Shift

Linear and nonlinear scans over the ion temperature gradient $\omega_{T\mathrm{i}}$ were also performed around the experimental value $\omega_{T\mathrm{i}} = 5.8$ in order to identify a threshold $\omega_{T\mathrm{i,crit}}$ from which on ITG modes drive the turbulence. Fig. 7.13 shows, as a function of $\omega_{T\mathrm{i}}$, the growth rate of the most unstable mode from the linear scan, as well as the ion and electron electrostatic heat fluxes from three nonlinear runs. The linear scan displays a knee around $\omega_{T\mathrm{i}} = 5$, making the identification of a critical value slightly more difficult; still, $\omega^{\mathrm{lin}}_{T\mathrm{i,crit}} \approx 3.6$ serves as a realistic estimate. Even if one allows for some uncertainty, the corresponding value for the nonlinear simulations, $\omega^{\mathrm{nonlin}}_{T\mathrm{i,crit}} \approx 4.7$, is still larger than the linear threshold. This property is the so-called Dimits shift first reported by Dimits et al. [56], and the above findings agree very well with similar research published recently by Mikkelsen and Dorland [113].

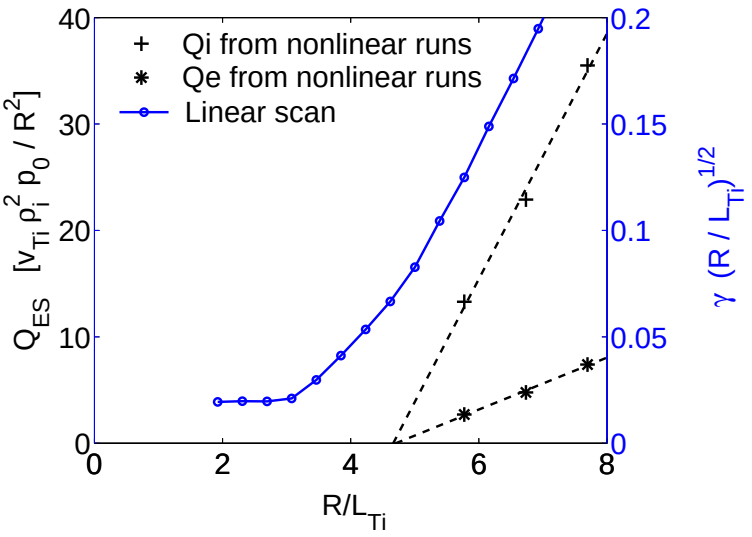

Figure 7.13: Linear and nonlinear scans of the normalized ion temperature gradient: the linear growth rates indicate a threshold $R/L_{T\mathrm{i}} = \omega^{\mathrm{lin}}_{T\mathrm{i,crit}} \approx 3.6$ whereas the fit from nonlinear heat fluxes suggests $\omega^{\mathrm{nonlin}}_{T\mathrm{i,crit}} \approx 4.7$. This is due to the Dimits shift described in the text.

At the same time, the Dimits shift highlights a property that may contribute to the differences between the experimental scaling and that observed in the simulations: in the parameter regime investigated here, small changes – e.g., of the ion temperature gradient – can lead to significant deviations in the heat flux, as becomes apparent in Fig. 7.13. Thus, if one aims to reproduce experimental heat flux measurements, one has to perform simulations not only at that specific parameter set, but additionally take the error bars of all parameters into account. Since those error bars can be significant, and since turbulent flux levels may depend strongly on many parameters, matching simulation and experimental data directly can be a difficult undertaking. Still, it is important to pursue this line of investigation to understand the impact of geometry on β scaling more thoroughly.

7.5 Chapter Summary

In this chapter, various analyses of electromagnetic turbulence were performed. A magnetic transport model was investigated in detail, and its applicability was demonstrated for a wide range of turbulent regimes both qualitatively and quan-

titatively. Then, field line integration was used to obtain information about the altered magnetic field structure in the presence of magnetic field fluctuations – specifically, diffusive behavior was observed which was explained well by a simple model. The properties of fast ion diffusivities was studied next, and good agreement was found with analytical scalings as reported by Hauff et al. [105]. Finally, a first investigation into the effects of realistic geometry on finite-β turbulence was presented.

Chapter 8

Application to Astrophysical Scenarios

The applicability of the gyrokinetic framework and, more specifically, the GENE code to astrophysical scenarios is discussed – it is possible to take results obtained from fusion plasma simulations (as reported in the previous chapters) and insert cosmic scales into the normalizations. Two examples are given: Cooling flows are observed in some galaxy clusters, yet no cold matter seems to be present; heat transport is believed to be the process causing this effect. On the other hand, evaporating clouds are cold and dense objects in a much hotter medium. It is generally believed that they are kept together by magnetic fields.

8.1 Gyrokinetics on Astrophysical Scales

In the derivation of gyrokinetic theory in Ch. 2, two characteristic length scales were introduced: a macroscopic scale describing the change of the equilibrium quantities and the magnetic geometry, as well as the microscopic scale of the turbulent processes perpendicular to the magnetic field. While this picture, with $\rho \ll L_{\mathrm{ref}}$, was designed to match the physical conditions in toroidal fusion devices, its validity extends beyond this range of applications. More specifically, some astrophysical systems exhibit features which may be described using the gyrokinetic framework as implemented in the GENE code.
Astrophysical magnetic field strengths span an enormous range, with more than 18 orders of magnitude lying between parts of the intracluster medium (ICM) and the surface of magnetars; the gyroradii of charged particles vary accordingly. Interestingly, the fields used in terrestrial fusion – which correspond to the upper limit of technologically achievable fields – lie in the very middle of this scale.

However, for the cases investigated here, magnetic fields $B_{\text{astro}} \ll B_{\text{fusion}}$ are typical, which result in gyroradii of order $\rho \sim \mathcal{O}(\text{m} - 10^3\,\text{km})$ at temperatures of $\sim 10^7\,\text{K}$. However, the gyrokinetic ordering is still fulfilled, with $L_{\text{ref}} \gg \rho$.
For fusion plasmas, error bars of experimental measurements constitute a difficulty for the application of simulations. This is even more problematic for astrophysical scenarios where some quantities are not even certain within an order of magnitude. Keeping this in mind, the results reported here should be seen as estimates and not as precise measures.
Many astrophysical plasmas have a complex abundance of many different elements, and a lot of those particles are only partially ionized. While technically, GENE is able to include any number of elements, covering thousands of particle species with their respective physical time scales poses a computational limit. Therefore, only fully ionized hydrogen plasmas are considered in the following, and effects due to other species are only mentioned in a qualitative way. Additionally, the normalization length is taken to be $L_{\text{ref}} = L_T$ – defining a major radius R proves to be difficult since in most cases, very little is known about the fine structure of the magnetic field geometry.

8.2 Galactic Cooling Flows

8.2.1 Motivation and Previous Investigations

Cooling flows (see Fig. 8.1) constitute a common process for the formation of compact objects in the universe. To describe this phenomenon in an idealized fashion, a gas cloud (note that throughout this chapter, the category of gases is understood to include plasmas) of uniform density is considered. Assuming a low initial temperature (and thus, low pressure), the cloud will start to collapse, with the outer shells falling towards the inner shells due to their weight. This causes both the density and the temperature to rise, the latter as a result of the conversion of potential into kinetic and thus thermal energy. As soon as the pressure – which rises rapidly – is large enough to balance the gravitational force, the collapse is halted; the system is now in hydrostatic equilibrium. However, since the temperature is large, so are radiative losses, e.g., via bremsstrahlung. The current state is therefore not stable, and temperature losses are compensated by further inflow of matter. Generally, the picture is more complex, and the presence of magnetic fields, external heat sources, or inhomogeneities of the flow may have to be considered.
While the formation, e.g., of smaller, single galaxies from cooling gas is fairly

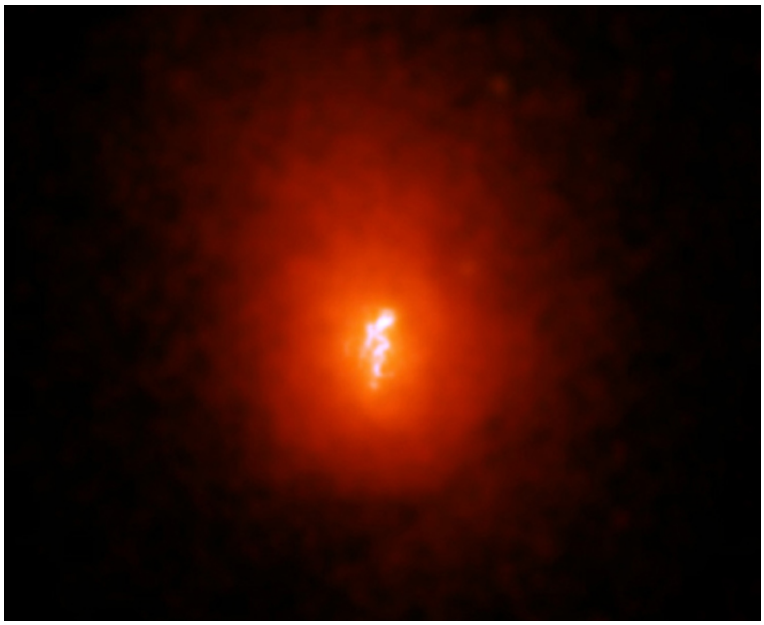

Figure 8.1: Abell 1795 cluster. In the center of this cluster, a cooling flow can be observed in the form of a bright filament. It consists of gas at lower temperatures than its surrounding. Source: [114]

well understood, open questions remain about gas clouds in the central regions of galaxy clusters. Since these clouds are radiating in the X-ray band, cooling flows towards the centers of these objects are to be expected. At first, it was believed that cooling flows were operating fairly unhinderedly in the clusters and that the resulting cold gas in the center was dropping out and becoming unobservable (see Fabian [115] for an earlier review). For this to happen, radial heat transfer from the hot outer shells to the cooler inner shells has to be suppressed.
The standard picture, however, has since changed (see, e.g., Voigt et al. [116], as well as Voigt and Fabian [117]). In many ICM observations with X-ray emitting gas, no sufficiently large quantities of cold matter were observed at the centers of these objects where the gas should have ended up after completing the cooling process. It is more than unlikely that many initial stages of ICM cooling are observed but none where the process has been at least partially completed. Since the typical cooling times t_{cool} of these objects are smaller than the Hubble time

$$t_H = H_0^{-1} = 1.38 \times 10^{10}\,\mathrm{yrs} \tag{8.1}$$

(which is an estimate for the age of the universe), with the Hubble constant

$H_0 = 71\,\mathrm{km/(s\,Mpc)}$, examples of later stages of ICM matter inflow should have been found. Consequently, processes have to exist that offset the cooling.
It has been proposed that external heat sources may balance the radiative losses mentioned above (see, e.g., Churazov et al. [118]); there also exist theories which would allow for cold matter to drop out, involving, e.g., differential absorption [119] or inhomogeneous distribution of metallicity throughout the gas [120]. Most of these explanations, however, do not apply to the majority of clusters or constitute only very small contributions.
Instead, the most likely theory is that cooling flows are offset by conduction (note that in the context of cooling flows, conduction does not necessarily refer to classical heat conduction; turbulent phenomena are also included): The inner radial shells receive thermal energy from the warmer outer shells. This way, effective cooling of those shells is suppressed, and the matter inflow halted.
Classical thermal conduction (as described by Spitzer [121]) results in the Spitzer conductivity

$$\kappa_S = \frac{1.84\times10^{-5}T^{5/2}}{37.8 + \ln\left[\left(\frac{T}{10^8\,\mathrm{K}}\right)\left(\frac{n_\mathrm{e}}{10^{-3}\,\mathrm{cm}^{-3}}\right)^{-1/2}\right]}\,\mathrm{erg\,s^{-1}\,cm^{-1}\,K^{-1}} \quad . \tag{8.2}$$

In the case of functional cooling flows, it has been argued that conduction must be suppressed, $\kappa = f\kappa_S$ with $f < 1$, an effect caused by magnetic fields; as to the magnitude of the suppression, while Churazov et al. [118] find $f \sim 0.01$, work by Narayan and Medvedev [122] suggests $f \sim 0.3$, requiring tangled field lines. However, as discussed in Ref. [117], it has been estimated that heat transfer must be larger in order for the cooling to be compensated, with required conductivities of $\kappa > \kappa_S$ at the center of the objects – more specifically, $f \geq 2$.
Turbulent transport is able to exceed classical heat conduction significantly. Cho et al. [123] performed simple hydrodynamic and MHD simulations; their results were then applied more comprehensively by Voigt and Fabian [117]. The conductivity is found to be of the order of the unhindered Spitzer value, $f \sim 1$, where a simple ansatz

$$\kappa_\mathrm{turb} \approx v_\mathrm{turb} l_\mathrm{inject} \tag{8.3}$$

is used. Here, v_turb is a characteristic turbulent velocity, and l_inject corresponds to a typical turbulent length scale. However, Fabian et al. [124] present arguments against turbulence being a dominant process, based on observations of quasi-linear filaments in the Perseus cluster; this reasoning does not apply to microturbulence, though. In the following, the applicability of GENE simulation results to the scenario described above is discussed. Unlike previous work (see,

e.g., Pistinner and Eichler [125]) employing kinetic theory which sought to find processes that suppress heat transport to comply with the physical interpretation by Fabian [115], the considerations presented here aim to assess the maximal influence of microturbulent phenomena on increasing the heat transport.

8.2.2 Applying GENE Results to Cooling Flows

Using the normalizations and definitions in Ch. 2, one can split the heat flux into a nondimensional quantity $\hat{Q}$ (which corresponds directly to the GENE output Q) and a component Q_D absorbing the dimensions:

$$Q = \hat{Q} Q_D = \hat{Q} \frac{n_{\mathrm{ref}} T_{\mathrm{ref}}^{3/2} \rho_{\mathrm{ref}}^2}{m_{\mathrm{ref}}^{1/2} L_{\mathrm{ref}}^2} \quad . \tag{8.4}$$

Assuming a typical value of $\hat{Q} \sim 10$ (which may vary, depending on the physical parameters, by more than an order of magnitude), one may thus infer typical physical transport levels by inserting density, temperature (recalling the inclusion of the Boltzmann constant in the definition used here), gyroradius, and typical length scale describing the system. This latter variable poses something of a problem, as does the density. For instance, Godon et al. [126], investigating dynamo activity in rotating cooling flows, find magnetic loops with a characteristic length scale of $\sim 1\,\mathrm{kpc}$ in the center of the objects. Densities of cooling flows are usually specified for the outermost radius R_{cool} of the flow (where $t_{\mathrm{cool}} = t_H$), with a typical of $n(R_{\mathrm{cool}}) \sim 3{\times}10^{-3}\,\mathrm{cm}^{-3}$. However, the central densities of these objects are much larger; using mass distributions from Soker and Sarazin [127], one may expect values $n(R = 1\,\mathrm{kpc}) \sim 10^3\,\mathrm{cm}^{-3}$, assuming a simplified model with pure hydrogen plasma.

To avoid the difficulty of fixing R, the reference length is taken to be $L_{\mathrm{ref}} = L_T \sim 0.1\,\mathrm{kpc}$, corresponding to the largest gradients which are likely to occur in the context of a simple model. Additionally, high densities are considered, assuming $n \sim 10^4\,\mathrm{cm}^{-3}$, so as to maximize Q. Taking $\rho_{\mathrm{ref}} \sim 10^4\,\mathrm{km}$, $T_{\mathrm{ref}}/k \sim 10^8\,\mathrm{K}$, and $m_{\mathrm{ref}} = m_{\mathrm{H}}$, one thus arrives at

$$Q = \hat{Q} Q_D \sim 8{\times}10^{-19} \frac{\mathrm{erg}}{\mathrm{s\,cm}^2} \quad . \tag{8.5}$$

This result constitutes an extremely low heat flux; in fact, to obtain a dominant contribution to the cooling flow scenario, at least 17 orders of magnitude would have to be bridged.

There are, however, considerations which suggest a more favorable picture for microturbulence. Firstly, MHD turbulence may be present in the central area of

cooling flows, even if it is not strong enough to dominate the picture; this would create small structures (i.e., lower ρ/L_T significantly) which, in turn, would be prone to microinstabilities. Since Q is proportional to the square of ρ/L_T, a very large impact on the heat flux would have to be expected. Such smaller scales are in line with the general assumption that cooling flows are of multi-phase nature. Secondly, for the value $\hat{Q} \sim 10$ used here, a typical result with $\beta \ll 1$ was taken. In the present physical scenario, however, $\beta \sim 1$, which means that, in principle, much higher transport levels are possible. Thirdly, as mentioned before, a pure hydrogen plasma was considered; heavier and more strongly charged species are likely to cause transport levels to change, while at the same time constituting a (possibly significant) impact on the ratio $\rho^2/m^{1/2}$ which enters into Eq. (8.4). Also note that above, a static equilibrium field was assumed, and only heat flux perpendicular to the field lines was evaluated. Postulating a parallel heat diffusivity like the one used in Eq. (7.4), one obtains $Q \sim 1\,\mathrm{erg}/(\mathrm{s\,cm}^2)$; this value is indeed in the expected range.

It remains to be investigated whether these adjustments are sufficient to raise perpendicular transport due to plasma microturbulence to the point where it is able to contribute significantly to the overall heat flux in galactic cooling flow scenarios. Deeper insight must first be gained into the relevant geometry, and increasing β to realistic values requires inclusion of $B_\parallel$ fluctuations; a benchmark for the physics connected to higher β values is currently underway.

8.3 Evaporating Clouds

8.3.1 General Picture and Previous Work

A different scenario in which microturbulent transport may have an impact on the interpretation of the physical model are cold clouds near the centers of active galactic nuclei (AGNs). As described in Rees [129], a range of objects – quasars, radio and Seyfert galaxies (see Fig. 8.2) – exhibits features that may be explained by the existence of numerous dense and cold clouds which are immersed in the hot environment of the inner AGN region. Sivron and Tsuruta [130] show that such clouds explain the observed spectra well.

In a simplified model, these clouds should evaporate very quickly; therefore, magnetic fields are used to account for their existence – the internal kinetic pressure is thought to be balanced by equal magnetic pressure, $\beta \sim 1$, which holds the cloud together. To allow for the validity of this model, one has to constrain the parameter space in which clouds may live; investigations in this direction were

Figure 8.2: NGC 6814 galaxy. Its nucleus is believed to be harboring cold clouds which balance kinetic and magnetic pressure as described in the text. Source: [128]

performed by Kuncic et al. [131]. Typical parameters are taken here, with the cloud temperature $T_{\mathrm{cl}} \sim 10^5\,\mathrm{K}$ (and the surrounding medium at $T_{\mathrm{sm}} \sim 10^9\,\mathrm{K}$), the density $n_{\mathrm{cl}} \sim 10^{17}\,\mathrm{cm}^{-3}$, and the cloud radius $R_{\mathrm{cl}} = L_T \sim 10^6\,\mathrm{cm}$. As motivated in Ref. [129], the magnetic field is assumed to be $B \sim 10^{-4}\,\mathrm{T}$, and the proton gyroradius thus becomes $\rho \sim 500\,\mathrm{cm}$.

8.3.2 Application of GENE Data

Unlike in the above cooling flow case, the context in which GENE data is applied to evaporating clouds is the attempt to understand whether microinstabilities might destroy the clouds by causing evaporation as described above. To this end, the heat flux in the border between cloud and surrounding medium is examined. It is to be expected that due to the high $\beta \sim 1$, this border is parallel to the magnetic field, reducing the relevant heat flux to its parallel component.
Inserting the above parameters into Eq. (8.4) and again taking $\hat{Q} \sim 10$, one obtains a heat flux of $Q \sim 10^6\,\mathrm{erg}/(\mathrm{s\,cm}^2)$. Note that the choice of $L_T = R_{\mathrm{cl}}$ constitutes an upper limit – in reality, somewhat larger gradients may be ex-

pected, yielding higher transport. Assuming a constant heating rate, delivering energy homogeneously across the entire surface, the heating power becomes $P \sim 10^{19}\,\mathrm{erg/s}$. A heating process of this magnitude, however, would cause the cloud to evaporate after

$$t_{\mathrm{evap}}^{\mathrm{GK}} \sim (10^9 - 10^{10})\,\mathrm{s} \quad . \tag{8.6}$$

This value can be compared to the time scale for unhindered evaporation as given by Rees [129]:

$$t_{\mathrm{evap}}^{\mathrm{unhind}} \sim (10^6 - 10^7)\,\mathrm{s} \quad . \tag{8.7}$$

The latter is significantly lower than the former, but only roughly three orders of magnitude lie between both results (and the difference becomes smaller if larger gradients are considered). Therefore, if the above estimates are to hold even within a large tolerance, the general picture of evaporating clouds may have to be revisited. A more in-depth analysis will be undertaken in the near future to determine the answer to this question.

8.4 Chapter Summary

In the present chapter, typical GENE results have been used as order-of-magnitude estimates for heat transport levels in astrophysical plasmas. For galactic cooling flows – where a process is required that enhances heat transfer beyond the Spitzer rate – the applicability seems doubtful unless the gyrokinetic framework is used in conjunction with non-trivial geometry resulting from MHD activity. Evaporating clouds, on the other hand, may be affected by plasma microturbulence, with the latter becoming a relevant factor in determining the lifetime of cold, dense gas clouds near the center of AGNs. Since all the results presented in this chapter are of a very preliminary nature, more research will be undertaken to assess their validity; also, additional insight is expected to be gained by considering β values much higher than those investigated in this thesis.

Chapter 9

Conclusions

The findings of this thesis are reviewed briefly, highlighting novel results. Hereafter, an outlook is given with areas marked for future research.

9.1 Summary

Gyrokinetics and the GENE Code

A brief derivation of the gyrokinetic framework was presented; the functionalities of the GENE code – which operates on this framework – was detailed. This code was the basis for most results obtained in the context of this thesis.

Visualization

Since in typical simulations, enormous amounts of data are produced, mechanisms to visualize this data in a physically meaningful way were discussed. The GENE Diagnostics Tool – which was redesigned and extended to allow for more versatile application – was introduced, along with most of its standard diagnostics, as well as additional diagnostics, many of which were conceived during the course of the physical investigations of this work. Similarly, the RZG VisualKit, along with a program to create GENE data sets, was presented.

Numerical Diffusion

In order to avoid numerically induced effects which may pollute or even dominate the physics one seeks to describe, unphysical high-k modes have to be removed from the simulations. To this aim, a numerical (hyper-)diffusion term was introduced in the Vlasov equation; a widely applicable rule for the diffusion coefficient was derived, where the critical value was equal to the linear growth rate of the

system. Moreover, velocity space diffusion was employed to suppress numerical recurrence phenomena, and radial diffusion was investigated as a method to alter the extended mode structure and dampen the outmost radial modes which might otherwise cause an unphysical influence.
These findings were then applied to the ETG benchmark scenario where the direct applicability of the prescriptions concerning parallel, as well as parallel velocity, diffusion was demonstrated.

Electromagnetic Effects

The main focus of this thesis lies on the study of the impact of the normalized plasma pressure β. Two parameter sets were investigated: the Cyclone Base Case and density gradient driven trapped electron modes (TEMs). Linear studies of the onset of kinetic ballooning modes (KBMs) were undertaken, furthering the understanding of the threshold properties and the relevance of different thresholds. In this context, mode interactions – and even more so, mode transformations – are found to make the definition of the onset point problematic.
For the first time, nonlinear KBM turbulence simulations were reported, extending the range of accessible β values significantly. In this regime, multiple mechanisms may contribute to the very low transport levels which were observed. Quasilinear transport models were used in this context, and analyses of the zonal flow and zonal field structure were performed, detailing their influence on the saturation. The major contributor to the reduction of transport, however, was found to be nonlinear mode interactions. In the case of TEM turbulence, zonal flows were shown to explain the nonlinear behavior.
Making use of the simulations described above, the magnetic transport was investigated; it scaled as β^2 and was described very well by a test-particle model. Moreover, magnetic fluctuations affect the field line structure and its resonances. Application of a simple diffusion model yielded good agreement with the data. Apart from magnetic field line diffusion, the diffusivity of fast passive ions was explained by analytical models both for electrostatic and magnetic turbulent fields. Lastly, realistic tokamak geometry was found to have different properties in the context of magnetic transport than the standard but rather simple $\hat{s}$-α geometry employed in most of the simulations reported here.

Astrophysical Applications

A direct transfer of typical GENE transport levels to a simple model for galactic cooling flows results in a significant gap between obtained and required fluxes.

While potentially, plasma microinstabilities do not play a role in the stability of these objects, there is a range of possibilities how the gap may ultimately be bridged. In the case of cold gas clouds, which, in a simple model, should evaporate quickly, a similar transfer was performed. Microturbulent transport was found to be very efficient here, and the results allow for the destruction of such clouds on time scales only moderately larger than unhindered evaporation. This may suggest the need for refinement of the standard cloud model.

9.2 Future Investigations

Electromagnetic Fusion Plasmas

The current research is intended to be expanded by performing studies in additional parameter regimes, e.g., in order to isolate KBM turbulence and study its properties in more detail. Realistic geometry provides an opportunity to refine the simulations and ideally allow for quantitative comparisons with fusion experiments.
In the light of increasingly successful descriptions of stellarators (which operate at much larger β than tokamaks), as well as requirements for many astrophysical scenarios, investigations with $B_\parallel$ fluctuations at higher β values will be performed, comparing GENE results with other codes as well as analytic models.

Astrophysical Plasmas

Both cooling flows and evaporating clouds are to be studied in more detail in the future, along with the applicability of gyrokinetic simulations. Using more complex models for the geometry, and allowing for realistic β values, it is expected that some quantitative answers are found to issues only debated in a qualitative fashion in the present work. More specifically, a thorough analysis of the evaporating cloud problem is to be undertaken in order to assess the influence of plasma microturbulence by employing observational data for specific clouds. It is also planned to extend investigations to a larger range of astrophysical objects.

Acknowledgments

A great number of people have supported me during my time as a Ph.D. student at the Max Planck Institute for Plasma Physics, by giving advice, listening, lifting up my spirits, or simply by being excellent company. Adding to this group those who had accompanied me on the journey leading there, it would be impossible to name them all in such scarce space. Therefore, I must beg forgiveness of those who are not mentioned here by name.

First and foremost, I would like to offer my gratitude to my supervisor, Frank Jenko. Between introducing me to the world of gyrokinetics, providing deep insights into the realm of science, and helping out with many a problem, he also found ample time for idle talk and music. Additional thanks go to him and Rudolf Friedrich for their efforts in reading this thesis and agreeing to be on my board of examiners.

Our turbulence group, including all former and unofficial members, deserves a special mention; Tilman Dannert was most supportive during the first weeks and months when everything seemed like a big mystery (admittedly, some things still belong to that category). My office-mates – Tobias Görler, Thilo Hauff, and Florian Merz – created a wonderful environment not only by offering advice on work-related topics, but also by never failing to provide discussions about matters political, cultural, or religious. Klaus Reuter was at hand for practically every question concerning the sometimes rather overwhelming world of computer issues.

Many thanks go out to my other collaborators: Ralph Bruckschen, Gloria Falchetto, Abdou Garamoon, Matthias Hölzl, Matthias Kammerer, Laurent Laborde, Harald Lesch, José Mejia, Bill Nevins, Bruce Scott, Daniel Told, Laure Vermare, and Pavlos Xanthopoulos; to Aurelia Herrmann – with whom I had the pleasure of serving a most joyful term as Ph.D. student representative – and to the Ph.D. students, you have been great company.

Among the many from the institute who deserve acknowledgment, I would like to name our head of department, Sibylle Günter, and my former plasma physics lecturer, Hartmut Zohm. Also, the sports groups I have the honor of partaking

in shall not go unmentioned; thanks for the much-needed physical exercise and mental distraction.
Had it not been for the following people, chances are that I would not have made it to where I find myself now: thanks to my physics teachers in high school, Walter Beyer and Verena Schroll, and especially to my former professor, Harald Lesch, who has been a tremendous support in many ways both during my time as his student and after.
Kudos to Joss [132] and George for their cultural contributions.
Tobias Görler and Johannes Ferber undertook the effort of reading this thesis most diligently and brought many important details to my attention. I hereby express my thorough gratitude and hope you will let me return the favor when the time comes.
Last – but definitely not least: A hearty thank you to my parents and family, as well as to all my friends, it would not have been possible without you. And my deepest thanks and devotion to the love of my life, Beata.

Bibliography

[1] http://www.vikdhillon.staff.shef.ac.uk/teaching/phy213/phy213_fusion1.html (2009).

[2] http://www.kayelaby.npl.co.uk/images/fig38_t.jpg (2009).

[3] http://www.fys.uio.no/plasma/plasma/norsk/tokamak.gif (2009).

[4] http://www.ipp.mpg.de/ippcms/eng/images/pic/images_bereiche/w7x/380x265/grafik_stellarator_2.gif (2009).

[5] http://www.iter.org/ (2009).

[6] H. Zohm, *Edge localized modes (ELMs)*, Plasma Phys. Control. Fusion **38**, 105 (1996).

[7] S.-I. Itoh, K. Itoh, A. Fukuyama, and M. Yagi, *Edge Localized Modes as new bifurcation in tokamaks*, Phys. Rev. Lett. **76**, 920 (1996).

[8] http://en.wikipedia.org/wiki/Image:World_energy_usage_width_chart.svg (2009).

[9] http://www.ipcc.ch/pdf/assessment-report/ar4/wg3/ar4-wg3-chapter3.pdf (2009).

[10] K. Heinloth (editor), *Energy technologies: nuclear energy* (Springer, Berlin, 2005).

[11] H. Bartels, A. Poucet, G. Cambi, C. Gordon, M. Gaeta, W. Gulden, T. Honda, M. Iseli, H. Jahn, J. Koonce, et al., *ITER reference accidents*, Fusion Eng. Des. **42**, 13 (1998).

[12] F. Najmabadi, A. Abdou, L. Bromberg, T. Brown, V. C. Chan, M. C. Chu, F. Dahlgren, L. El-Guebaly, P. Heitzenroeder, D. Henderson, et al., *The ARIES-AT advanced tokamak, advanced technology fusion power plant*, Fusion Eng. Des. **80**, 3 (2006).

[13] W. M. Tang and V. S. Chan, *Advances and challenges in computational plasma science*, Plasma Phys. Control. Fusion **47**, R1 (2005).

[14] W. X. Wang, G. Rewoldt, W. M. Tang, F. L. Hinton, J. Manickam, L. E. Zakharov, R. B. White, and S. Kaye, *Nonlocal neoclassical transport in tokamak and spherical torus experiments*, Phys. Plasmas **13**, 082501 (2006).

[15] R. Neu, M. Balden, V. Bobkov, R. Dux, O. Gruber, A. Herrmann, A. Kallenbach, M. Kaufmann, C. F. Maggi, H. Maier, et al., *Plasma wall interaction and its implication in an all tungsten divertor tokamak*, Plasma Phys. Control. Fusion **49**, B59 (2007).

[16] A. Dinklage, T. Klinger, G. Marx, and L. Schweikhard, *Plasma physics: confinement, transport and collective effects* (Springer, Berlin, 2005).

[17] D. A. Batchelor, M. Beck, A. Becoulet, R. V. Budny, C. S. Chang, P. H. Diamond, J. Q. Dong, G. Y. Fu, A. Fukuyama, T. S. Hahm, et al., *Simulation of fusion plasmas: current status and future direction*, Plasma Sci. Technol. **9**, 312 (2007).

[18] R. G. Littlejohn, *A guiding center Hamiltonian: a new approach*, J. Math. Phys. **20**, 2445 (1979).

[19] R. G. Littlejohn, *Hamiltonian formulation of guiding center motion*, Phys. Fluids **24**, 1730 (1981).

[20] R. G. Littlejohn, *Hamiltonian perturbation theory in noncanonical coordinates*, J. Math. Phys. **23**, 742 (1982).

[21] J. R. Cary and R. G. Littlejohn, *Noncanonical Hamiltonian mechanics and its application to magnetic field line flow*, Ann. Phys. **151**, 1 (1983).

[22] T. S. Hahm, W. W. Lee, and A. Brizard, *Nonlinear gyrokinetic theory for finite-beta plasmas*, Phys. Fluids **31**, 1940 (1988).

[23] T. S. Hahm, *Nonlinear gyrokinetic equations for tokamak microturbulence*, Phys. Fluids **31**, 2670 (1988).

[24] A. J. Brizard, *Gyrokinetic energy conservation and Poisson-bracket formulation*, Phys. Fluids B **1**, 1381 (1989).

[25] A. J. Brizard and T. S. Hahm, *Foundations of nonlinear gyrokinetic theory*, Rev. Mod. Phys. **79**, 421 (2007).

[26] T. Dannert, Ph.D. thesis, Technische Universität München (2004).

[27] M. J. Pueschel, Second workshop and training program in cheap plasma technology applications in industry and environment, Cairo, Egypt (Al-Azhar University, 2007).

[28] M. A. Beer, Ph.D. thesis, Princeton University (1995).

[29] F. Merz, Ph.D. thesis, Westfälische Wilhelms-Universität Münster (2008).

[30] P. Xanthopoulos and F. Jenko, *Clebsch-type coordinates for nonlinear gyrokinetics in generic toroidal configurations*, Phys. Plasmas **13**, 092301 (2006).

[31] J. W. Connor, R. J. Hastie, and J. B. Taylor, *Shear, periodicity, and plasma ballooning modes*, Phys. Rev. Lett. **40**, 396 (1978).

[32] X. Lapillonne, S. Brunner, T. Dannert, S. Jolliet, A. Marinoni, , L. Villard, T. Görler, F. Jenko, and F. Merz, *Limitations of the $s-\alpha$ equilibrium model for gyrokinetic computations of turbulence*, submitted to Phys. Plasmas (2009).

[33] F. Jenko, W. Dorland, M. Kotschenreuther, and B. N. Rogers, *Electron temperature gradient driven turbulence*, Phys. Plasmas **7**, 1904 (2000).

[34] T. Dannert and F. Jenko, *Gyrokinetic simulation of collisionless trapped-electron mode turbulence*, Phys. Plasmas **12**, 072309 (2005).

[35] M. Kammerer, Master's thesis, Universität Ulm (2008).

[36] J. Roman, M. Kammerer, F. Merz, and F. Jenko, *Fast eigenvalue calculations in a massively parallel plasma turbulence code*, submitted for publication in 5th Special Issue of Parallel Computing on Parallel Matrix Algorithms and Applications (2009).

[37] V. Hernández, J. E. Román, and V. Vidal, *SLEPc: scalable library for eigenvalue problem computations*, Lect. Notes Comput. Sci. **2565**, 377 (2003).

[38] V. Hernández, J. E. Román, and V. Vidal, *SLEPc: a scalable and flexible toolkit for the solution of eigenvalue problems*, ACM Transactions on Mathematical Software **31**, 351 (2005).

[39] M. Hoelzl, *private communication* (2008).

[40] C. Gourdon, *Programme optimisé de calculs numériques dans les configurations magnétiques toroidales* (CEN, Fontenay aux Roses, 1970).

[41] `http://www.povray.org/` (2009).

[42] `http://megapov.inetart.net/` (2009).

[43] C. Nuber, R. W. Bruckschen, B. Hamann, and K. I. Joy, Medical Imaging 2003: Visualization, Image-Guided Procedures, and Display, San Diego, USA (SPIE, 2003).

[44] F. K. Röpke and R. W. Bruckschen, *Thermonuclear supernovae: a multi-scale astrophysical problem challenging numerical simulations and visualization*, New J. Phys. **10**, 125009 (2008).

[45] `https://jogl.dev.java.net/` (2009).

[46] `http://www.opengl.org/` (2009).

[47] M. J. Pueschel, T. Dannert, and F. Jenko, *On the role of numerical dissipation in Vlasov simulations of plasma microturbulence*, to be submitted to Comp. Phys. Commun. (2009).

[48] F. Jenko and B. D. Scott, *Numerical computation of collisionless drift wave turbulence*, Phys. Plasmas **6**, 2418 (1999).

[49] B. D. Fried and S. D. Conte, *The plasma dispersion function* (Academic Press, New York, 1961).

[50] R. J. Goldston and P. H. Rutherford, *Introduction to plasma physics* (IoP Publishing, Bristol, 1995).

[51] L. Chen, S. Briguglio, and F. Romanelli, *The long-wavelength limit of the ion-temperature gradient mode in tokamak plasmas*, Phys. Fluids B **3**, 611 (1991).

[52] T. Dannert and F. Jenko, *Vlasov simulation of kinetic shear Alfvén waves*, Comput. Phys. Commun. **163**, 67 (2004).

[53] A. Hasegawa and M. Wakatani, *Self-organization of electrostatic turbulence in a cylindrical plasma*, Phys. Rev. Lett. **59**, 1581 (1987).

[54] M. N. Rosenbluth and F. L. Hinton, *Poloidal flow driven by ion-temperature-gradient turbulence in tokamaks*, Phys. Rev. Lett. **80**, 724 (1998).

[55] J. Candy, R. E. Waltz, and M. N. Rosenbluth, *Smoothness of turbulent transport across a minimum-q surface*, Phys. Plasmas **11**, 1879 (2004).

[56] A. M. Dimits, G. Bateman, M. A. Beer, B. I. Cohen, W. Dorland, G. W. Hammett, C. Kim, J. E. Kinsey, M. Kotschenreuther, A. H. Kritz, et al., *Comparisons and physics basis of tokamak transport models and turbulence simulations*, Phys. Plasmas **7**, 969 (2000).

[57] W. M. Nevins, J. Candy, S. Cowley, T. Dannert, A. Dimits, W. Dorland, C. Estrada-Mila, G. W. Hammett, F. Jenko, M. J. Pueschel, et al., *Characterizing electron temperature gradient turbulence via numerical simulation*, Phys. Plasmas **13**, 122306 (2006).

[58] A. M. Dimits, W. M. Nevins, D. E. Shumaker, G. W. Hammett, T. Dannert, F. Jenko, M. J. Pueschel, W. Dorland, S. C. Cowley, J. N. Leboeuf, et al., *Gyrokinetic simulations of ETG and ITG turbulence*, Nucl. Fusion **47**, 817 (2007).

[59] F. Jenko and W. Dorland, *Nonlinear electromagnetic gyrokinetic simulations of tokamak plasmas*, Plasma Phys. Control. Fusion **43**, A141 (2001).

[60] C. Holland and P. H. Diamond, *Electromagnetic secondary instabilities in electron temperature gradient turbulence*, Phys. Plasmas **9**, 3857 (2002).

[61] M. J. Pueschel, M. Kammerer, and F. Jenko, *Gyrokinetic turbulence simulations at high plasma beta*, Phys. Plasmas **15**, 102310 (2008).

[62] C. E. Kessel, *Bootstrap current in a tokamak*, Nucl. Fusion **34**, 1221 (1994).

[63] J. Wesson, *Tokamaks* (Claredon Press, Oxford, 1997).

[64] M. Ushigome, S. Ide, S. Itoh, E. Jotaki, O. Mitarai, S. Shiraiwa, T. Suzuki, Y. Takase, S. Tanaka, T. Fujita, et al., *Development of completely solenoidless tokamak operation in JT-60U*, Nucl. Fusion **46**, 207 (2006).

[65] D. C. McDonald, L. Laborde, J. C. DeBoo, F. Ryter, C. D. Challis, P. de Vries, J. Hobirk, E. Joffrin, T. C. Luce, J. Mailloux, et al., 35th EPS Conference on Plasma Physics, Herniossos, Greece (EPS, 2008).

[66] C. C. Petty, *Sizing up plasmas using dimensionless parameters*, Phys. Plasmas **15**, 080501 (2008).

[67] C. C. Petty, T. C. Luce, D. C. McDonald, J. Mandrekas, M. R. Wade, J. Candy, J. G. Cordey, V. Drozdov, T. E. Evans, J. R. Ferron, et al., 45th Annual Meeting of the APS Division of Plasma Physics, Albuquerque, USA (AIP, 2004).

[68] D. C. McDonald, J. G. Cordey, C. C. Petty, M. Beurskens, R. Budny, I. Coffey, M. de Baar, C. Giroud, E. Joffrin, P. Lomas, et al., *The beta scaling of energy confinement in ELMy H-modes in JET*, Plasma Phys. Control. Fusion **46**, A215 (2004).

[69] ITER Physics Basis, *Chapter 2: Plasma confinement and transport*, Nucl. Fusion **39**, 2175 (1999).

[70] H. Urano, T. Takizuka, H. Takenaga, N. Oyama, Y. Miura, and Y. Kamada, *Confinement degradation with beta for ELMy H-mode plasmas in JT-60U tokamak*, Nucl. Fusion **46**, 781 (2006).

[71] L. Vermare, F. Ryter, C. Angioni, A. G. Peeters, J. Stober, R. Bilato, L. D. Horton, B. Kurzan, C. F. Maggi, H. Meister, et al., *Study of the β dependence of confinement and heat transport in ASDEX Upgrade*, Nucl. Fusion **47**, 490 (2007).

[72] C. C. Petty, *private communication* (2009).

[73] C. M. Greenfield, J. C. DeBoo, T. H. Osborne, F. W. Perkins, M. N. Rosenbluth, and D. Boucher, *Enhanced fusion performance due to plasma shape modification of simulated ITER discharges in DIII-D*, Nucl. Fusion **37**, 1215 (1997).

[74] G. L. Falchetto, B. D. Scott, P. Angelino, A. Bottino, T. Dannert, V. Grandgirard, S. Janhunen, F. Jenko, S. Jolliet, A. Kendl, et al., *The european turbulence code benchmarking effort: turbulence driven by thermal gradients in magnetically confined plasmas*, Plasma Phys. Control. Fusion **50**, 124015 (2008).

[75] B. D. Scott, *Free-energy conservation in local gyrofluid models*, Phys. Plasmas **12**, 102307 (2005).

[76] A. G. Peeters and D. Strintzi, *The effect of a uniform radial electric field on the toroidal ion temperature gradient mode*, Phys. Plasmas **11**, 3748 (2004).

[77] A. G. Peeters, C. Angioni, and D. Strintzi, *Toroidal momentum pinch velocity due to the Coriolis drift effect on small scale instabilities in a toroidal plasma*, Phys. Rev. Lett. **98**, 265003 (2007).

[78] P. B. Snyder and G. W. Hammett, *Electromagnetic effects on plasma microturbulence and transport*, Phys. Plasmas **8**, 744 (2001).

[79] B. D. Scott, *Computation of turbulence in magnetically confined plasmas*, Plasma Phys. Control. Fusion **48**, B277 (2006).

[80] Y. Chen, S. E. Parker, B. I. Cohen, A. M. Dimits, W. M. Nevins, D. Shumaker, V. K. Decyk, and J. N. Leboeuf, *Simulations of turbulent transport with kinetic electrons and electromagnetic effects*, Nucl. Fusion **43**, 1121 (2003).

[81] S. E. Parker, Y. Chen, W. Wan, B. I. Cohen, and W. M. Nevins, 45th Annual Meeting of the APS Division of Plasma Physics, Albuquerque, USA (AIP, 2004).

[82] J. Candy, *Beta scaling of transport in microturbulence simulations*, Phys. Plasmas **12**, 072307 (2005).

[83] M. Kotschenreuther, G. Rewoldt, and W. M. Tang, *Comparison of initial value and eigenvalue codes for kinetic toroidal plasma instabilities*, Comput. Phys. Commun. **8**, 128 (1995).

[84] P. B. Snyder, Ph.D. thesis, Princeton University (1999).

[85] M. S. Chu, C. Chu, G. Guest, J. Y. Hsu, and T. Ohkawa, *Kinetic analysis of the localized magnetohydrodynamic ballooning mode*, Phys. Rev. Lett. **41**, 247 (1978).

[86] C. Z. Cheng, *Kinetic theory of collisionless ballooning modes*, Phys. Fluids **25**, 1020 (1982).

[87] F. Zonca, L. Chen, J. Q. Dong, and R. A. Santoro, 40th Annual Meeting of the APS Division of Plasma Physics, New Orleans, USA (AIP, 1999).

[88] J. Dong, L. Chen, and F. Zonca, *Study of kinetic shear Alfvén modes driven by ion temperature gradient in tokamak plasmas*, Nucl. Fusion **39**, 1041 (1999).

[89] G. Zhao and L. Chen, *Gyrokinetic particle-in-cell simulation of Alfvénic ion-temperature-gradient modes in tokamak plasma*, Phys. Plasmas **9**, 861 (2002).

[90] G. L. Falchetto, J. Vaclavik, and L. Villard, *Global-gyrokinetic study of finite beta effects on linear microinstabilities*, Phys. Plasmas **10**, 1424 (2003).

[91] T. Kato, *Perturbation theory of linear operators* (Springer, Berlin, 1966).

[92] M. Kammerer, F. Merz, and F. Jenko, *Exceptional points in linear gyrokinetics*, Phys. Plasmas **15**, 052102 (2008).

[93] F. Jenko, T. Dannert, and C. Angioni, *Heat and particle transport in a tokamak: advances in nonlinear gyrokinetics*, Plasma Phys. Control. Fusion **47**, B195 (2005).

[94] M. Kotschenreuther, W. Dorland, M. A. Beer, and G. W. Hammett, *Quantitative predictions of tokamak energy confinement from first-principles simulations with kinetic effects*, Phys. Plasmas **2**, 2381 (1995).

[95] P. H. Diamond, S.-I. Itoh, K. Itoh, and T. S. Hahm, *Zonal flows in plasma – a review*, Plasma Phys. Control. Fusion **47**, R35 (2005).

[96] T. S. Hahm, M. A. Beer, Z. Lin, G. W. Hammett, W. W. Lee, and W. M. Tang, *Shearing rate of time-dependent E x B flow*, Phys. Plasmas **6**, 922 (1999).

[97] P. Xanthopoulos, F. Merz, T. Görler, and F. Jenko, *Nonlinear gyrokinetic simulations of ion-temperature-gradient turbulence for the optimized Wendelstein 7-X stellarator*, Phys. Rev. Lett. **99**, 035002 (2007).

[98] F. Jenko and A. Kendl, *Radial and zonal modes in hyperfine-scale stellarator turbulence*, Phys. Plasmas **9**, 4103 (2002).

[99] F. Merz and F. Jenko, *Nonlinear saturation of trapped electron modes via perpendicular particle diffusion*, Phys. Rev. Lett. **100**, 035005 (2008).

[100] J. Lang, S. E. Parker, and Y. Chen, *Nonlinear saturation of collisionless trapped electron mode turbulence: zonal flows and zonal density*, Phys. Plasmas **15**, 055907 (2008).

[101] A. B. Rechester and M. N. Rosenbluth, *Electron heat transport in a tokamak with destroyed magnetic surfaces*, Phys. Rev. Lett. **40**, 38 (1978).

[102] Z. Chang and J. D. Callen, *Unified fluid/kinetic description of plasma microinstabilities. part i: Basic equations in a sheared slab geometry*, Phys. Fluids B **4**, 1167 (1992).

[103] R. Fitzpatrick, *Helical temperature perturbations associated with tearing modes in tokamak plasmas*, Phys. Plasmas **2**, 825 (1995).

[104] T. Hauff and F. Jenko, *E x B advection of trace ions in tokamak microturbulence*, Phys. Plasmas **14**, 092301 (2007).

[105] T. Hauff, M. J. Pueschel, T. Dannert, and F. Jenko, *Electrostatic and magnetic transport of energetic ions in turbulent plasmas*, Phys. Rev. Lett. **102**, 075004 (2009).

[106] G. M. Webb, G. P. Zank, E. K. Kaghashvili, and J. A. le Roux, *Compound and perpendicular diffusion of cosmic rays and random walk of the field lines*, Astrophys. J. **651**, 211 (2006).

[107] W. W. Heidbrink, C. W. Barnes, G. W. Hammett, Y. Kusama, S. D. Scott, M. C. Zarnstorff, L. C. Johnson, D. McCune, S. S. Medley, H. K. Park, et al., *The diffusion of fast ions in Ohmic TFTR discharges*, Phys. Fluids B **3**, 3167 (1991).

[108] W. W. Heidbrink and G. J. Sadler, *The behaviour of fast ions in tokamak experiments*, Nucl. Fusion **34**, 535 (1994).

[109] H. E. Mynick and J. A. Krommes, *Particle diffusion by magnetic perturbations of axisymmetric geometries*, Phys. Rev. Lett. **43**, 1506 (1979).

[110] J. R. Myra and P. J. Catto, *Effect of drifts on the diffusion of runaway electrons in tokamak stochastic magnetic fields*, Phys. Fluids B **4**, 176 (1992).

[111] M. J. Pueschel, L. Laborde, F. Jenko, and JET EFDA contributors, 35th EPS Conference on Plasma Physics, Herniossos, Greece (EPS, 2008).

[112] Y. Chen and S. E. Parker, *Electromagnetic gyrokinetic δf particle-in-cell turbulence simulation with realistic equilibrium profiles and geometry*, J. Comput. Phys. **220**, 839 (2007).

[113] D. R. Mikkelsen and W. Dorland, *Dimits shift in realistic gyrokinetic plasma-turbulence simulations*, Phys. Rev. Lett. **101**, 135003 (2008).

[114] `http://chandra.harvard.edu/photo/2000/0163/0163_xray_fullfield.jpg` (2009).

[115] A. C. Fabian, *Cooling flows in clusters of galaxies*, Annu. Rev. Astron. Astrophys. **32**, 277 (1994).

[116] L. M. Voigt, R. W. Schmidt, A. C. Fabian, S. W. Allen, and R. M. Johnstone, *Conduction and cooling flows*, Mon. Not. R. Astron. Soc. **335**, L7 (2002).

[117] L. M. Voigt and A. C. Fabian, *Thermal conduction and reduced cooling flows in galaxy clusters*, Mon. Not. R. Astron. Soc. **347**, 1130 (2004).

[118] E. Churazov, M. Brüggen, C. R. Kaiser, H. Böhringer, and W. Forman, *Evolution of buoyant bubbles in M87*, Astrophys. J. **554**, 261 (2001).

[119] A. C. Fabian, R. F. Mushotzky, P. E. J. Nulsen, and J. R. Peterson, *On the soft X-ray spectrum of cooling flows*, Mon. Not. R. Astron. Soc. **321**, L20 (2001).

[120] A. C. Fabian, S. W. Allen, C. S. Crawford, R. M. Johnstone, R. G. Morris, J. S. Sanders, and R. W. Schmidt, *The missing soft X-ray luminosity in cluster cooling flows*, Mon. Not. R. Astron. Soc. **332**, L50 (2002).

[121] L. Spitzer, *Physics of fully ionized gases* (Wiley, New York, 1962).

[122] R. Narayan and M. V. Medvedev, *Thermal conduction in clusters of galaxies*, Astrophys. J. **562**, L129 (2001).

[123] J. Cho, A. Lazarian, A. Honein, B. Knaepen, S. Kassinos, and P. Moin, *Thermal conduction in magnetized turbulent gas*, Astrophys. J. **589**, L77 (2003).

[124] A. C. Fabian, J. S. Sanders, C. S. Crawford, C. J. Conselice, J. S. Gallagher, and R. F. G. Wyse, *The relationship between the optical Hα filaments and the X-ray emission in the core of the Perseus cluster*, Mon. Not. R. Astron. Soc. **344**, L48 (2003).

[125] S. L. Pistinner and D. Eichler, *Self-inhibiting heat flux: a chance for snowballs in hell?*, Phys. Rep. **311**, 475 (1999).

[126] P. Godon, N. Soker, and R. E. White III, *Amplification of magnetic fields in the centers of cluster cooling flows*, Astron. J. **116**, 37 (1998).

[127] N. Soker and C. L. Sarazin, *The role of magnetic fields in cluster cooling flows*, Astrophys. J. **348**, 73 (1990).

[128] `http://www.noao.edu/outreach/aop/observers/n6814africa.jpg` (2009).

[129] M. J. Rees, *Magnetic confinement of broad-line clouds in active galactic nuclei*, Mon. Not. R. Astron. Soc. **228**, 47P (1987).

[130] R. Sivron and S. Tsuruta, *Dense clouds near the central engine of active galactic nuclei*, Astrophys. J. **402**, 420 (1993).

[131] Z. Kuncic, E. G. Blackman, and M. J. Rees, *Physical constraints on the sizes of dense clouds in the central magnetospheres of active galactic nuclei*, Mon. Not. R. Astron. Soc. **283**, 1322 (1996).

[132] J. Whedon, *Serenity* (2005).